Response to reviewers, ACP-2019-1187

'Differences in tropical high clouds among reanalyses: origins and radiative impacts.'

We extend our thanks to both reviewers for your positive feedback and your thoughtful comments and advice. Following your suggestions, we have eliminated the multi-reanalysis mean, benchmarking the reanalyses against observed distributions instead. We have also adopted the most recent version of CERES EBAF, expanded our discussion of clear-sky and net radiative fluxes at the top-of-atmosphere, added further information on the reanalysis systems examined in the paper, and clarified several aspects of the methodology. Page and line numbers refer to the revised manuscript without changes tracked.

Response to major comments:

1. My first comments concern the presentation of the results. First, it baffles me why many of the biases (e.g., fig. 1 and 5) are presented with respect to multi-reanalyses mean (MRM) instead of observations. While it is understood that the observational datasets are subject to their own uncertainties and sampling discrepancies, it is still of the interest of most readers to see how each of the reanalyses compares to an observational ground truth. I strongly suggest the bias results be presented with respect to relevant observations wherever available.

AR: This choice was also a subject of much internal discussion. We initially opted to use the MRM for three reasons. First, this study is part of the SPARC Reanalysis Intercomparison Project, which is primarily aimed at intercomparison of reanalyses against each other. Second, using the MRM allows us to use the same 1980-2014 base period for both figures (initially this would have been 1984-2009 to match ISCCP and 2001-2014 to match CERES). Third, we view the satellite cloud products in particular as a questionable quantitative benchmark for the reanalyses (a large part of the motivation for focusing on 'qualitative' rather than 'quantitative' comparisons of reanalysis and observationally-based cloud fields, as mentioned below).

After further discussion, we decided that the first rationale can be mitigated by offering the MRM-based presentation in the S-RIP report and the observationally-based presentation here; the second by the H-series extension of ISCCP to recent years and an overall weak sensitivity of the results to the choice of base period (with the notable exception of the CFSR / CFSv2 transition as discussed in section 6); and the third by CERES EBAF being a more suitable quantitative benchmark for OLR than the MRM. Accordingly, we adopted your suggestion to use ISCCP with a 1984-2014 base period for high cloud cover and CERES EBAF with a 2001-2014 base period for OLR. To help make room for several additions in the revised text, we have eliminated both the MRM concept and maps based on MERRA from the paper. We retain the MERRA profiles in Figure 3F and Figure 4F to help illustrate the effects of model changes between MERRA and MERRA-2. The MRM and MERRA maps will still be included in chapter 8 of the S-RIP report.

Adopting the new benchmark directly works well for OLR (Figure R1, which replaces Figure 5 in the main text). We have inverted the color scale for OLR so that dark colors of OLR represent

low values, which helps to emphasize the difference between the difference plots and the CERES climatology, since most of the reanalyses produce OLR larger than indicated by CERES.

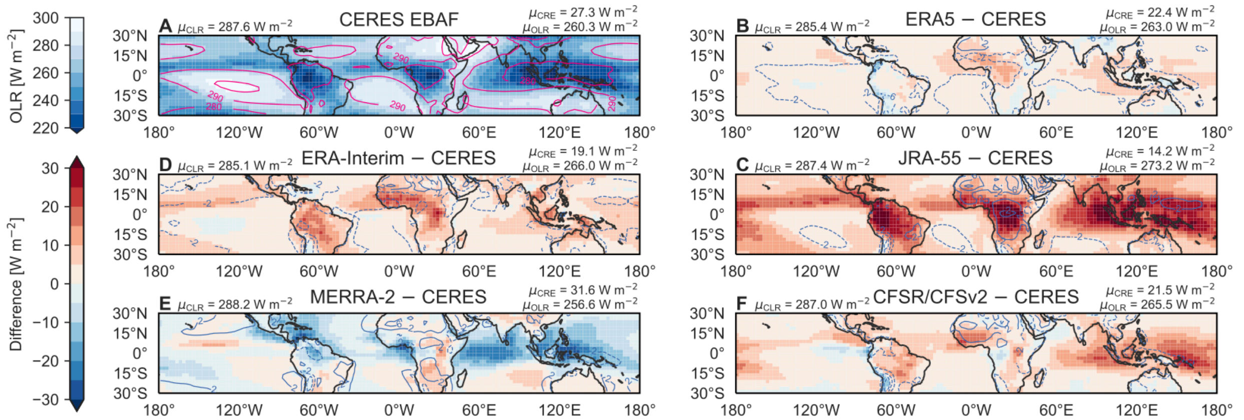

Figure R1: Climatological mean spatial distributions of all-sky outgoing longwave radiation (OLR; shading) and clear-sky outgoing longwave radiation (CLR; contours at intervals of 10 W m^{-2}) for (A) CERES EBAF over 2001–2014. Differences relative to CERES EBAF for the same period are shown for (B) ERA5, (C) ERA-Interim, (D) JRA-55, (E) MERRA-2, and (F) CFSR/CFSv2. Contours in panels (C) through (F) cover the range within ±10 W m^{-2} at intervals of 4 W m^{-2}. Tropical mean (30°S–30°N) values of OLR and CLR based on each product are shown at the upper right and left corners, respectively, of the corresponding panel. Tropical mean values for the longwave cloud radiative effect (LWCRE; CLR – OLR) are listed above those for OLR.

The high cloud fraction plot needed a little more modification: simply replacing the MRM with ISCCP made it difficult to describe the inter-reanalysis differences in the text and seemed to contradict our statement that "direct comparisons between cloud variables derived from observations and those derived from models may be misleading." To address this, we show instead maps of HCC for both ISCCP and each reanalysis with contour overlays to show differences relative to ISCCP (Figure R2, which replaces Figure 1 in the text).

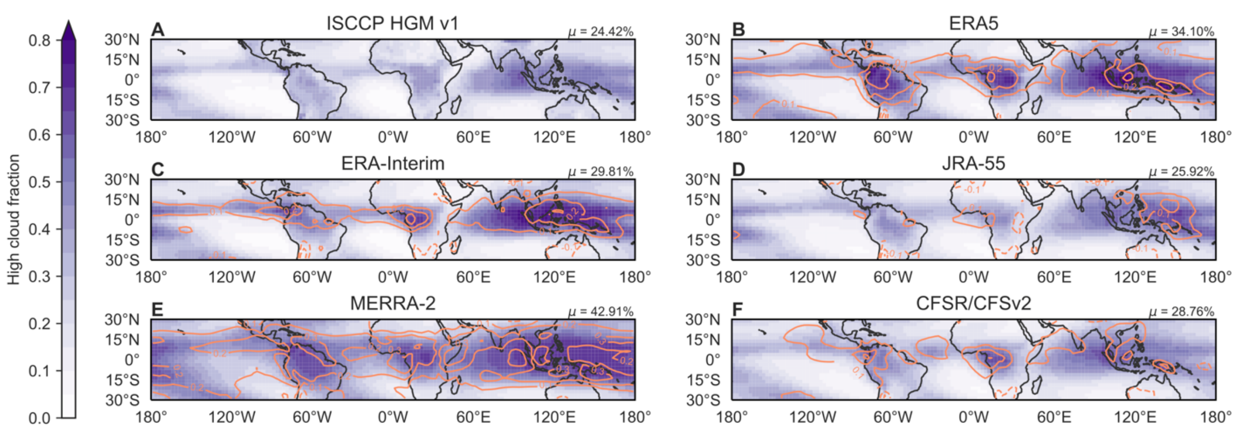

Figure R2: Climatological mean spatial distributions of high cloud cover (HCC) for (A) ISCCP HGM, (B) ERA5, (C) ERA-Interim, (D) JRA-55, (E) MERRA-2, and (F) CFSR/CFSv2 over 1984–2014. Differences relative to ISCCP HGM are shown for each reanalysis as orange contours (dashed

for negative values) at intervals of 0.1. The area-weighted tropical mean (30°S—30°N) HCC based on each product is shown at the upper right corner of the corresponding panel.

Second, I find some results are presented in unconventional, and probably not advantageous, ways. One example is Fig 11. The authors may be seeking a concise way to present rich information from many variables: HTR, RH, CRE, CWC, etc., although the plots become difficult to interpret. I suggest the authors decouple these variables and use more straightforward plots to evidence their points, or, less preferably, identify what features are for the readers to recognize and explain how they relate to their points.
AR: Thank you for this comment. The purpose of Figure 11 is to examine differences in cloud fields within the TTL, above the typical levels of convective detrainment and often above the level of zero net radiative heating. Clouds in this layer are primarily associated with slow radiatively-balanced ascent, and occasionally with very deep convection that penetrates into the TTL (e.g., Fueglistaler et al., 2009). We expect these two cloud populations to be distinguished by their cloud water contents (smaller for in situ cirrus; larger for convective overshoots) and radiative heating rates (weak radiative heating for slow ascent; usually strong cloud-top cooling for deep convection, though the latter depends on anvil depth as shown in previous Fig 12). Choosing radiative heating as one axis thus helps to distinguish the different types of clouds at these levels: (1) in situ clouds, which occur at high RH in tandem with weak positive heating rates (i.e., close to the 'spine' of the plot); (2) deep convection that detrains near the base of the TTL, which is associated with large CWCs and negative radiative heating (the left 'wing', exemplified by the blue profiles in previous Fig 12); and (3) deep convection that penetrates to near the tropopause and detrains within the TTL, which is associated with larger CWCs and positive heating rates (the right 'wing', red profiles in previous Fig 12). Selecting RH as the other axis helps to highlight some important differences and unexpected features, including differences in ice supersaturation and in situ cloud occurrence between ERA5 and ERA-Interim (supersaturation and related clouds are typically collocated with deep convective areas in ERA-Interim but form mostly away from deep convective areas in ERA5); the unexpected prevalence of ice supersaturation in MERRA-2, especially at 150 hPa; and the unrealistic behavior of CFSR water vapor fields at these levels. This approach also serves to set up our crude estimates of inter-reanalysis differences in overshooting (0-0.2%) and in situ cirrus (10-35%) frequencies at 100 hPa (p.29, l.1-6). We have revised and added text to better to better explain the motivation and interpretation of this figure (p.27, l.2 through p.28, l.8; see more detail below).

My last complaint about presentation is that I find some potentially very interesting and important results omitted. This applies to a few places: Fig 5. What about SW and net (LW+SW) results? A central radiative question about the high clouds is to what extent their LW and SW effects compensate [e.g., Kolly & Huang 2018; Wall et al. 2019] and how different datasets may bias this compensation [e.g., Zhu et al. 2019 Fig. S1 and relevant texts].
AR: Thank you for this suggestion. We have produced a figure that shows the distribution of the TOA net radiative flux (all-sky and clear-sky) together with the tropical mean net cloud effect. This figure is included here as Fig R3, again adopting the 2001-2014 period for overlap

with CERES (the results are only weakly sensitive to this choice). Rather than difference plots, we prefer to show the absolute distribution of net radiative flux for each reanalysis here, as in the new version of Fig 1. We have added this as Fig 6 in the revised manuscript, along with the accompanying text (p.14, l.15 – p.15, l.16):

"Figure 6 shows spatial distributions of all-sky net radiation based on CERES EBAF and the five reanalyses, with positive values indicating time-mean energy fluxes into the tropical climate system. Mean values across the tropics are positive (incoming solar radiation exceeds OLR), as indicated here by CERES EBAF (net gain of 45.0 W m^{-2}). This excess of incoming energy in the already energy-rich tropics is essential to the 'heat engine' model of the atmospheric circulation, and is contributed primarily by imbalances in the clear-sky fluxes (e.g. Stephens and L'Ecuyer, 2015, and references therein). Net clear-sky fluxes into the tropics are typically somewhat larger in the reanalyses than in CERES, with overestimates as large as 7 W m^{-2} (in ERA-Interim). The closest match in the tropical mean is provided by JRA-55, which is within 0.1 W m^{-2} of CERES (this good agreement does not extend to the all-sky net radiation flux, as detailed below). Cloud effects reduce the energy excess provided by clear sky radiation, as the negative SWCRE (cloud albedo) outweighs the positive LWCRE. However, most of the reanalyses greatly overestimate the magnitude of this reduction relative to CERES. Such overestimates have implications for atmospheric energy transport, and could result at least in part from the lack of two-way coupling between cloud fields and SST in the reanalyses (e.g. Kolly and Huang, 2018; Wall et al., 2019). For JRA-55, which overestimates the net CRE by 22.5 W m^{-2} relative to CERES, a little more than half of the bias in the net CRE is attributable to the bias in the LWCRE. The remainder is due to overestimated cloud albedo effects. Similar ratios hold for ERA5 and ERA-Interim, with biases in the LWCRE contributing approximately 55% of the overall biases in each case. For MERRA-2, overestimated cloud albedo effects more than compensate for the stronger LWCRE, producing a net CRE similar to that in ERA5 (approximately 9 W m^{-2} stronger than that from CERES). CFSR/CFSv2 produces a net CRE very similar to that indicated by CERES, implying compensating biases in the SWCRE and LWCRE. However, the horizontal gradients of net radiation are much sharper in this reanalysis than in any of the other data sets included in Fig. 6."

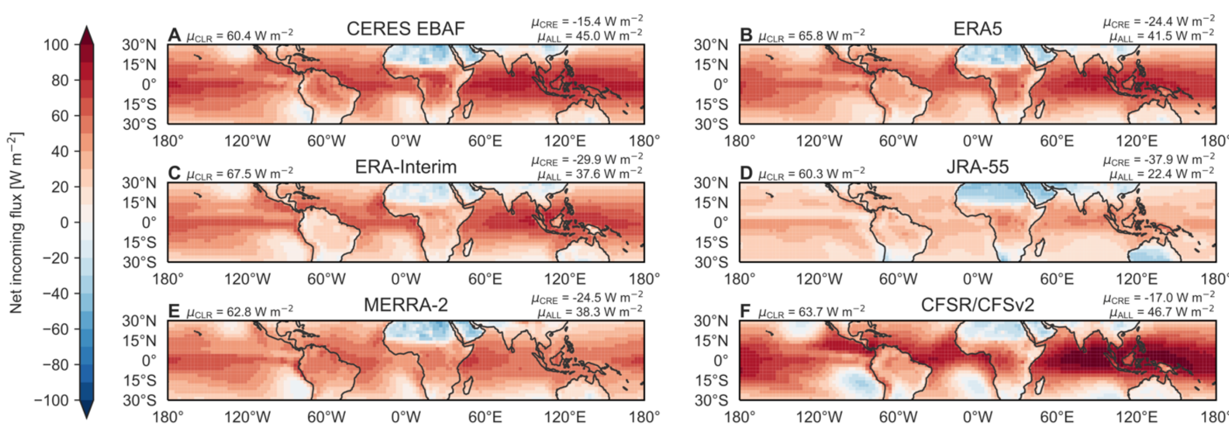

Figure R3: Climatological mean spatial distributions of all-sky net incoming radiation (ALL; shading) for (A) CERES EBAF, (B) ERA5, (C) ERA-Interim, (D) JRA-55, (E) MERRA-2, and (F)

CFSR/CFSv2 during 2001–2014. Tropical mean (30°S–30°N) values of ALL and clear-sky net incoming radiation (CLR) based on each product are shown at the upper right and left corners, respectively, of the corresponding panel. Tropical mean values for the net cloud radiative effect (CRE = CLR – ALL) are listed above those for ALL. Positive values indicate time-mean energy fluxes into the tropical climate system.

Fig. 10. Why not show the three related variables: T, q and z (components of MSE), respectively here?

AR: The motivation for showing MSE is because of its links with both the occurrence and effects of convection, but we like this idea as well. In the revised submission, along with the profiles of MSE, we have included distributions of c_pT, L_vq, and gz for Q4 in each of the five reanalyses at the 300 hPa, 500 hPa, and 850 hPa levels (Fig R4; now Fig 11 in the revised text). Note that ERA5 is adopted as the reference rather than ERA-Interim (as in the original text for comparison with MERRA-2) or AIRS (as the 'observational' distribution in the profile panel). This modification supports and expands the existing discussion in the paper.

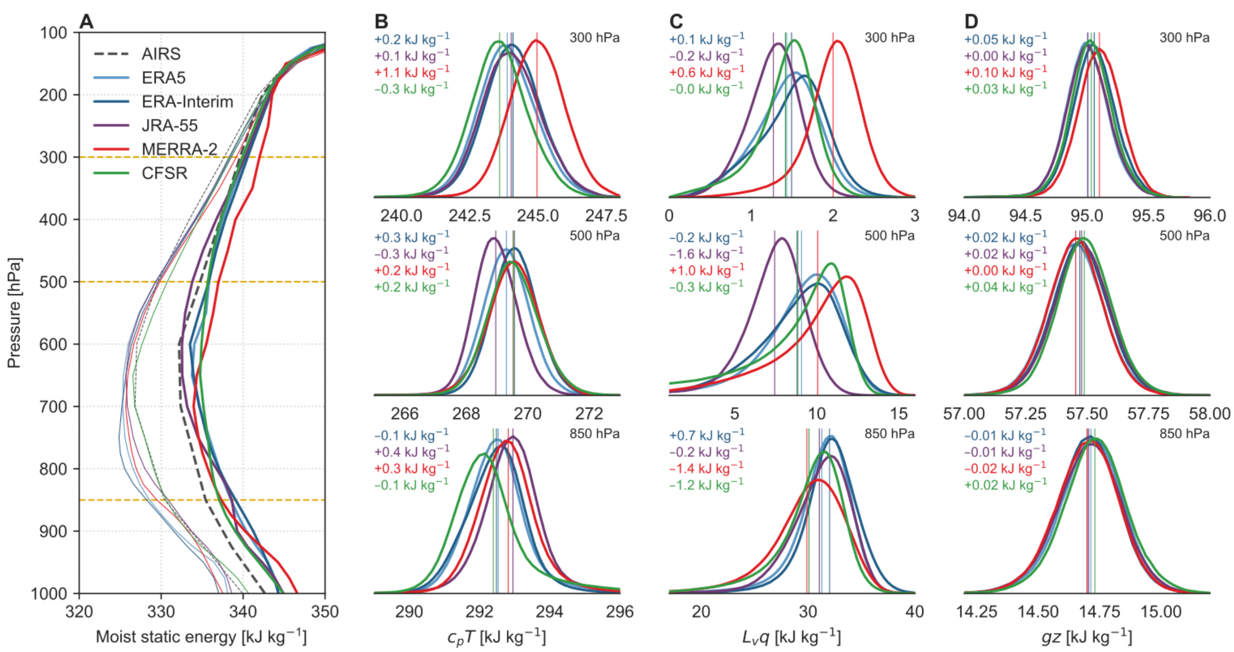

Figure R4: (A) Composite vertical profiles of moist static energy (MSE) for ERA5 (cyan), ERA-Interim (blue), JRA-55 (purple), MERRA-2 (red), and CFSR (green) averaged for the upper (Q4; thick lines) and lower (Q1; thin lines) quartiles of daily-mean LWCRE during 2001–2010. Profiles calculated from AIRS observations (September 2002–December 2010; grey dashed lines) are shown for context. AIRS profiles are conditioned on quartiles of daily-mean LWCRE from CERES SYN1Deg. At right are distributions of the (B) temperature (c_pT), (C) moisture (L_vq), and (D) geopotential (gz) components of MSE for Q4 from each reanalysis at 850 hPa (lower row), 500 hPa (centre row), and 300 hPa (upper row). Levels correspond to the horizontal yellow dashed lines in panel A. Mean values are marked as vertical lines; biases in these mean values relative to the mean value from ERA5 are color-coded at the upper left of each panel (each list from top: ERA-Interim, JRA-55, MERRA-2, CFSR).

Fig. 13. What about the clear-sky OLR?

AR: We have added a panel showing the evolution of anomalies in the clear-sky OLR averaged over the inner tropics. (Figure R5; now Fig 14 in the revised text). This figure and Figure 15 have also been updated to use CERES EBAF Ed4.1 in place of Ed4A.

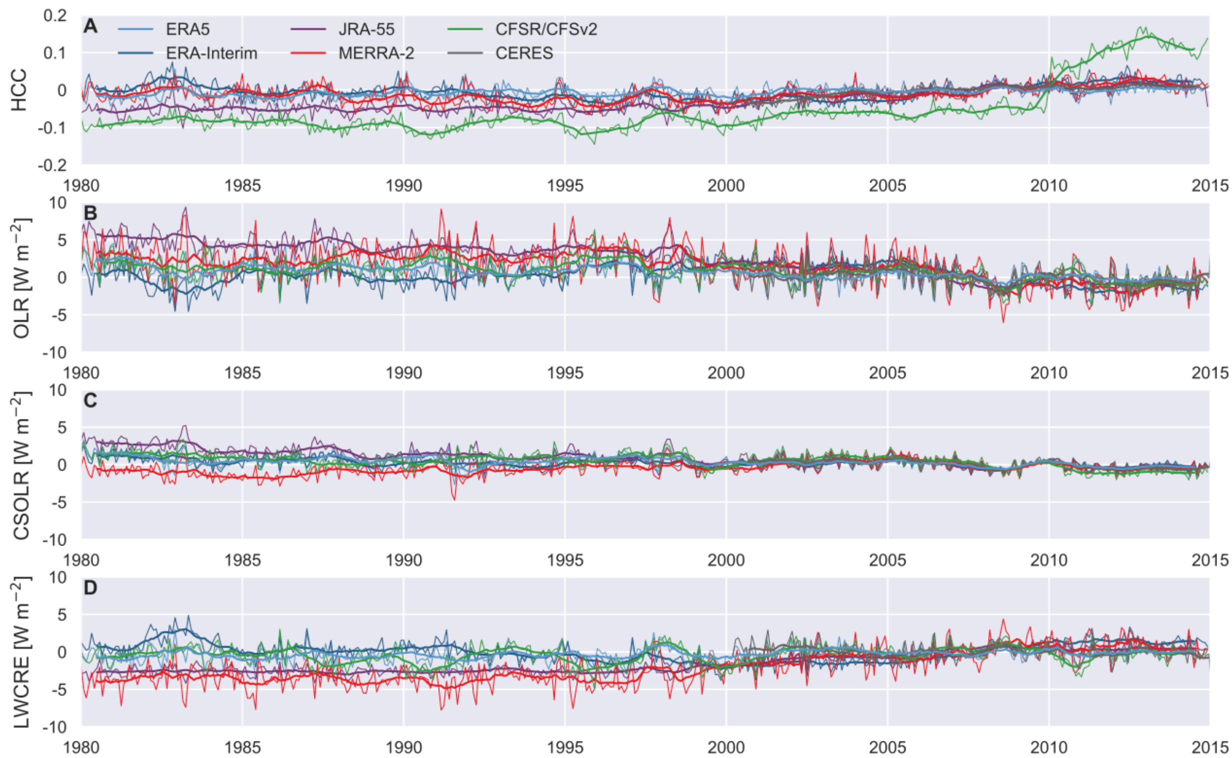

E Trends (1980–2014)

	ERA5	ERA-I	JRA-55	MRR-2	CFSR/v2	CFSR 1980-2009	SRB 1984-2007	NOAA	ISCCP 1984-2014
HCC	**** +0.5	+0.1	**** +2.3	* +0.7	**** +2.3	**** +1.3			** –0.7
OLR	**** –0.56	–0.07	**** –2.06	**** –1.23	**** –0.68	**** –0.55	* +0.46	+0.14	
CSOLR	**** –0.34	**** –0.29	**** –0.90	**** +0.38	**** –0.49	* –0.26	**** –1.15		
LWCRE	**** +0.22	–0.23	**** +1.1	**** +1.60	+0.15	* +0.28	**** –1.57		

F Trends (2001–2014)

	ERA5	ERA-I	JRA-55	MRR-2	CFSR/v2	CFSR 2001-2009	CERES	ISCCP/ NOAA	MODIS
HCC	+0.2	**** +5.0	**** +2.5	**** +3.4	**** +16.6	+1.9	**** +2.3	–0.7	–0.3
OLR	–0.41	**** –3.30	**** –1.97	*** –2.19	**** –1.51	–1.58	–0.73	–1.17	
CSOLR	** –0.56	–0.34	** –0.85	** –0.90	**** –1.93	–1.60	*** –0.94		
LWCRE	–0.07	**** +2.96	**** +1.17	*** +1.47	–0.48	+0.56	–0.43		

Figure R5: Time series of deseasonalized anomalies in (A) monthly mean high cloud cover (HCC), (B) monthly mean OLR, and (C) monthly mean LWCRE averaged over the inner tropics (10°S–10°N) for 1980–2014 based on ERA5 (cyan), ERA-Interim (blue), JRA-55 (purple), MERRA-2 (red), and CFSR/CFSv2 (green). Observational analyses from CERES SYN1Deg (A; March 2000–December 2014) and CERES EBAF (B and C; March 2000–December 2014) are shown for context. Anomalies are calculated relative to the mean annual cycle during 2001–2014. Thick lines show time series after applying a 12-month uniformly-weighted rolling mean. Trends are listed for annual-mean anomalies during the (D) 1980–2014 and (E) 2001–2014 periods in percentage points per decade for HCC and units of W m^{-2} per decade for OLR, clear-sky OLR, and LWCRE. Stars indicate statistical significance at the 90% (*), 95% (**), 99% (***), and 99.5% (****) confidence levels. Light grey shading indicates that the 90% confidence interval of the Theil–Sen slope contains zero. Blue colors mark negative trends and red colors positive trends, with darker shades signifying larger trend magnitudes (0 to 1, 1 to 2, 2 to 3, and greater than 3).

2. A technical comment: it should be cautioned that CRE, defined as the difference between clear- and all-skies, is subject to influence of clear-sky [e.g., Soden 2004]. I'd suggest where appropriate (e.g., Fig. 5) clear-sky biases be also examined to ensure that the CRE difference measures cloud effect, instead of being affected by the clearsky differences between the reanalyses.
AR: Thank you for raising this point. In the revised manuscript we have addressed differences in clear-sky radiative fluxes more directly, both by including them in Fig 5 (as contours in place of LWCRE) and by discussing the differences in both all-sky and clear-sky OLR in the text (p.7, l.13-14; p.13, l.18-27, p.36, l.14-18). Please see further discussion below.

Response to detailed comments:

YH: P3, L5. Note there are methods, such as latent heat nudging and particle filter, that make use of cloud and precipitation info in data assimilation.
AR: Thank you for mentioning this. We have added a sentence at the end of the paragraph: "Methods that directly make use of cloud or precipitation information in data assimilation, such as latent heat nudging or particle filters (e.g. Bannister et al., 2020), have yet to be implemented in global atmospheric reanalyses." (p.3, l.12-14)

R2: Page 4, l23: might it be clearer to say '… involved changes in the cloud fields which are much larger …'?
AR: Changed as suggested.

YH: P4, L31. Another benefit of simulator, if properly configured, is that it also addresses sampling consistency issue.
R: We agree. We have added a sentence to clarify our reasoning: "Use of a satellite simulator could address sensitivity and sampling biases for easier comparison with observations; however, it could also obscure inter-reanalysis differences in cloud types that are not well observed and complicate analysis of cloud radiative effects in each reanalysis." (p.5, l.16-18)

R2: Page 4, l32: suggest '… we stress that most …' without 'the'.
AR: Changed as suggested.

YH: P4, L33. I'm surprised to read that the aim is stated to be "qualitative" – despite many quantitative – why?
AR: We included quantitative comparisons amongst the reanalyses, and some with respect to OLR/LWCRE, but had focused on qualitative comparisons with respect to cloud observations (e.g. the approximate height, thickness, and distribution of anvil clouds in the time-mean tropical-mean, as opposed to the amount of cloud water or the magnitude of cloud fraction). One exception, of course, is Fig 2 which does use simulator output from MERRA-2, as well as the contour overlays in the revised Fig 1. Following the revision of Fig 1 (see above), we have changed this sentence to read: "Accordingly, comparisons between reanalysis products and satellite cloud observations in this paper should be interpreted with care." (p.5, l.18-19)

R2: Page 5, Table 1 / section 2.1: Table 1 provides a useful "at a glance" summary of the characteristics of the different observation datasets. There would be much to be said for extending it by the 5 or 6 lines needed to add equivalent details for the different reanalyses. I take the point made in section 2.1 that this paper provides detailed information of key aspects regarding cloud etc. and that other reviews have covered more general information, for those wishing to spend the time to track it down, but a brief summary set of 'vital statistics' would reduce the reliance the paper is otherwise placing upon a reader's prior knowledge of the reanalyses.

AR: Thank you for this suggestion. Because the most relevant information for the reanalyses differs from that for the observations, we have added a separate table summarizing key details of the reanalyses (Table R1) to section 2.1 of the manuscript.

Reanalysis	Model	Model Grid	HCC[a]	Profiles[a]	Fluxes[a]	Reference
ERA5	IFS 41R2 (2016)	N320 (∼31 km) 137 levels	$\sigma < 0.45$ 1-hourly	T, q, z, CC, I/LWC 3-hourly	TOA, RHR 12-h forecasts	Hersbach et al. (2020)
ERA-Interim	IFS 31R2 (2007)	N128 (∼79 km) 60 levels	$\sigma < 0.45$ 6-hourly	T, q, z, CC, I/LWC 6-hourly	TOA, RHR 12-h forecasts	Dee et al. (2011)
JRA-55	JMA GSM (2009)	N160 (∼55 km) 60 levels	$p < 500$ hPa 3-hourly	T, q, z, CC, I/LWC 6-hourly	TOA, RHR 6-h forecasts	Kobayashi et al. (2015)
MERRA-2	GEOS 5.12.4 (2015)	C180 (∼50 km) 72 levels	$p < 400$ hPa 1-hourly	T, q, z, CC, I/LWC 3-hourly	TOA, RHR 3-h forecasts	Gelaro et al. (2017)
CFSR	NCEP CFS (2007)	F288 (0.3125°) 64 levels	$p < 400$ hPa 6-hourly	T, q, z, CWC 6-hourly	TOA, RHR 6-h forecasts	Saha et al. (2010)
CFSv2	NCEP CFS (2011)	F440 (0.2045°) 64 levels	$p < 400$ hPa monthly	CWC monthly	TOA monthly	Saha et al. (2014)

[a] Climatological means of HCC, CC, CWC (or I/LWC), and TOA fluxes from all reanalyses are calculated from monthly mean products.

Table R1: Summary of reanalysis products. HCC stands for high cloud fraction; CC for cloud fraction; CWC for cloud water content and I/LWC for separate ice and liquid water contents; TOA for top-of-atmosphere fluxes (shortwave and longwave; clear-sky and all-sky); RHR for radiative heating rates (shortwave and longwave; all-sky). We use CFSR products for 1980–2010, CFSv2 for 2011–2014, and all other reanalysis products for 1980–2014.

YH: P6, L27; P13 L26. Note the latest CERES data includes a version of clear-sky values, computed using the same clear-sky definition as in GCM [Loeb 2019].

AR: Thank you for bringing this to our attention. We have replaced CERES EBAF Ed4A with CERES EBAF Ed4.1 throughout the paper, with reference to Loeb et al. (2020) and the appropriate dataset citation (see Table 2; also p.5 l.30-31 and p.13 l.19-21). We have continued using the 'adjusted' fluxes from SYN1Deg for the analyses based on daily data.

R2: Page 7, l3: do you intend 'specific heat constant' rather than 'heat capacity'?

AR: Thanks for noticing this; we have changed it to 'specific heat capacity'.

YH: P7, L15, Why linear with ln(p) instead of p?

AR: This approach was adapted from code for identifying the tropopause height and interpolating to isentropic surfaces, for which it is advantageous to interpolate temperature

and height in $\ln(p)$ (or z), rather than in pressure coordinates directly. We have tested the sensitivity of the LZRH statistics to this choice and find little influence on the results (see Fig R6 for comparisons using the ERA5 and ERA-Interim products from 2005). As using $\ln(p)$ produces a slightly smoother distribution for ERA-Interim, we make no change to the method.

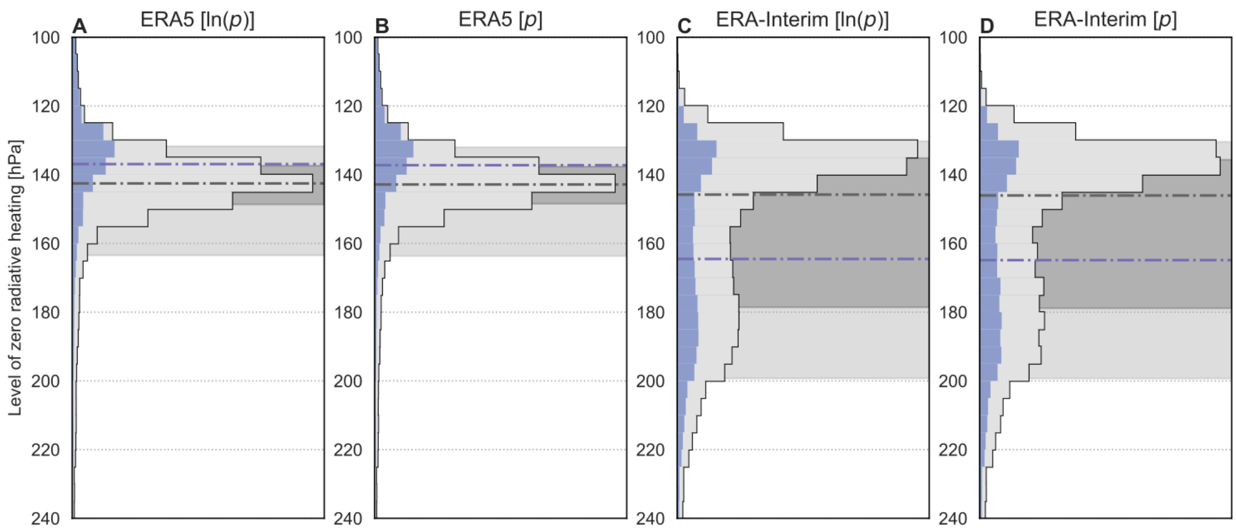

Figure R6: Distributions of LZRH locations in pressure calculated by conducting the interpolation (A,C) linearly in $\ln(p)$ versus (B,D) linearly in p for (A,B) ERA5 and (C,D) ERA-Interim during 2005. Distributions for Q4 based on the LWCRE are shown in light purple. The median for each distribution is marked by the dash-dot line (purple for Q4; grey for the full distribution); the middle 50% (dark grey shading; 25th to 75th percentile) and middle 80% (light grey shading; 10th to 90th percentile) are marked in each panel.

YH: P9, L8. Note that cloud top temperature (CTT) is another potential cause of (compensating) errors.

AR: Thank you for mentioning this. We have added a sentence, so that the text now reads: "Bechtold et al. (2014) reported that changes to parameterized convection in the ECMWF atmospheric model implemented between ERA-Interim and ERA5 yielded lower biases against observed brightness temperatures in land convective regions, especially for channels sensitive to the upper troposphere. However, as differences in cloud top temperatures between the two model versions could also influence the simulated brightness temperatures, these lower biases cannot be directly attributed to changes in HCC." (p.8, l.28-32)

YH: P11, L22 and Fig. 4. Are the CWC averaged over only cloudy profiles or over both cloudy and clear profiles? Consistently between all the reanalyses? Both averages would be of interest to compare.

AR: All reanalysis CWCs evaluated in this paper are grid-scale, not in-cloud products. We agree that both averages would be interesting to compare, but with length already an issue we only examine the grid-scale products in this paper.

R2: Page 14, Fig5 caption: 'with values for OLR listed above …' actually look as though the OLR mean values on the Figure are beneath?

AR: Yes, you are correct, and we have changed the caption accordingly. Please note that we have changed this figure (1) to add tropical-mean values for clear-sky OLR (at upper left), (2) to show contours for clear-sky OLR rather than LWCRE, and (3) to use CERES EBAF (updated to Ed4.1 as noted above) as the benchmark with 2001-2014 as the comparison period instead of using MRM as the benchmark with 1980-2014 as the comparison period. We still show area-mean values for LWCRE at the upper right of each panel (Figure R2).

YH: P15, Fig. 6. How is the purple line drawn exactly?

R: The purple line is the 75th percentile of all LWCREs included in the distribution (daily-mean products on a 1° grid between 10°S and 10°N from 1 January 2001 through 31 December 2010), meaning that 25% of the gridded daily-mean LWCREs are greater than this value. This value is then used as the threshold for selecting the 'Q4' convective subset in later analyses.

R2: Page 15, Fig 6 caption: 'is marked in the upper row.' Does this refer to the violet lines with numbers beside them in A, C-G?

AR: Yes; we have changed the caption accordingly.

R2: Page 15, l6: is 'are analogous to scatter plots containing millions of points' a roundabout way of saying 'represent a 2-dimensional probability density function'?

AR: Yes; however, we have found that the analogy to scatter plots is helpful when introducing this type of plot. We have changed this to read "two-dimensional frequency distributions analogous to scatter plots", omitting "containing millions of points" (p.15, l.18-19)

R2: Page 17, l5: 'presumably owing' reads a little loosely to a reviewer. But more precisely, at the bottom of page 16 the point has been made that MERRA-2 can persist large cloud fraction for declining cloud water, which implies reduced in-cloud water contents that might well lead to different LWCRE. It is thus unclear when the issue of characteristic lifetimes appears in the text whether this is meant to have been inferred from the differences in in-cloud water content or a separate (and presumably verifiable) behaviour of the different schemes discussed that is however (not shown). This sentence would benefit from clarification.

AR: Yes, this sentence was not worded well. We have changed it to read "Although the treatment of prognostic cloud fraction used in MERRA-2 is conceptually similar to that used in JRA-55 (Appendix A1), JRA-55 and MERRA-2 produce very different relationships between cloud fraction and condensate. Tuning efforts to increase the amount of cloud ice in the upper troposphere in MERRA-2 were motivated by a desire to improve OLR (recognizing that convective detrainment altitudes are too low in GEOS-5, the developers accepted overestimating cloud ice to get OLR right) and upper tropospheric humidity (Molod et al., 2015). The anvil cloud fraction was then kept small relative to the cloud ice content to prevent a worsening of the SWCRE as the LWCRE was increased." We have also corrected some descriptions of the MERRA-2 model in the preceding sentences. (p.17, l.22-30)

R2: Page 17, l13: 'more than 140Wm-2' seems a bit redundant when sitting beside 'from -100 to +40 Wm-2'

AR: We have removed the phrase 'more than 140 W m^{-2}'.

YH: P17, L30. OLR vs. CRE – this seems significant methodological difference. What's the rational to use CRE here?

AR: Thank you for asking this question. The initial rationale for adopting LWCRE, like the use of $\ln(p)$ above, was from other work; however, on further thought the rationale from that study does not clearly apply here: OLR may indeed be a better choice. We have checked the sensitivity of the conditional composite and distribution results to using LWCRE instead of OLR. The results indicate that there is little sensitivity to this choice for the inner tropical band (10°S–10°N) that we focus on (see, e.g., Figure R7).

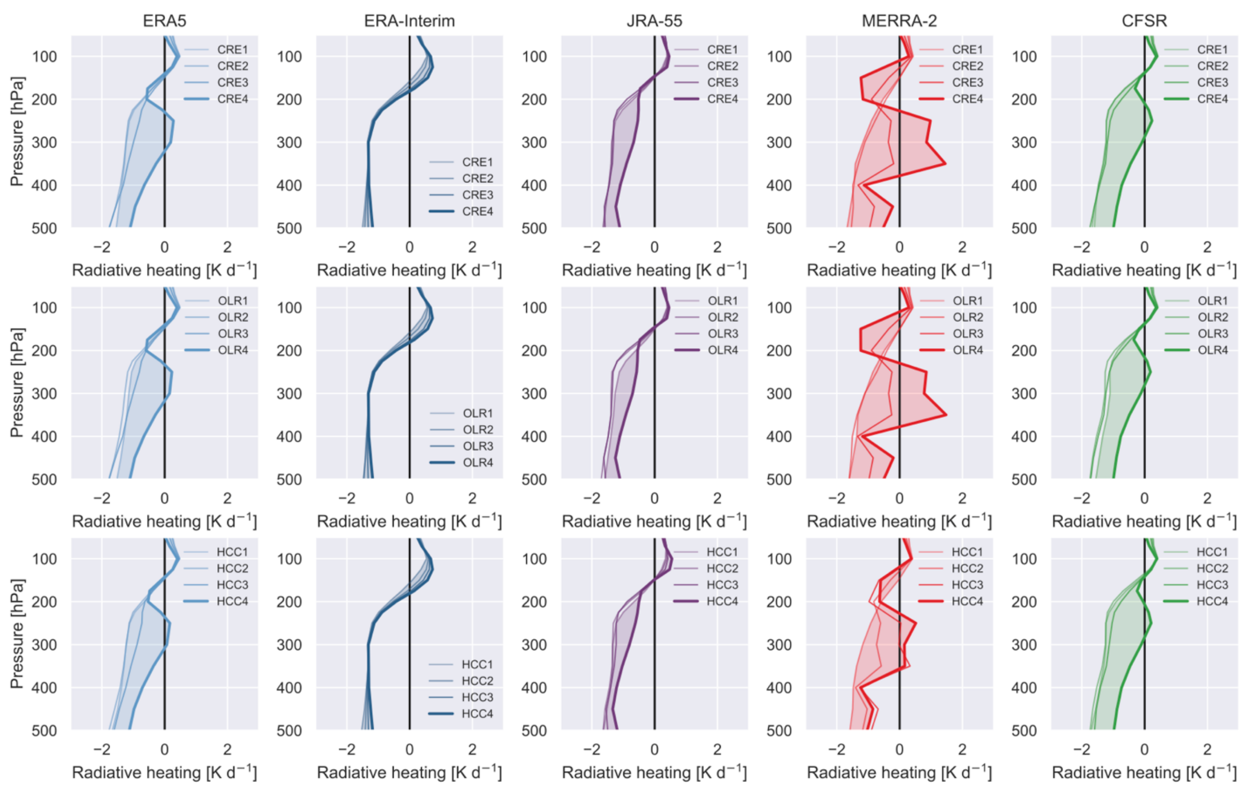

Figure R7: Composite mean profiles of daily-mean radiative heating rates as a function of pressure for the first through fourth quartiles (Q1–Q4) based on longwave cloud radiative effect (upper row; CRE1–CRE4), outgoing longwave radiation (centre row; OLR1–OLR4), and high cloud fraction (lower row; HCC1–HCC4) in the inner tropics (10°S–10°N) based on (left-to-right) ERA5, ERA-Interim, JRA-55, MERRA-2, and CFSR during 2001--2010. Here Q1 refers to the bottom quartile (weak LWCRE, large OLR, small HCC) and Q4 to the top quartile (strong LWCRE, small OLR, large HCC).

Using the bias-corrected Cramér's V (ϕ_c; Bergsma, 2013), which tests agreement between two categorical variables, we find that the data points selected for Q4 are extremely similar

between CRE and OLR, with $\phi_c > 0.9$ for each individual data set. Interpretation of ϕ_c is analogous to that for absolute linear correlations between numerical variables, with a value of 0 indicating no relationship and a value of 1 indicating perfect agreement. The overall quartile classification as a whole is also similar, with ϕ_c ranging from 0.7 (JRA-55) to 0.82 (MERRA-2). Given this similarity, particularly with Q4 as our primary condition for data selection, we prefer to limit changes by continuing to use LWCRE instead of switching the condition to quantiles of OLR. This choice also fits well with the existing presentation, since the threshold values for LWCRE Q4 are already marked in Figure 6 of the original submission (now Figure 7). We have noted the lack of sensitivity to choosing LWCRE versus OLR in the text (p.8, l.3-4; p.18, l.24-25)

YH: P18, Fig. 7. I am surprised to see the lack of distinctions in the ERAi results here, reminiscent of fig. 10e of Zhang et al. [2017]. Some basic radiative signatures such as cloud top cooling and cloud bottom warming are totally missing. May this be related to the use of CRE as a state indicator - it may fail to identify cloud effect due to clear-sky bias difference (see comments above)? Would it be useful to simply use cloud fraction instead to identify the regimes (Q1-4)? How does cloudy heating rate profile compare to clear-sky in this reanalysis?
AR: We initially did construct the composites based on high cloud fraction rather than LWCRE and have also tried OLR (Figure R7). The lack of distinction in ERA-Interim is a common feature in all three approaches, and ERA-Interim is clearly different from the other reanalyses in this regard. The results are more sensitive to replacing CRE with high cloud cover when constructing the quantiles than they are to replacing CRE with OLR, with ϕ_c ranging from 0.4 (MERRA-2) to 0.6 (CFSR) for the HCC classification relative to the CRE classification. Differences are especially stark for Q4, where the MERRA-2 results differ quite a bit ($\phi_c \sim 0.3$; consistent with a relatively weak relationship between CWC and cloud fraction) but the CFSR results are hardly altered at all ($\phi_c \sim 0.9$; consistent with cloud fraction being explicitly tied to CWC in the large-scale cloud parameterization). Given these different relationships between CWC and HCC, as well as different lower bounds for defining the 'high cloud' layer (from $p < 500$ hPa to $p < 400$ hPa), we find LWCRE (or OLR) preferable to high cloud fraction for this purpose.

We have added a few sentences at the end of section 2.3 to summarize our responses to these two comments: "Results are very similar for ranked quartiles of all-sky OLR, with OLR reversed so that Q4 corresponds to the smallest values of OLR. Using HCC instead of LWCRE produces more substantial differences, particularly for MERRA-2. Given discrepancies in the precise definition of HCC across reanalyses (Table 1) and the difficulty of defining an appropriate observational benchmark for HCC, we judge HCC less suitable for this purpose. We select LWCRE rather than OLR for convenience of presentation." (p.8, l.3-8)

YH: P19, Fig. 8. Is it LW or net radiative heating that is used to define LZRH and the relevant results?
AR: The LZRH is defined based on net radiative heating (SW+LW, all-sky). We have clarified this information in both section 2.3 (p.7, l.30-33) and section 4.2 (p.20, l.4-5).

YH: P20, L20. Isn't it the diabatic heating (instead of radiative only) that better inferences ascent/descent? Why focused on radiative?

AR: Yes, the ascent / descent is balanced by the total diabatic heating. However, overshooting convection that reaches the tropopause (or even the LZRH) is rare enough that ascent through the TTL is mostly balanced by radiative heating. Temperature tendencies due to shear-flow turbulence (e.g. Flannaghan and Fueglistaler, 2011) are poorly constrained and differ substantially among reanalyses (Wright and Fueglistaler, 2013) but become comparable to convective terms near the tropopause, especially in some regions and seasons. To avoid these complications, some studies have used radiative heating alone to represent vertical transport in this region (e.g. Tzella and Legras, 2011; Tissier and Legras, 2016). These studies use satellite imagery to represent the convective sources of trajectories, thus avoiding uncertainties in whether the reanalysis puts convection in the correct locations with the correct depths and at the correct times. Focusing on radiative heating rates serves a similar purpose here, as it allows us to keep the scope of the paper manageable, avoiding some finer details of the convective and free-atmosphere turbulence parameterizations that are better treated elsewhere. Regardless of whether the all-sky radiative heating or total heating is used, the LZRH is a critical level in that convective influences on the lower stratosphere should be dominated by detrainment occurring at or above the LZRH.

YH: P21 "Possible origins". The discussions in this section don't distinguish cause and effect of previously presented cloud biases. Maybe worth some clarification and discussion here about this.
AR: Yes, this is a good idea. We have added: "We cannot fully distinguish between causes and effects. All of the variables we examine in this section are intimately connected to cloud and convection processes, so that differences in these variables may indicate the causes of cloud biases, reflect the effects of those biases, or both of the above. To address this, we link differences in the examined variables to differences in model parameterizations or data assimilation procedures whenever possible. Although we cannot unequivocally tie each bias to a distinct origin of this type, this information may be helpful both for understanding differences between the reanalyses and for highlighting potential targets for improvement in the reanalysis systems." (p.22, l.19-24)

R2: Page 23, Table 2 caption: 'all data points' (plural)?
AR: Yes; corrected.

R2: Page 23, ll2-13: To me, lines 10-13 'Note … independent.' seem to follow more naturally from the statement of similarity that ends on line 4 '(Table 2).'
AR: Changed as suggested.

R2: In addition, the lines 4-7 seem to spend a lot of time simply repeating the data that readers can see in Table 2 whereas I think they would add more if they pulled out what seems to be the key message by showing the differences [Q4 –All] that appear scattered either side of the observed 1K. e.g. 'CFSR exhibits the weakest increase in SST (0.7K) between mean cloud and high …' or 'observation …, assigns a mean value to Q4 that is 1K warmer than the tropical mean.'
AR: Changed as suggested (p.22, l.31 – p.23, l.2)

YH: P24, L5. The way the current plot is made makes it difficult to discern the "kink".

AR: We have added distributions of the three components of MSE at 850 hPa, 500 hPa, and 300 hPa for Q4 from each reanalysis (Figure R4), along with dashed yellow lines to highlight those three levels. The kink is located at the intersection of the thick purple line and the lowest dashed yellow line. We have added the sentence: "This kink arises because the Q4 profile in JRA-55 has a warm bias at 850 hPa (+0.4 kJ kg^{-1} relative to ERA5; Fig 11B, lower row) but a cool and dry bias at 900 hPa (–1.0 kJ kg^{-1}; not shown)." The distributions at 900 hPa are omitted from the figure because they only appear in this explanation, whereas the biases at 850, 500, and 300 hPa are discussed in more detail in the text.

R2: Page 25, l5: The first half of the first sentence would be better if merged into the following sentence 'Distributions of 500hPa grid-scale vertical velocity (w) for the whole tropics (Figure 9C) …' and the second half similarly into line 2 of P26.

AR: Changed as suggested. We have also added a paragraph break between the discussion of 500-hPa vertical velocity and the discussion of mid-tropospheric RH.

R2: Page 26, l16-18: there is a lot of repetition that could be reduced by swapping the order in line 16, for instance, 'so that plumes are only permitted to reach the upper troposphere when entrainment rates are small, that is potentially smaller than the … Tokioka parameter.'

AR: We have changed this to "For MERRA-2 this is consistent with the application of a Tokioka-type entrainment condition (Bacmeister and Stephens, 2011): entrainment rates smaller than a randomly-selected minimum (the Tokioka parameter) are disallowed. For small values of RH, entrainment is efficient in diluting the updraft, so that plumes can only reach the upper troposphere when the entrainment rate is small. The Tokioka condition thus tightens the preference for deeper convection to occur in more humid environments." (p.26, l.27-31)

YH: P26, section 5.2 and Fig 11. Besides the confusing way the figure is presented as noted above, I find the discussion here doesn't show enough recognition of the cloud position with respect to the respective levels focused (100 and 150 hPa). A basic signature of clouds is cloud top cooling and bottom warming. The sign and magnitude of the cloud radiative impact is strongly dependent on where the clouds are placed.

AR: We have expanded on this discussion making reference to the former Fig 12 (now Fig 13), which clarifies the difference in cloud placement between strong positive and strong negative heating rates at 150 hPa. Specifically, we have revised the presentation of the results, and have included the following text at the beginning of the section: "The TTL is located above the typical levels of convective detrainment (200~300 hPa; Fig. 4), with a lower boundary near the LZRH (140~150 hPa; Fig. 9A). Clouds in this layer are most often associated with slow radiatively-balanced ascent, and occasionally with very deep convection that penetrates into the TTL (e.g. Fueglistaler et al., 2009). These two cloud populations are distinguished by their CWCs (smaller for in situ cirrus; larger for convective anvil clouds) and associated radiative heating rates (weak radiative heating for slow ascent; strong cloud-top cooling for most anvil clouds, possibly supplanted by strong warming for clouds reaching very high altitude). The essential radiative signature of cloud-top cooling and cloud-base warming can be seen by comparing the radiative heating profiles in Fig. 8A–E and the vertical locations of the anvil cloud layers in Fig. 4F.

Radiative heating thus helps to distinguish different types of clouds in the lower part of the TTL: (1) in situ cirrus clouds, which are associated with weak positive heating rates balancing large-scale ascent (i.e. close to the 'spine' of the plot); (2) deep convection that detrains near the base of the TTL, which is associated with large CWCs and negative radiative heating (the left 'wing'); and (3) deep convection that detrains inside the TTL, which is associated with large CWCs and positive heating rates (the right 'wing'). The latter two types are distinguished by both the depth and water content of the anvil cloud (Fig. 13), and the third type grows progressively rarer with increasing altitude. Compositing on RH in addition to radiative heating helps to highlight some differences and unrealistic features among the reanalyses, as discussed below." (p.27, l.7 – p.28, l.8)

YH: P29, L31. "systemic" => "artificial"?
AR: Changed as suggested.

YH: P29, L32 and Fig. 13. A striking feature is that OLR doesn't seem "jumped" despite of the cloud fraction jump! How could cloud cover change be consistent with OLR and CRE with regard to long-term trend but inconsistent with regard to this jump?
AR: Yes, this is one of several perplexing features of CFSR that we have so far been unable to pin down. One likely contributor is that improvements in humidity near the tropical tropopause (Figure R8A-C) led to increases in HCC above and outside of the core convective regions (cf. Figure R9A-C). Although CFSR/CFSv2 does not provide a vertically resolved estimate of cloud fraction, we do find increases in cloud water content near the tropopause and outside the deep tropics (Figure R8D-F). Cloud fractions in CFSR are determined primarily as a function of CWC (with RH a contributing factor), so that these differences (and/or any undocumented changes in the relationship between CWC/RH and cloud fraction) could result in large changes in HCC but relatively little change in LWCRE. Another possibility (not mutually exclusive) is that tuning of the CFSv2 model following the resolution and physical parameterization changes (e.g. the introduction of McICA) smoothed out the discontinuity in OLR despite the jump in high cloud fraction. In this sense, it is interesting to note that there was a jump of more than 7 W m^{-2} in the net CRE between the last four years of CFSR and the first four years of CFSv2, indicating substantial changes in the SWCRE (Figure R9H). These changes must include the effects of model changes targeting marine low-level clouds (Saha et al., 2014); however, it is clear from the spatial distribution that reductions in planetary albedo are concentrated in places where high clouds are more prevalent (including canonical deep convective regions and locations where increases in HCC are relatively large). It is unclear how increases in HCC and upper-level CWC lead to an unchanged LW effect and a *reduced* planetary albedo – we have double- and triple-checked the data processing history and found no obvious errors. Indeed, the fluxes make sense internally for both CFSR and CFSv2; it is only when we evaluate the changes at the transition that this inconsistency crops up, implicating changes in the model. Despite the lack of a clear explanation, we have added these figures and a tighter version of this text as an appendix to the paper to support the discussion of discontinuities at the CFSR-CFSv2 transition. (Appendix B; p.43-45)

Some unique behaviors in CFSR also seem to emerge from the bias correction scheme. These features show up as 'blips' in the time series after every production stream transition, as the model gradually imprints its own bias on any variables that are not sufficiently constrained by data assimilation (the spin-up period seems to be just about long enough to reset water vapor in the stratosphere to zero as shown by Davis et al., 2017; a similar issue might affect clouds, especially at upper levels). This could explain why we see such a large difference in these variables for the 2010 bridge year, since that bridge year was run without spin-up (see Long et al., 2017). Unfortunately, it is not documented whether the model used for 2010 included any changes relative to the original model or bias correction scheme.

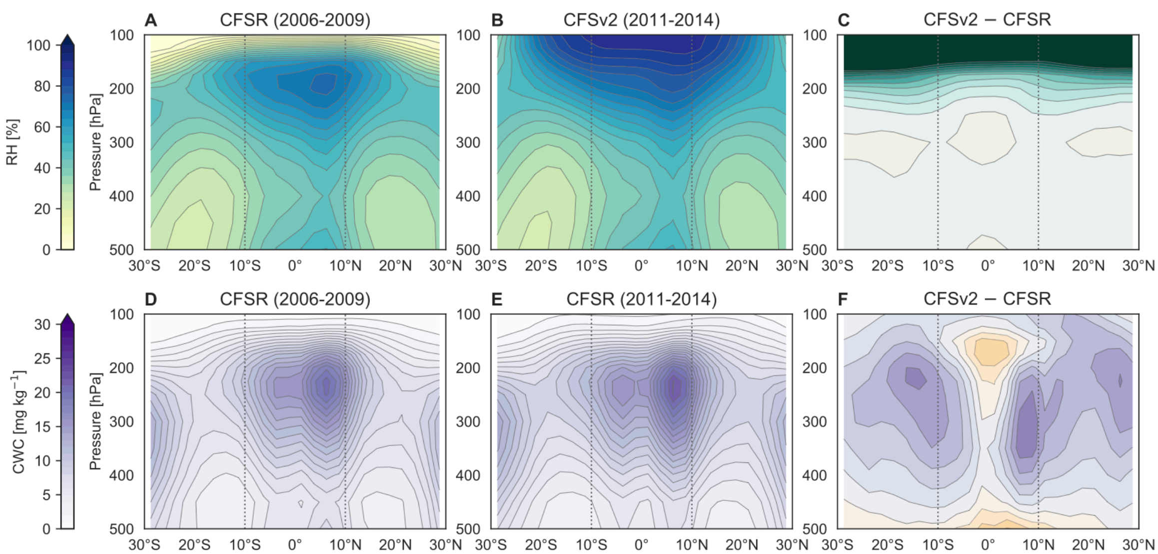

Figure R8: Upper row: Zonal-mean distributions of RH based on (A) the last four years of the original CFSR (2006–2009) and (B) the first four years of CFSv2 (2011–2014), along with (C) differences between the two products. Lower row: as in the upper row, but for CWC.

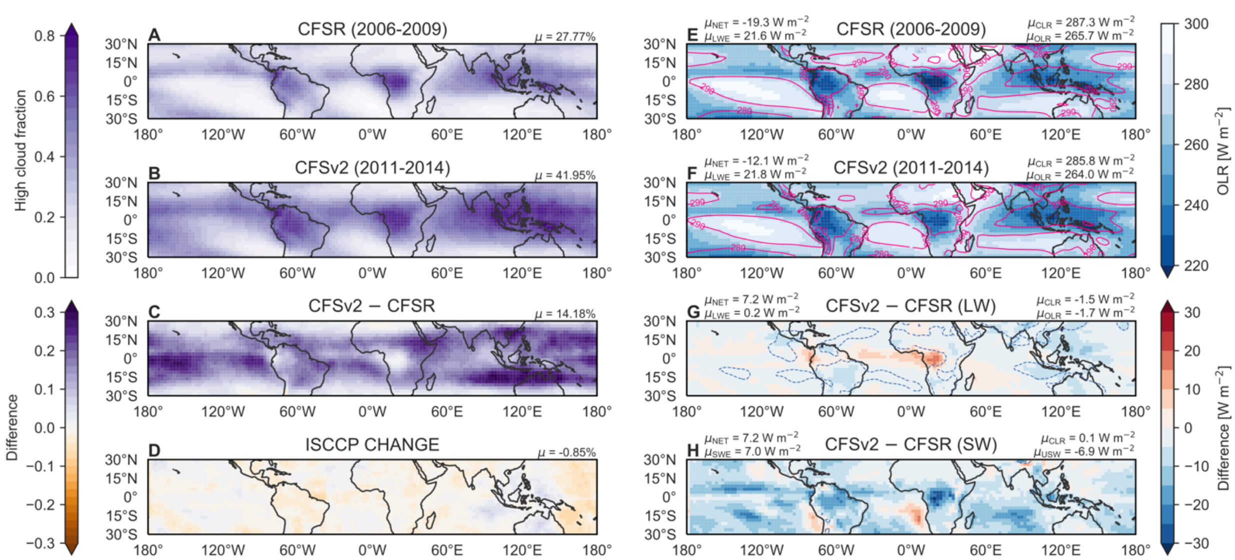

Figure R9: At left: distributions of high cloud fraction based on (A) the last four years of the original CFSR (2006–2009) and (B) the first four years of CFSv2 (2011–2014), along with (C) the difference between CFSv2 and CFSR. The change in ISCCP HGM high cloud fraction between the 2006–2009 mean and the 2011–2014 mean is shown for context in panel (D). At right: as in the left column, but for all-sky (shading) and clear-sky (contours) OLR. The change in all-sky and clear-sky upward SW flux between CFSR and CFSv2 is also shown in panel (H). Tropical mean (30°S-30°N) values of HCC (or ΔHCC) are listed at upper right of panels (A) through (D). Tropical mean values of OLR, clear-sky OLR, LWCRE, and net CRE (or corresponding Δ values) are listed at upper right (OLR and clear-sky OLR) or upper left (LWCRE and net CRE) of panels (E) through (G). These are replaced with mean changes in TOA upward SW fluxes in panel (H).

YH: Also, the long-term trends seem similar among the reanalyses – should this be taken seriously as a sign of real trend in nature? It is important to reason and caution whether we can use these reanalyses for studying climate trend in this critical region. It should be noted that the all-sky OLR trend appears to contradict the FAT hypothesis [Hartmann & Larson 2002].
AR: We are skeptical of the trends, especially without more robust independent evidence from observations and extension to other periods. As noted in the text, it is not surprising that reanalyses produce declining trends in clear-sky OLR over periods ending in 2014, and the further contribution to decreases in all-sky OLR from increases in high cloud cover is not consistently supported by observations. It is a good idea to mention the FAT hypothesis for context here, although the all-sky OLR trend only contradicts FAT to the extent that it cannot be explained by changes in high cloud cover. We are also unsure how much we should expect reanalyses subject to a changing observing system over time to follow FAT, especially given changes in the strength of constraints on temperature structure around the tropopause (Tegtmeier et al., 2020). We have added the text: "Decreasing trends in all-sky OLR seem at first glance to contradict the fixed anvil temperature (FAT) hypothesis of Hartmann and Larson (2002). However, increasing trends in HCC are qualitatively consistent with decreases in all-sky OLR above and beyond those in clear-sky OLR; reductions in all-sky OLR therefore do not necessarily imply reductions in anvil cloud emission temperatures. Indeed, with the exception of CFSR/CFSv2 (affected by discontinuities around the CFSR–CFSv2 transition as discussed in Appendix B) and ERA5 (for which trends are small), relatively large decreasing trends in all-sky OLR among reanalyses reflect relatively large increases in LWCRE, which are linked in turn to increases in HCC." (p.32, l.17-23)

YH: P30, L23. The clear-sky OLR change described sounds very interesting and ought to be shown. Relevant to the above point, another important question the reanalyses may or may not answer is whether broadband fluxes, either clear- or all-sky, may be useful for climate change monitoring. As shown by Huang & Ramaswamy [2009, Fig. 5], there may be intrinsic compensation between greenhouse gas forcing and Planck response that results in no trend signal. This point, together with the above one, is worth noting and discussing here.
AR: We have added a panel showing the evolution of anomalies in clear-sky OLR (Fig. R5). We have expanded the text here to read: "Decreasing trends in clear-sky OLR suggest that increases in atmospheric greenhouse gas absorption outpaced increases in the effective emission temperature in the tropics over this period, changes that may be explained by the so-called

`hiatus' in surface warming during the early 2000s (Song et al., 2016). Prescribed greenhouse gas concentrations increased throughout this period (Fujiwara et al., 2017, their Fig. 4), even as observed surface temperatures cooled or stayed roughly constant through much of the tropics (Kosaka and Xie, 2013). Although these trends should be interpreted with caution, their consistency with expectations may be a promising sign for the use of broadband OLR fluxes in climate monitoring, given the potential for compensating effects to damp signals of climate change in these fields (e.g. Huang and Ramaswamy, 2009)."

YH: P31, Fig. 13. Some of the time series apparently don't have zero mean. How are the anomalies defined?
AR: Anomalies are defined relative to the mean annual cycle during 2001-2014. This information is included in the caption and in the text at the beginning of section 6 (p.30, l.12-13).

R2: Page 33, Figure 14 caption: are the separation lines 'Solid grey' or 'Solid black'? (I do like the plot, though!).
AR: We have changed this to 'solid black'.

YH: P34, Summary. A general suggestion for this section is to reference the respective summary points to the relevant figures.
AR: We have added figure references to the text in section 7.

YH: P34, L20. It is striking to find the lack of agreement among the studies in terms of what direction cloud drives the LZRH. Can you discuss why and how would one elucidate this matter?
AR: We agree! This is a troubling discrepancy, not least as the recent ERA5 agrees with the other reanalyses rather than ERA-Interim, in contrast to what the observation-based calculations suggest. However, to answer this question beyond the short discussion at the end of this paragraph would require a detailed evaluation of the relative uncertainties and deficiencies associated with the observational products (all subject to sampling biases and assumptions about cloud properties) that lies beyond the scope of this paper. We are aware of colleagues who are digging into this question and eagerly await their results.

R2: Page 36, l18: 'occur in …' rather than 'into'?
AR: Yes, thank you.

YH: P36, L29. Cloud top temperature, as related to in some of the above comments, is perhaps another aspect to note.
AR: We have revised this paragraph to mention cloud top temperature in conjunction with cloud top height throughout.

R2: Page 36, l33: I found this sentence somewhat hard to digest, especially as a finale. I would suggest putting a stop in at 'in the reanalysis models.' then rewording the rest into a following sentence as appropriate.

AR: Changed as suggested. The final sentence now reads: "Further investigation along these lines may also consider how these features imprint upon more widely-used reanalysis products and model simulations that use reanalysis fields to drive atmospheric transport." (p.37, l.22-23)

YH: P37, Appendix. It may be worth reviewing the difference in assimilated data in this appendix as well. This is apparently relevant to the trend discussions (section 6) and potential affects climatology as well.

AR: With the exception of ERA5, differences in assimilated data among these reanalyses have been covered by Fujiwara et al. (2017) on conventional observations and satellite radiances, Long et al. (2017) on observations influencing temperature, Davis et al. (2017) on observations of water vapor and ozone, Tegtmeier et al. (2020) on TTL thermal structure (in this case including ERA5), and others. Given the range of observation types that may contribute to biases in clouds, OLR, and heating rates, we are unsure how to condense this information into a reasonable length for this paper (for reference, chapter 2 of the S-RIP report includes 28 pages on this topic). We prefer to direct readers to these other resources (and the ERA5 documentation now in press; Hersbach et al., 2020) instead. We have included a sentence giving these references on p.4 (l.15-17).

YH: P37, L25. What is liquid water temperature?

AR: Liquid water temperature is defined as the air temperature minus (L_v/c_p) * q_c, where L_v is the latent heat of vaporization, c_p is the specific heat capacity at constant pressure, and q_c is the cloud water content. We have added this clarification to the appendix (p.38, l.13).

R2: Page 42, l3: 'discrete' is redundant here as 'discretization' guarantees it!

AR: We have changed 'discrete' to 'predetermined'.

YH: P43, L1. Sufficient info to ensure reproducibility of the results should be included. Regarding the data sources, how were the data, such as ERA5 heating rates, obtained exactly, as they are not normally available from the webpages stated here? If scripts were used, it is useful to post a sample script and explain how relevant parameters, e.g., analysis vs. forecast and, if latter, forecast times and steps, are set. Moreover, are the these parameters set consistently for all the variables: heating rate and state variables such as cloud fraction, temperature, humidity, etc. from the same time steps?

AR: We have added information on the temporal resolution of each product in the data availability statement as well as in the new Table 1 (see Table R1 above). Heating rates and TOA fluxes are in all cases based on time-average forecast fields which are then aggregated into daily means, while other data are typically instantaneous outputs at 1-hourly, 3-hourly, or 6-hourly resolution. We have sub-sampled the ERA5 pressure-level analysis fields to 3-hourly resolution, which matches MERRA-2; all other vertically resolved fields (from ERA-Interim, JRA-55, and CFSR) are only provided 6-hourly. High cloud fraction sampling ranges from hourly (ERA5, MERRA-2) to 3-hourly (JRA-55) to 6-hourly (ERA-Interim, CFSR); this difference in sampling potentially impacts values along the y-axis in the joint distributions shown in Fig 6 (and Fig R4 above), but should not influence any other calculations in the paper.

Additional changes:

In addition to the above changes, we have replaced the July 2006–June 2007 CWC-RO profile of IWC in Figure 3 with a 2007–2010 mean profile based on 2C-ICE (Deng et al., 2015) and added one co-author. The profile based on 2C-ICE shows quantitative differences relative to the previous CWC-RO profile, but introduces no changes in interpretation. We elect to make this change for two reasons: (1) the longer period, which is consistent with the KG2009 cloud fraction profile and (2) a clearer data provenance and processing history.

We have also made changes for clarity and to shorten the text.

References:

Bacmeister, J. T. and Stephens, G. L.: Spatial statistics of likely convective clouds in CloudSat data, J. Geophys. Res. Atmos., 116, D04104, https://doi.org/10.1029/2010JD014444, 2011

Bannister, R. N., Chipilski, H. G., and Martinez-Alvarado, O.: Techniques and challenges in the assimilation of atmospheric water observations for numerical weather prediction towards convective scales, Q. J. Roy. Meteor. Soc., 146, 1–48, https://doi.org/10.1002/qj.3652, 2020

Bechtold, P., Semane, N., Lopez, P., Chaboureau, J.-P., Beljaars, A., and Bormann, N.: Representing equilibrium and nonequilibrium convection in large-scale models, J. Atmos. Sci., 71, 734–753, https://doi.org/10.1175/JAS-D-13-0163.1, 2014

Bergsma, W.: A bias correction for Cramér's V and Tschuprow's T, J. Kor. Stat. Soc., 42, 323–328, doi:10.1016/j.jkss.2012.10.002, 2013

Davis, S. M., Hegglin, M. I., Fujiwara, M., Dragani, R., Harada, Y., Kobayashi, C., Long, C., Manney, G. L., Nash, E. R., Potter, G. L., Tegtmeier, S., Wang, T., Wargan, K., and Wright, J. S.: Assessment of upper tropospheric and stratospheric water vapor and ozone in reanalyses as part of S-RIP, Atmos. Chem. Phys., 17, 12 743–12 778, https://doi.org/10.5194/acp-17-12743-2017, 2017

Deng, M., Mace, G. G., Wang, Z., and Berry, E.: CloudSat 2C-ICE product update with a new Ze parameterization in lidar-only region, J. Geophys. Res. Atmos., 120, 12 198–12 208, https://doi.org/10.1002/2015JD023600, 2015

Flannaghan, T. J. and Fueglistaler, S.: Kelvin waves and shear-flow turbulent mixing in the TTL in (re-)analysis data, Geophys. Res.Lett., 38, L02801, https://doi.org/10.1029/2010GL045524, 2011.

Fueglistaler, S., Dessler, A. E., Dunkerton, T. J., Folkins, I., Fu, Q., and Motte, P. W.: Tropical tropopause layer, Rev. Geophys., 47, RG1004, https://doi.org/10.1029/2008RG000267, 2009

Fujiwara, M., Wright, J. S., Manney, G. L., Gray, L. J., Anstey, J., Birner, T., Davis, S., Gerber, E. P., Harvey, V. L., Hegglin, M. I., Homeyer, C. R., Knox, J. A., Krüger, K., Lambert, A., Long, C. S., Martineau, P., Molod, A., Monge-Sanz, B. M., Santee, M. L., Tegtmeier, S., Chabrillat, S., Tan, D. G. H., Jackson, D. R., Polavarapu, S., Compo, G. P., Dragani, R., Ebisuzaki, W., Harada, Y., Kobayashi, C., McCarty, W., Onogi, K., Pawson, S., Simmons, A., Wargan, K., Whitaker, J. S., and Zou, C.-Z.: Introduction to the SPARC Reanalysis Intercomparison Project (S-RIP) and overview of the reanalysis systems, Atmos. Chem. Phys., 17, 1417–1452, https://doi.org/10.5194/acp-517-1417-2017, 2017

Hersbach, H., Bell, B., Berrisford, P., Hirahara, S., Horányi, A., Muñoz-Sabater, J., Nicolas, J., Peubey, C., Radu, R., Schepers, D., Simmons, A., Soci, C., Abdalla, S., Abellan, X., Balsamo, G., Bechtold, P., Biavati, G., Bidlot, J., Bonavita, M., De Chiara, G., Dahlgren, P., Dee, D., Diamantakis, M., Dragani, R., Flemming, J., Forbes, R., Fuentes, M., Geer, A., Haimberger, L., Healy, S., Hogan, R. J., Hólm, E., Janisková, M., Keeley, S., Laloyaux, P., Lopez, P., Lupu, C., Radnoti, G., de Rosnay, P., Rozum, I., Vamborg, F., Villaume, S., and Thépaut, J.-N.: The ERA5 Global Reanalysis, Q. J. Roy. Meteor. Soc., accepted manuscript, https://doi.org/10.1002/qj.3803, 2020.

Huang, Y. and Ramaswamy, V.: Evolution and trend of the outgoing longwave radiation spectrum, J. Climate, 22, 4637–4651, https://doi.org/10.1175/2009JCLI2874.1, 2009

Kolly, A. and Huang, Y.: The radiative feedback during the ENSO cycle: observations versus models, J. Geophys. Res. Atmos., 123, 9097–9108, https://doi.org/10.1029/2018JD028401, 2018

Kosaka, Y. and Xie, S.: Recent global-warming hiatus tied to equatorial Pacific surface cooling, Nature, 501, 403–407, https://doi.org/10.1038/nature12534, 2013

Long, C. S., Fujiwara, M., Davis, S., Mitchell, D. M., and Wright, C. J.: Climatology and interannual variability of dynamic variables in multiple reanalyses evaluated by the SPARC Reanalysis Intercomparison Project (S-RIP), Atmos. Chem. Phys., 17, 14 593–14 629, https://doi.org/10.5194/acp-17-14593-2017, 2017.

Reynolds, R. W., Smith, T. M., Liu, C., Chelton, D. B., Casey, K. S., and Schlax, M. G.: Daily high-resolution-blended analyses for sea surface temperature, J. Climate, 20, 5473–5496, https://doi.org/10.1175/2007JCLI1824.1, 2007

Saha, S., Moorthi, S., Wu, X., Wang, J., Nadiga, S., Tripp, P., Behringer, D., Hou, Y. T., Chuang, H., and Iredell, M.: The NCEP Climate Forecast System Version 2, J. Climate, 27, 2185–2208, https://doi.org/10.1175/JCLI-D-12-00823.1, 2014

Song, J., Wang, Y., and Tang, J.: A hiatus of the greenhouse effect, Sci. Rep., 6, 33315, https://doi.org/10.1038/srep33315, 2016

Stephens, G. L. and L'Ecuyer, T.: The Earth's energy balance, Atmos. Res., 166, 195–203, https://doi.org/10.1016/j.atmosres.2015.06.024, 2015

Tegtmeier, S., Anstey, J., Davis, S., Dragani, R., Harada, Y., Ivanciu, I., Pilch Kedzierski, R., Krüger, K., Legras, B., Long, C., Wang, J. S.,Wargan, K., and Wright, J. S.: Temperature and tropopause characteristics from reanalyses data in the tropical tropopause layer, Atmos. Chem. Phys., 20, 753–770, https://doi.org/10.5194/acp-20-753-2020, 2020

Tissier, A.-S. and Legras, B.: Convective sources of trajectories traversing the tropical tropopause layer, Atmos. Chem. Phys., 16, 3383–3398, https://doi.org/10.5194/acp-16-3383-2016, 2016

Tzella, A. and Legras, B.: A Lagrangian view of convective sources for transport of air across the tropical tropopause layer: distribution, times and the radiative influence of clouds, Atmos. Chem. Phys., 11, 12 517-12 534, https://doi.org/10.5194/acp-11-12517-2011, 2011

Wall, C. J., Hartmann, D. L., and Norris, J. R.: Is the net cloud radiative effect constrained to be uniform over the tropical warm pools?, Geophys. Res. Lett., 46, 12 495–12 503, https://doi.org/10.1029/2019GL083642, 2019

Wright, J. S. and Fueglistaler, S.: Large differences in reanalyses of diabatic heating in the tropical upper troposphere and lower stratosphere, Atmos. Chem. Phys., 13, 9565–9576, https://doi.org/10.5194/acp-13-9565-2013, 2013.

Differences in tropical high clouds among reanalyses: origins and radiative impacts

Jonathon S. Wright[1], Xiaoyi Sun[1], Paul Konopka[2], Kirstin Krüger[3], Bernard Legras[4], Andrea M. Molod[5], Susann Tegtmeier[6], Guang J. Zhang[7], and Xi Zhao[8]

[1]Ministry of Education Key Laboratory for Earth System Modeling, Department of Earth System Science, Tsinghua University, Beijing, China
[2]Forschungszentrum Jülich (IEK-7: Stratosphere), Jülich, Germany
[3]Department of Geosciences, University of Oslo, Oslo, Norway
[4]Laboratoire de Météorologie Dynamique, CNRS/PSL-ENS/Sorbonne Université/Ecole Polytechnique, Paris, France
[5]Global Modeling and Assimilation Office, NASA Goddard Space Flight Center, Greenbelt, Maryland, USA
[6]Department of Physics and Engineering Physics, University of Saskatchewan, Saskatoon, Canada
[7]Scripps Institution of Oceanography, La Jolla, California, USA
[8]Department of Atmospheric Sciences, Texas A&M University, College Station, Texas, USA

Correspondence: Jonathon S. Wright (jswright@tsinghua.edu.cn)

Abstract. We examine differences among reanalysis high cloud products in the tropics, assess the impacts of these differences on radiation budgets at the top of the atmosphere and within the tropical upper troposphere and lower stratosphere (UTLS), and discuss their possible origins in the context of the reanalysis models. We focus on the ERA5, ERA-Interim, JRA-55, MERRA-2, and CFSR/CFSv2 reanalyses~~, with MERRA included in selected comparisons~~. As a general rule, JRA-55 produces the smallest tropical high cloud fractions and cloud water contents among the reanalyses, while MERRA-2 produces the largest. Accordingly, longwave cloud radiative effects are relatively weak in JRA-55 and relatively strong in MERRA-2. Only MERRA-2 and ERA5 among the reanalyses produce tropical-mean values of outgoing longwave radiation (OLR) close to observed, but ERA5 tends to underestimate cloud effects while MERRA-2 tends to overestimate variability. ERA5 also produces distributions of longwave, shortwave, and total cloud radiative effects at top-of-atmosphere that are very consistent with observed. The other reanalyses all exhibit substantial biases in at least one of these metrics, although compensation between the longwave and shortwave effects helps to constrain biases in the total cloud radiative effect for most reanalyses. The vertical distribution of cloud water content emerges as a key difference between ERA-Interim and ~~the~~ other reanalyses. Whereas ERA-Interim shows a monotonic decrease of cloud water content with increasing height, the other reanalyses all produce distinct anvil layers. The latter is in better agreement with observations and yields very different profiles of radiative heating in the UTLS. For example, whereas the altitude of the level of zero net radiative heating tends to be lower in convective regions than in the rest of the tropics in ERA-Interim, the opposite is true for the other four reanalyses. Differences in cloud water content also help to explain systematic differences in ~~diabatic ascent~~ radiative heating in the tropical lower stratosphere among the reanalyses. We discuss several ways in which aspects of the cloud and convection schemes impact the tropical environment. Discrepancies in the vertical ~~profile of moist static energy~~ profiles of temperature and specific humidity in convective regions are particularly

noteworthy, as this metric is based exclusively on variables that these variables are directly constrained by data assimilation, widely used, and feed back to convective behaviour through their relationships with thermodynamic stability.

1 Introduction

Tropical high clouds play a central role in climate via their ability to modulate influences on the radiation budget, altering both the reflection of incoming solar radiation and the atmospheric absorption of longwave radiation emitted by the Earth's surface (Trenberth et al., 2009; Dessler, 2010). The net effect of an individual cloud on the radiation budget depends on several factors, including the type, phase, height, and microphysical characteristics of the cloud (Stevens and Schwartz, 2012). These features are difficult to parameterize, so that the integrated radiative impacts of clouds remain poorly represented in global models (Bony et al., 2015), including those used to produce atmospheric reanalyses (Dolinar et al., 2016; Li et al., 2017).

Clouds, circulation, and sea surface temperature (SST) are strongly coupled in the tropics (e.g. Hartmann and Michelsen, 1993; Emanuel et al., 1994; Fu et al., 1996; Su et al., 2011). These coupled interactions transport energy away from convective regions, which tend to be anchored over the warmest SSTs, into subsidence-dominated regions where SSTs are usually cooler. Associated tracer transports have extensive influences on humidity, ozone, and other constituents in the upper troposphere (Folkins et al., 2002; Jiang et al., 2007; Fiehn et al., 2017; Pan et al., 2017), while momentum transport, latent heat release, and radiative effects modulate circulation patterns in both the troposphere and stratosphere (LeMone et al., 1984; Carr and Bretherton, 2001; Lane and Moncrieff, 2008; Geller et al., 2016; Kim et al., 2017). Changes in precipitation are governed to leading order by the balance of changes in radiative cooling and condensational heating in the atmosphere (O'Gorman et al., 2011), both of which are intimately connected with the distribution and properties of high clouds. The radiative and condensational heating effects of clouds have also been shown to influence atmospheric water budgets associated with a wide range of climatological phenomena, including the El Niño–Southern Oscillation (e.g. Posselt et al., 2011), the Madden–Julian Oscillation (e.g. Anber et al., 2016; Cao and Zhang, 2017), and the South Asian summer monsoon (e.g. Wang et al., 2015).

Given the influential role of high clouds in the tropical climate system and the complexity of their interactions with other variables, evaluation and intercomparison of reanalysis cloud products serves several purposes. First, reanalyses offer global coverage at relatively high resolution and regular intervals. It is therefore useful to assess the level to which reanalysis cloud and radiation products may be considered 'realistic'. Second, systematic differences in cloud fields can be used to diagnose problems or points of concern in the atmospheric model. Detailed evaluation of these biases can thus inform both interpretation of model outputs and future efforts toward model development. Differences in cloud fields may likewise indicate pervasive biases in the model background state that influence more widely-used reanalysis products, such as temperatures and winds. Data assimilation helps to mitigate these effects in variables that are analyzed, but the extent of this mitigation depends on the availability and quality of assimilated observations (and thus varies with consequent variations in time and space), as well as the assimilation method used to combine observations with the model background state. No such mitigation can be expected for forecast-only variables that are not analyzed, such as the radiative heating rates often used to drive diabatic transport simulations in the upper troposphere and stratosphere (Wright and Fueglistaler, 2013; Tao et al., 2019). Data assimilation may even exacerbate disagreements among these variables if the analysis pulls the model away from its internal equilibrium state.

Cloud fields in reanalyses are essentially model products, but many variables that influence the distribution of clouds in the tropics are altered during the data assimilation step (e.g. atmospheric temperatures, moisture, and winds). We therefore anticipate that differences in cloud fields among reanalyses may arise from several factors, including the prescribed boundary conditions (such as SST), the physical parameterizations used in the atmospheric models (especially those pertaining to convection and large-scale condensation), the implementation of approach to data assimilation, and the assimilated data data assimilated (particularly satellite data from infrared and all-sky microwave humidity sounders). Traditional 3-dimensional variational (3D-Var) or 'first guess at appropriate time' (3D-FGAT) assimilation techniques provide only indirect constraints on cloud fields via the use of previous analyzed states to initialize subsequent forecasts. Constraints on cloud fields might be tightened by several approaches used in recent reanalyses, such as the incremental analysis update (IAU) and incremental 4-dimensional variational (4D-Var) methods. Under IAU, assimilation increments in analyzed fields are applied gradually during a 'corrector' forecast after they are calculated (Bloom, 1996; Takacs et al., 2018). Under incremental 4D-Var, the assimilation scheme iteratively adjusts the entire forecast to optimize the fit between the full temporal evolution of the model state and the available observations (Courtier et al., 1994). Both of these approaches produce cloud fields that are more consistent with analyzed temperatures, humidities, and winds, although this internal consistency is still governed by parameterized representations of sub-grid physics. Methods that directly make use of cloud and precipitation information in data assimilation, such as latent heat nudging or particle filters (e.g. Bannister et al., 2020), have yet to be implemented in global atmospheric reanalyses.

The purpose of this paper is to examine and evaluate upper tropospheric cloud fields in the tropics (30°S–30°N) as represented in recent atmospheric reanalyses, to identify differences among these reanalyses, and to explore the potential reasons behind these differences. We consider the fractional coverage of high clouds, total condensed water content in the tropical upper troposphere, and the radiative effects of clouds, both at the nominal top-of-atmosphere (TOA) and within the upper troposphere and lower stratosphere (UTLS). Our approach differs from and builds on other recent efforts in this direction (e.g. Dolinar et al., 2016) through an exclusive focus on tropical high clouds ($p < 500$ hPa), a deeper exploration of co-variability at daily time scales in addition to monthly means, discussion of cloud–radiation interactions in the tropical UTLS in addition to TOA fluxes, and the inclusion of some recently-released reanalyses. We also endeavor to systematically document key differences in parameterizations of clouds and radiation among the reanalyses, and discuss some of the ways these differences impact the state of the tropical atmosphere as represented in recent reanalyses.

We briefly introduce the reanalysis products, observationally-based data sets, and methodology in Sect. 2, with more . More detailed descriptions of the cloud and radiation parameterizations used in the reanalyses these reanalyses are collected in Appendix A. In Sect. 3, we summarize the climatological distributions of high cloud fraction, total condensed water content, and outgoing longwave radiation produced by reanalyses in the tropics. In Sect. 4, we examine how differences in the distribution and properties of high clouds alter radiative fluxes and exchange at daily scales in the deep tropics, both at the TOA and within the tropical UTLS. In Sect. 5, we explore the potential origins of differences in high clouds in the context of different reanalysis model treatments of deep convection and in situ cloud formation near the tropical tropopause. In Sect. 6, we briefly

Table 1. Summary of reanalysis products. HCC stands for high cloud fraction; CC for cloud fraction; CWC for cloud water content and I/LWC for separate ice and liquid water contents; TOA for top-of-atmosphere fluxes (shortwave and longwave; clear-sky and all-sky); and RHR for radiative heating rates (shortwave and longwave; all-sky). We use CFSR products for 1980–2010, CFSv2 for 2011–2014, and all other reanalysis products for 1980–2014.

Reanalysis	Model	Model Grid	HCC[a]	Profiles[a]	Fluxes[a]	Reference
ERA5	IFS 41R2 (2016)	N320 (∼31 km) 137 levels	$\sigma < 0.45$ 1-hourly	T, q, z, CC, I/LWC 3-hourly	TOA, RHR 12-h forecasts	Hersbach et al. (2020)
ERA-Interim	IFS 31R2 (2007)	N128 (∼79 km) 60 levels	$\sigma < 0.45$ 6-hourly	T, q, z, CC, I/LWC 6-hourly	TOA, RHR 12-h forecasts	Dee et al. (2011)
JRA-55	JMA GSM (2009)	N160 (∼55 km) 60 levels	$p < 500$ hPa 3-hourly	T, q, z, CC, I/LWC 6-hourly	TOA, RHR 6-h forecasts	Kobayashi et al. (2015)
MERRA-2	GEOS 5.12.4 (2015)	C180 (∼50 km) 72 levels	$p < 400$ hPa 1-hourly	T, q, z, CC, I/LWC 3-hourly	TOA, RHR 3-h forecasts	Gelaro et al. (2017)
CFSR	NCEP CFS (2007)	F288 (0.3125°) 64 levels	$p < 400$ hPa 6-hourly	T, q, z, CWC 6-hourly	TOA, RHR 6-h forecasts	Saha et al. (2010)
CFSv2	NCEP CFS (2011)	F440 (0.2045°) 64 levels	$p < 400$ hPa monthly	CWC monthly	TOA monthly	Saha et al. (2014)

[a] Climatological means of HCC, CC, CWC (or I/LWC), and TOA fluxes from all reanalyses are calculated from monthly mean products.

assess temporal variability and agreement amongst the reanalyses. We close the paper in Sect. 7 by summarizing the results and providing recommendations and context for reanalysis data users.

2 Data and methodology

2.1 Reanalysis products

Our intercomparison focuses mainly on five relatively recent atmospheric reanalyses: the fifth generation European Centre for Medium-range Weather Forecasts (ECMWF) reanalysis (ERA5; Hersbach et al., 2018)(ERA5; Hersbach et al., 2020), the ECMWF Interim Reanalysis (ERA-Interim; Dee et al., 2011), the Japanese 55-year Reanalysis (JRA-55; Kobayashi et al., 2015), the Modern-Era Retrospective Analysis for Research and Applications, Version 2 (MERRA-2; Gelaro et al., 2017), and the Climate Forecast System Reanalysis (CFSR; Saha et al., 2010) and its extension via the Climate Forecast System Version 2 (CFSv2; Saha et al., 2014). The earlier MERRA reanalysis (Rienecker et al., 2011) is included in selected comparisons. All six of these products are 'full-input' reanalyses in that they assimilate both conventional and satellite data (Fujiwara et al., 2017); however, they differ from each other with respect to their atmospheric models, assimilation techniques, and assimilated data sets. We document key Summary information on the forecast models and variables used are provided in Table 1. We document additional details of the cloud, convection, and radiation schemes in Appendix A. Readers interested in these technical details and how they imprint on the intercomparisons presented in this paper may wish to consult this appendix before proceeding to the results. Other relevant aspects of most of these reanalysis systems (with

With the exception of ERA5) , other relevant aspects have recently been reviewed by Fujiwara et al. (2017). An expanded review (including ERA5) is provided in Chapter 2 of the forthcoming SPARC Reanalysis Intercomparison Project (S-RIP) report (Wright et al., 2020, in preparation; digital version for review available at https://jonathonwright.github.io/S-RIPChapter2E.pdf) . (Wright et al., 2020, digital version available at https://jonathonwright.github.io/S-RIPChapter2E.pdf). Further details on assimilated observations and model treatments have been provided by Long et al. (2017) for temperature, Davis et al. (2017) for water vapour, and Tegtmeier et al. (2020) for the structure of the tropical tropopause layer (TTL), among others.

The full intercomparison period covers January 1980 through December 2014 and includes all six five reanalyses. We also conduct a more sophisticated detailed intercomparison of daily co-variability among key variables from five of the reanalyses (ERA5, ERA-Interim, JRA-55, MERRA-2, and CFSR), which covers co-variations among selected variables from January 2001–December 2010. Results for the full intercomparison are presented in Sects. 3, 4, and 6, while results based on daily co-variability are presented in Sects. 4 and 5. The Our intercomparison period includes the CFSR–CFSv2 transition in January 2011 , as well as and the intermediate year 2010 (as discussed by Fujiwara et al., 2017, among others). We show in Sect. 6 below that both transitions involved large changes in the cloud fields , that were much larger than the discontinuities at earlier other production stream transitions. The January 2011 transition to CFSv2 also involved changes in the atmospheric model formulation governing interactions between clouds and radiation. A brief summary of differences in tropical cloud and radiation fields between CFSR and CFSv2 is provided in Appendix B.

2.2 Observational data

Summary of observational data sets, listed in alphabetical order by project. TOA stands for top-of-atmosphere and UT for upper troposphere, where the latter comprises pressures less than 500 hPa for CERES SYN1Deg and pressures less than 440 hPa for ISCCP and MODIS. Other abbreviations are defined in the text.Project Product Version Variables Period Timestep Grid Levels Reference AIRS TqJoint v6 T, q, z 2003–2010 daily 1° 12 (p) Texeira (2013) CERES EBAF Ed4A TOA radiation 2001–2014 monthly 1° TOA Doelling (2019)CERES SYN1Deg Ed4A TOA radiation 2001–2010 daily 1° TOA Doelling (2017)CERES SYN1Deg Ed4A high cld cover 2001–2010 daily 1° UT Doelling (2017)CFMIP2 GOCCP v3.1.2 cld frac profile 2007–2014 monthly 2° 40 (z) Chepfer et al. (2010)CloudSat derived v1 cld frac profile 2007–2010 monthly 2° 40 (z) Kay and Gettelman (2009) CloudSat CWC-RO v5.1r4 IWC profile Aug 2006– monthly 1° 40 (z) Austin et al. (2009)Jul 2007 ISCCP HGM v1 high cld cover 1984–2014 monthly 1° UT Rossow et al. (2017)Terra MODIS MOD08 c6 high cld cover 2001–2014 monthly 1° UT Platnick (2015) NASA-GEWEX SRB r3.1 TOA radiation 1984–2007 monthly 1° TOA Zhang et al. (2015)

We use several observationally-based data products to supply context, including TOA radiative fluxes, cloud fraction, cloud ice water content, and atmospheric thermodynamic state variables (Table 2). Observations of these variables are subject to a number of uncertainties, including lack of sensitivity to optically thin clouds or clouds composed of small particles (e.g. Dessler and Yang, 2003), uncertainties caused by overlapping cloud layers (e.g. Zhang et al., 2005), errors in cloud top height (e.g. Sherwood et al., 2004), and diurnal or spatial sampling biases (e.g. Fowler et al., 2000; Hearty et al., 2014). As our primary focus is on the intercomparison of reanalysis products, we have opted not to apply not applied a satellite cloud observation simulator (e.g. Bodas-Salcedo et al., 2015; Stengel et al., 2018) to the reanalysis outputs. Accordingly, we stress that the most

Table 2. Summary of observational data sets, listed in alphabetical order by project. TOA stands for top-of-atmosphere and UT for upper troposphere, where the latter comprises pressures less than 500 hPa for CERES SYN1Deg and pressures less than 440 hPa for ISCCP and MODIS. Other abbreviations are defined in the text.

Project	Product	Version	Variables	Period	Timestep	Grid	Levels	Reference
AIRS	TqJoint	v6	T, q, z	2003–2010	daily	1°	12 (p)	Texeira (2013)
CERES	EBAF	Ed4.1	TOA radiation	2001–2014	monthly	1°	TOA	Doelling (2019)
CERES	SYN1Deg	Ed4A	TOA radiation	2001–2010	daily	1°	TOA	Doelling (2017)
CERES	SYN1Deg	Ed4A	HCC	2001–2010	daily	1°	UT	Doelling (2017)
CFMIP2	GOCCP	v3.1.2	CC profile	2007–2014	monthly	2°	40 (z)	Chepfer et al. (2010)
CloudSat	KG2009	v1	CC profile	2007–2010	monthly	2°	40 (z)	Kay and Gettelman (2009)
CloudSat	2C-ICE	P1_R05	IWC profile	2007–2010	monthly	n/a	104 (z)	Deng et al. (2015)
ISCCP	HGM	v1	HCC	1984–2014	monthly	1°	UT	Rossow et al. (2017)
Terra MODIS	MOD08	c6	HCC	2001–2014	monthly	1°	UT	Platnick (2015)
NASA-GEWEX	SRB	r3.1	TOA radiation	1984–2007	monthly	1°	TOA	Zhang et al. (2015)

Use of a satellite simulator could address sensitivity and sampling biases for easier comparison with observations; however, it could also obscure inter-reanalysis differences in cloud types that are not well observed and complicate analysis of cloud radiative effects in each reanalysis. Accordingly, comparisons between reanalysis products and ~~observational data presented~~ satellite cloud observations in this paper ~~are qualitative rather than quantitative~~should be interpreted with care.

The International Satellite Cloud Climatology Project (ISCCP) has produced observationally-based descriptions of clouds and their attributes using geostationary and polar-orbiting satellite measurements (Rossow and Schiffer, 1991). We use the H-series Global Monthly (HGM) product for January 1984–December 2014 (Rossow and Schiffer, 1999; Rossow et al., 2017). As a supplement to the ISCCP cloud data, we use all-sky and clear-sky fluxes of longwave (LW) radiation at the TOA from the NASA Global Energy and Water Cycle Experiment (GEWEX) Surface Radiation Budget (SRB) project covering January 1984 through December 2007 (Stackhouse et al., 2011; Zhang et al., 2015). These data are based on radiative calculations that combine observed fluxes and ozone with Goddard Earth Observing System Data Assimilation System, Version 4 (GEOS-4) analyses of temperature and water vapour. Pixel-level data from ISCCP are used to estimate cloud radiative effects in SRB.

We use several products from the Clouds and the Earth's Radiant Energy System (CERES) experiment (Wielicki et al., 1996). First, we use time-mean TOA fluxes calculated from Energy Balanced and Filled (EBAF) monthly-mean products at 1°×1° spatial resolution (Doelling, 2019). We use CERES EBAF Edition 4.1, which provides clear-sky TOA fluxes that are specifically intended for comparison with model outputs (Loeb et al., 2020). Second, we use daily-mean Synoptic Radiative Fluxes and Clouds (SYN1Deg) products at 1°×1° spatial resolution (Doelling, 2017). The SYN1Deg data set represents an intermediate step in the production of the monthly EBAF dataset. SYN1Deg provides several estimates of TOA radiative fluxes, including direct measurements, outputs from initial 'untuned' radiative transfer model simulations, and outputs from a second set of radiative transfer simulations in which the model input variables are adjusted to bring the simulated fluxes into better agreement with the observed fluxes. The initial atmospheric state for radiative computations is taken from the GEOS-5 data assimilation system, a different version of ~~which is~~ that used for MERRA-2. Only the final adjusted fluxes are discussed, as these products are most appropriate for computing cloud radiative effects for comparison with reanalysis estimates. The results are qualitatively similar when the direct measurements are used instead. Along with TOA radiative fluxes, the SYN1Deg data set includes estimates of cloud fraction retrieved using measurements collected by the Moderate-Resolution Imaging Spectroradiometer (MODIS) and geostationary satellites (Minnis et al., 2011; Doelling et al., 2013). We also use high cloud ~~fractions~~ fraction (HCC) data from Collection 6 of the Terra MODIS Level 3 Atmosphere Product (MOD08; Platnick, 2015).

For observations of the thermodynamic state of the atmosphere, we use level 3 data from the Atmospheric Infrared Sounder (AIRS) version 6 'TqJoint' collection (Texeira, 2013). This data set provides gridded representations of temperature, moisture, and other fields based on a consistent set of initial retrievals in each grid cell (Tian et al., 2013). As the finest temporal resolutions of other data examined in this study are daily means, we average data from ascending and descending passes together. Variables taken from AIRS TqJoint include temperature, water ~~vapor~~ vapour mass mixing ratio, and geopotential height between January 2003 and December 2014.

Finally, we examine three products ~~deriving~~ derived from CloudSat and Cloud-Aerosol Lidar and Infrared Pathfinder Satellite Observation (CALIPSO) measurements. These include two monthly estimates of cloud fraction vertical profiles, one based on combined information from CloudSat and CALIPSO (Kay and Gettelman, 2009) and one based on CALIPSO alone (Chepfer et al., 2010). We use the combined CloudSat–CALIPSO product for the four years 2007–2010 and the GCM-Oriented CALIPSO Cloud Product (GOCCP) for the eight years 2007–2014. The first product was discontinued after CloudSat switched to sunlit-only observations in early 2011. We also use ice water content (IWC) measurements from CloudSat ~~based on version 5.1 (release 4) of the radar-only~~ and CALIPSO based on the 2C-ICE retrieval algorithm ~~(CWC-RO; Austin et al., 2009), mapped onto a 1°×1° grid and averaged over the 12 months from August 2006 through July 2007 (see also Zhao et al., 2017). CloudSat measurements in units of mg m^{-3} are converted to mass mixing ratios using dry-air densities estimated from a tropical-mean temperature profile computed using AIRS observations from the same period.~~ (R05; Deng et al., 2015), averaged for all tropical profiles (10°S–10°N) over 2007–2010. CloudSat- and CALIPSO-based data sets are provided on ~~a 40-level height grid~~height grids, which we convert to pressure using the barometric equation with a constant scale height of 7.46 km. This approach introduces uncertainty in the precise vertical location (in pressure coordinates) of features observed by CloudSat and CALIPSO, which should be taken into consideration when comparing these features to those produced by the reanalyses.

2.3 Derived variables and statistical treatments

~~We use several classes of variables in this intercomparison.~~ Variables directly related to tropical high clouds include ~~high cloud fraction~~ HCC and vertical profiles of cloud fraction and cloud water content, while variables used to explore the impacts of differences in high clouds include TOA radiative fluxes and vertically-resolved radiative heating rates within the upper troposphere, tropopause layer, and lower stratosphere. All vertically-resolved variables are evaluated on pressure levels, interpolated from height or model levels when necessary.

Cloud radiative effects (CREs) are computed as clear-sky minus all-sky fluxes using positive-upward fluxes at the TOA, so that LW effects are the LWCEW is generally positive (the presence of clouds reduces OLR) and SW effects are the SWCRE is generally negative (the presence of clouds increases the planetary albedo). We denote the LW cloud radiative effect as LWCRE and the SW effect as SWCRECREs are sensitive to differences in both all-sky and clear-sky fluxes (e.g. Soden et al., 2004); accordingly, we report differences in both all-sky and clear-sky TOA fluxes below.

Variables used to diagnose the potential origins of differences in high clouds include SST, vertical velocity at 500 hPa, and vertical profiles of temperature, specific humidity, and geopotential height between 1000 and 100 hPa. The latter three variables are used to compute moist static energy:

$$\mathrm{MSE} = gz + c_p T + L_v q, \tag{1}$$

where g is gravitational acceleration in Earth's lower atmosphere, z is geopotential height, c_p is the specific heat constant capacity for dry air, T is temperature, L_v is latent enthalpy of vaporization vapourization at 0°C, and q is specific humidity. Temperature and specific humidity are also used to calculate equivalent potential temperature (θ_e), which is then used to diagnose the potential instability of the lower troposphere as the difference in equivalent potential temperature between the lower troposphere (850 hPa) and the middle troposphere (500 hPa):

$$\mathrm{PI} = \theta_{e,850} - \theta_{e,500}. \tag{2}$$

Equivalent potential temperature is computed according to the formula proposed by Bolton (1980) using the MetPy software package (May et al., 2008 - 2020). Relative humidity (RH) is calculated with respect to liquid water using MetPy. This approach avoids inconsistencies in the implementation of the liquid–ice transition among the different datasets (see Appendix A1). Ratios between saturation vapor vapour pressures with respect to ice and with respect to liquid water are provided for context, calculated using the empirical formulas proposed suggested by Emanuel (1994).

The level of zero radiative heating (LZRH) is determined for all profiles for which the daily-mean net radiative heating rate is positive at 100 hPa. Radiative heating rates All-sky total radiative heating rates (LW+SW) are linearly interpolated onto a 1000-level grid between 100 hPa and 500 hPa with equal spacing in $\ln(p)$. The LZRH is then defined as the largest pressure for which all net radiative heating rates are positive between 100 hPa and that level (inclusive).

Statistical treatments mainly consist of composite averages or distributions conditioned on ranked quartiles of the LWCRE (i.e. four bins separated by the 25$^{\mathrm{th}}$ percentile, the median, and the 75$^{\mathrm{th}}$ percentile). We focus in particular on the largest values of LWCRE (denoted as Q4) in the inner tropics (10°S–10°N) as a proxy for strong convective activity. Results are very similar for ranked quartiles of all-sky OLR, with OLR reversed so that Q4 corresponds to the smallest values of OLR. Using HCC instead of LWCRE produces more substantial differences, particularly for MERRA-2. Given discrepancies in the precise definition of HCC across reanalyses (Table 1) and the difficulty of defining an appropriate observational benchmark for HCC, we judge HCC less suitable for this purpose. We select LWCRE rather than OLR for convenience of presentation. Averages taken in the horizontal dimension are weighted by relative area. Two-dimensional kernel density estimates are computed using the k-dimensional tree-based implementation in SciKit-Learn (Pedregosa et al., 2011) with a Gaussian kernel. Optimal bandwidths for kernel density estimates are identified using a 20-fold grid-search cross-validation on randomly selected subsets of the data, and consistently converge to values near 1 (0.8–1.3) for the LWCRE and values near 2 (1.5–2.4) for the SWCRE.

3 Climatological distributions

~~We define a multi-reanalysis mean (MRM) to facilitate our intercomparison of cloud and radiation climatologies produced by the reanalyses climatological condition, calculated by averaging products from the ERA-Interim, JRA-55, MERRA-2, and CFSR/CFSv2 reanalyses. ERA5 and MERRA are omitted from the MRM, ERA5 because it was made available relatively late in the S-RIP activity and MERRA because we do not include MERRA products beyond this section of the paper.~~ Figure 1 shows the time-mean distributions of high cloud ~~cover~~ fraction (HCC) in the tropics based on ~~this MRM (1980–2014) and~~ the ISCCP HGM observationally-based analysis ~~(~~and the five individual reanalyses for 1984–2014~~). Differences of the six individual reanalyses relative to the MRM are also shown~~. Area-weighted mean values of ~~high cloud fraction~~ HCC averaged over the tropics (30°S–30°N) are noted for each product. The definition of ~~high cloud fraction~~ HCC varies somewhat among these data sets~~. For example, high clouds are defined at pressures less than ∼~~, with the lower bound of the high cloud layer ranging from 500 hPa ~~for JRA-55, pressures less than ∼~~to 400 hPa ~~for CFSR/CFSv2, MERRA, and MERRA-2, and pressures less than ∼450 hPa for ERA-Interim and ERA5. For the observational data sets, high cloud fractions are based on clouds with tops diagnosed at pressures less than 440 hPa in ISCCP and MODIS, and at pressures less than 500 hPa in CERES SYN1Deg.~~ (Tables 1 and 2). We show below (Fig. 3) that reanalysis-derived cloud fraction profiles have minima between 400 and 500 hPa in the tropics, so that differences in the precise definition of ~~high cloud fraction~~ HCC should not greatly impact qualitative comparisons based on Fig. 1.

~~High cloud fractions~~ Tropical mean HCCs among the reanalyses are smallest in JRA-55 ~~are almost exclusively smaller than the MRM, while those~~ and largest in MERRA-2~~are larger than the MRM. Negative biases in~~. For JRA-55~~are largest~~, differences relative to the other reanalyses are most pronounced over canonical deep convective regions, ~~such as the equatorial~~ including the tropical eastern Indian Ocean, equatorial Africa, and the Maritime Continent. By contrast, positive biases in MERRA-2 are largest ~~along~~ around the flanks of the deep convective regions. Tropical mean values of ~~high cloud fraction in~~ HCC are similar between ERA-Interim and CFSR/CFSv2~~are close to the MRM; however,~~, but with substantial differences in the spatial patterns of ~~biases relative to the MRM are qualitatively opposite~~ HCC between these two reanalyses. ~~Whereas~~ Most notably, ERA-Interim produces ~~high cloud fractions larger than the MRM~~ larger HCCs than CFSR/CFSv2 in the deep convective regions of the tropics (~~e.g. over the Maritime Continent and equatorial Indo–Pacific domain), CFSR/CFSv2 produces high cloud fractions smaller than the MRM in deep convective regions (especially over the western Pacific). ERA-Interim typically underestimates the MRM outside of the canonical deep convective regions, while CFSR/CFSv2 produces larger high cloud fractions over mountainous regions, such as the Andes and the Tibetan Plateau. Differences between~~ especially in the Indo-Pacific region). The spatial pattern in ERA5 ~~and the MRM are~~ is similar in many ways to ~~those found for~~ that in ERA-Interim, but with further ~~enhancements in~~ increases in HCC over tropical convective regions (especially over land). ERA5 has ~~noticeably larger high cloud fractions~~ larger HCCs than ERA-Interim in tropical South America and Africa, as well as in the

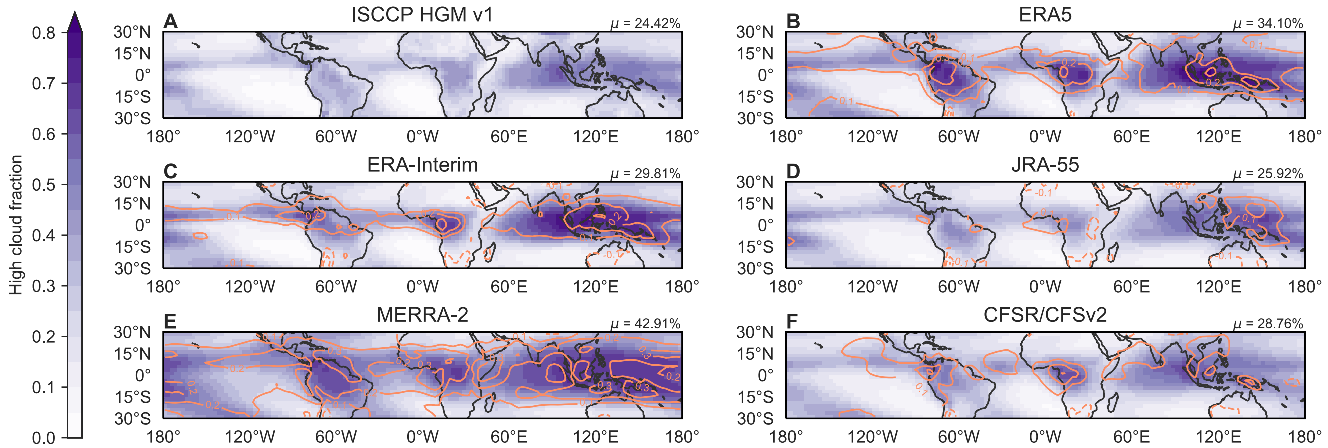

Figure 1. Climatological mean spatial ~~distributions~~ distribution of high cloud cover (HCC) for (A) ~~the multi-reanalysis mean (MRM) over 1980–2014~~ISCCP HGM, ~~calculated by averaging the distributions for ERA-Interim, JRA-55, MERRA-2, and CFSR, and~~ (B) ~~ISCCP over 1984–2014. Differences relative to the MRM are shown for~~ ERA5, (C) ~~ERA5~~ERA-Interim, (D) ~~ERA-Interim~~JRA-55, (E) ~~JRA-55~~MERRA-2, and (F) CFSR/CFSv2 ~~,~~ over 1984–2014. Differences relative to ISCCP HGM are shown for each reanalysis as orange contours (~~G~~dashed for negative values) ~~MERRA-2, and (H) MERRA over 1980–2014~~at intervals of 0.1. The area-weighted tropical mean (30~~°S–30°N~~°S–30°N) ~~high cloud fraction~~ HCC based on each product is shown at the upper right corner of the corresponding panel.

South Asian monsoon region, the Pacific portion of the ITCZ, and the SPCZ. These differences contribute to an increase of 0.04 (~~4~~∼14%) in the tropical mean ~~high cloud fraction~~ HCC between ERA-Interim and ERA5. ~~Additional analysis is necessary to assess which of these is more consistent with the actual distribution of high clouds. However,~~ Bechtold et al. (2014) reported that ~~modifications~~ changes to parameterized convection in the ECMWF atmospheric model implemented between ERA-Interim and ERA5 yielded lower biases against observed brightness temperatures in land convective regions, especially for channels sensitive to the upper troposphere. However, as differences in cloud top temperatures between the two model versions could also influence the simulated brightness temperatures, these lower biases cannot be directly attributed to improvements in HCC.

Initial comparison with ~~high cloud fractions from ISCCP D2~~ ISCCP HGM suggests that the reanalyses systematically overestimate ~~high cloud cover~~HCC, with the tropical mean ~~estimate~~ from JRA-55 (25.74%) falling closest to that ~~based on ISCCP D2 (23.93~~from ISCCP (24.42%). However, as discussed at the beginning of section 2, direct comparisons between cloud variables derived from satellite observations and those derived from models ~~may~~ can be misleading. MERRA-2 provides outputs from the Cloud Feedback Model Intercomparison Project (CFMIP) Observation Simulator Package (COSP; Bodas-Salcedo et al., 2015) as an ancillary product in the reanalysis. Included in this product are estimates emulating ~~high cloud fraction~~ HCC as observed by MODIS. Whereas MERRA-2 produces a tropical mean ~~high cloud fraction of 42.98% (rising slightly to~~ HCC of 43.35% during 2001–2014~~)~~, the MERRA-2 COSP product indicates that MODIS would observe a tropical mean ~~high cloud fraction~~ HCC of only 24.71%. This latter estimate is in good agreement ~~with both the~~ not only with ISCCP HGM, but also

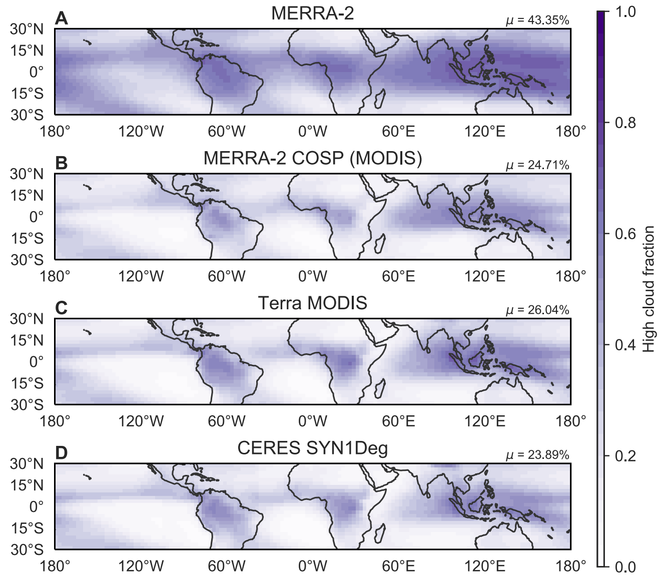

Figure 2. As in Fig. 1~~a~~A, but for (A) direct output from MERRA-2, (B) MERRA-2-COSP (emulating MODIS observations of the MERRA-2 atmosphere), (C) Terra MODIS, and (D) CERES SYN1Deg (based primarily on Terra and Aqua MODIS) for 2001–2014. The area-weighted tropical mean (30°S–30°N) high cloud ~~fraction~~ cover based on each product is shown at the upper right corner of the corresponding panel.

with Terra MODIS (26.04%) and CERES SYN1Deg (23.89%) gridded products ~~over the same period, both in terms of the tropical mean value and~~ (Fig. 2), and extends to the spatial distribution of ~~high cloud cover (Fig. 2). The most pronounced~~ HCC. The largest difference between the standard MERRA-2 HCC product and the MERRA-2 COSP product is a reduction in ~~cloud fractions~~ HCC outside the canonical deep convective regions of the tropics~~, suggesting~~. This difference suggests that the large ~~high cloud fractions~~ HCCs produced by MERRA-2 in these ~~locations~~ areas are associated with optically thin clouds having small water paths, which cannot be readily observed by MODIS. The close agreement between MERRA-2 COSP and ~~corresponding~~ observational estimates does not necessarily mean that the larger ~~high cloud fractions~~ HCCs in MERRA-2 are more realistic (i.e. that the other reanalyses substantially underestimate ~~high cloud fraction~~ HCC in the tropics). Rather, it indicates only that MERRA-2 produces a reasonably realistic distribution of the high clouds that can be readily observed by passive infrared instruments like MODIS. ~~Affirming this point, a~~ A recent study in which a cloud simulator was applied to ERA-Interim outputs also indicates good agreement with observed ~~high cloud fractions~~ HCCs in the tropics, with a slight ~~high bias (≤ 10%) in the same~~ positive bias in the inner tropical regions~~where ERA-Interim overestimates the MRM~~ (Stengel et al., 2018).

Figure 3 shows time-mean zonal-mean ~~distributions~~ profiles of cloud fraction in the tropical upper troposphere as functions of latitude and pressure. ERA5, ERA-Interim, JRA-55, and MERRA-2 all show maxima in cloud fraction near the base of the tropical tropopause layer. The peak value in ERA-Interim is centered at 150 hPa, slightly above that in ERA5 (∼175 hPa) and MERRA-2 (∼200 hPa) and slightly below that in JRA-55 (∼125 hPa). JRA-55 also shows a secondary maximum near 200 hPa.

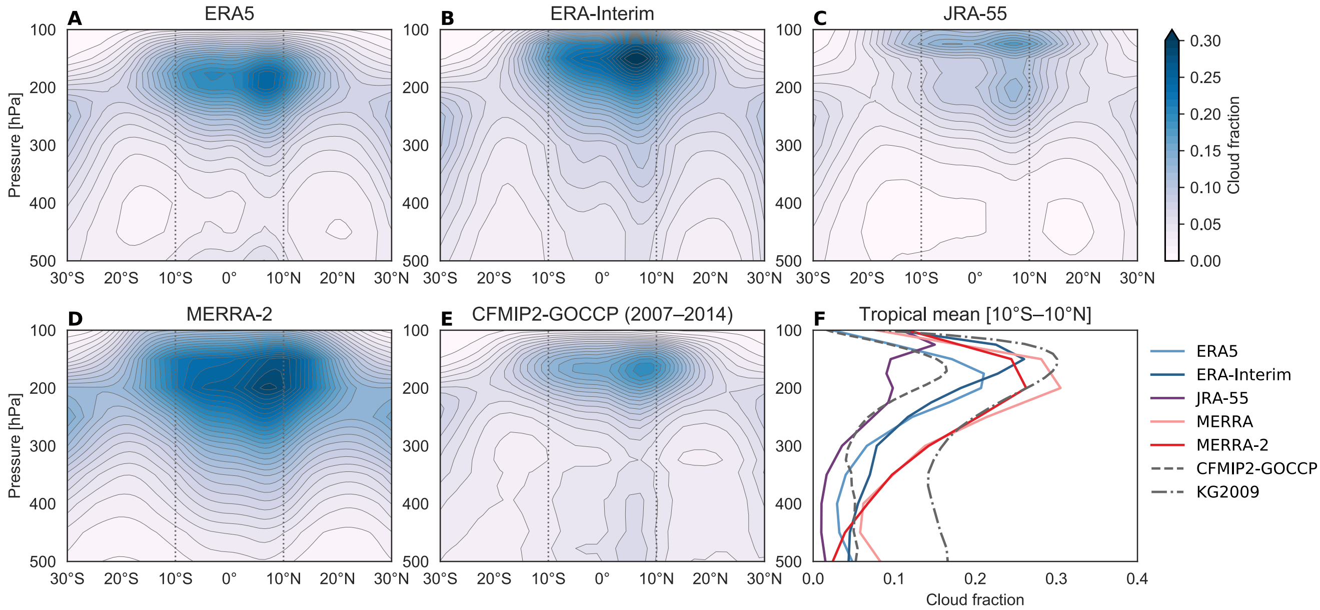

Figure 3. Time-mean zonal-mean distributions of cloud fraction based on the (A) ERA5, (B) ERA-Interim, (C) JRA-55, and (D) MERRA-2 reanalyses (1980–2014), along with (E) an observationally-based distribution from the GOCCP CALIPSO-based product produced for CFMIP2 (Chepfer et al., 2010), which covers 2007–2014. Inner tropical mean (10°S–10°N) profiles of cloud fraction based on these five estimates are shown in (F), along with profiles from MERRA and the combined CloudSat–CALIPSO product derived by Kay and Gettelman (2009). The latter is averaged over 2007–2011. Vertical lines in (A) through (E) mark the bounds of the averaging domain. CFSR does not provide vertical profiles of cloud fraction.

All of these maxima are most pronounced in the Northern Hemisphere between 5°N and 10°N, reflecting the preferred position of the intertropical convergence zone (ITCZ). CFSR does not provide vertical profiles of cloud fraction and is therefore not represented in Fig. 3.

Observationally-based estimates of vertically-resolved cloud fraction from CALIPSO (CFMIP2-GOCCP; Chepfer et al., 2010) are shown in Fig. 3E and Fig. 3F, with a tropical mean profile based on CloudSat and CALIPSO (KG2009; Kay and Gettelman, 2009) also included in Fig. 3F. The zonal-mean distribution based on KG2009 is qualitatively similar to that based on CFMIP2-GOCCP and is therefore omitted from Fig. 3; however, these two datasets show large differences in the magnitude of cloud fraction within the tropical upper troposphere (Fig. 3F). The range of cloud fractions spanned by the two observationally-based estimates is comparable to that spanned by the reanalysis products. Like the reanalyses, the observational products indicate that the maximum cloud fraction is located in the Northern Hemisphere tropics. The vertical placement of this maximum is around 150–175 hPa, between that produced by ERA-Interim and that produced by ERA5. This ~~implies~~ indicates that the altitude of the maximum in MERRA-2 is slightly too low, ~~although the relatively coarse vertical resolution of the MERRA-2 pressure-level product in this region and uncertainties associated with height–pressure conversion for the~~

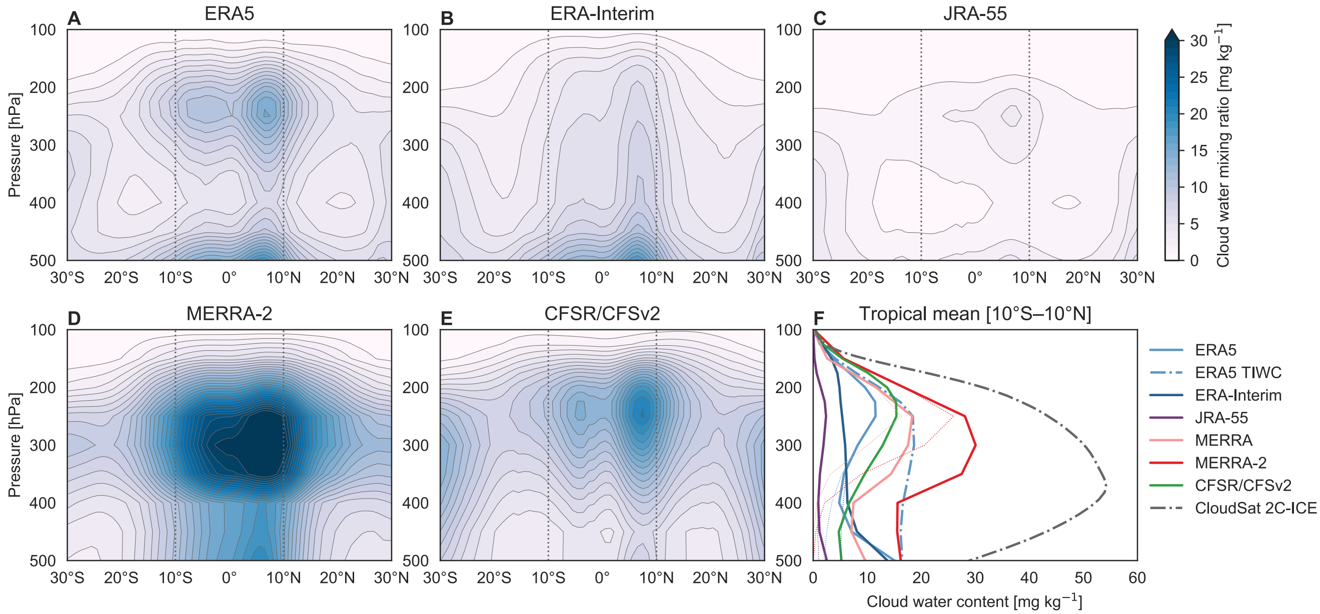

Figure 4. Time-mean zonal-mean distributions of total cloud water content based on the (A) ERA5, (B) ERA-Interim, (C) JRA-55, (D) MERRA-2, and (E) CFSR/CFSv2 reanalyses (1980–2014). Inner tropical mean (10°S–10°N) profiles based on these five reanalyses are shown in panel (F), along with profiles from MERRA and an observationally-based estimate of total ice water content (cloud ice + snow) during ~~August 2006–July 2007~~ 2007–2010 from ~~CloudSat~~the CloudSat–CALIPSO 2C-ICE product. Vertical lines in panels (A) through (E) mark the bounds of the averaging domain. Dashed lines in (F) indicate ice-only water contents from the reanalyses that provide this information (all but CFSR/CFSv2). The total ice (cloud ice + snow) profile from ERA5 is also included for comparison with 2C-ICE.

~~observational estimates (see Sect. 2.2) reduce our confidence in this conclusion. We find firmer ground in interpreting some of the other differences in Fig. 3. First, the~~ a known issue in the GEOS-5 model. The bimodal structure of the cloud fraction profile and the extremely high altitude of the peak values (125 hPa) are unique to JRA-55. Together with the relatively small values of ~~high cloud cover~~ HCC in JRA-55 (Fig. 1E), we conclude that this reanalysis underestimates high cloud ~~fraction~~ fractions through most of the tropical upper troposphere. ~~Second, the observational estimates indicate~~ The observational estimates also include secondary maxima in cloud fraction between 400–500 hPa, while most of the reanalyses produce local minima in this region. This difference suggests that the reanalysis models may systematically underestimate the depth, frequency, or amount of cloud detrained by cumulus congestus in the tropics (Johnson et al., 1999).

Differences among the reanalyses are even more pronounced with respect to time-mean zonal-mean distributions of cloud water content (CWC) in the tropical upper troposphere (Fig. 4). Here CWC represents the sum of ice and liquid water content, except for the CloudSat estimate shown in Fig. 4F, which ~~is based on icewater content (IWC) alone (see also Zhao et al., 2017)~~ includes only ice. Among the reanalyses, MERRA-2 (Fig. 4D) produces the largest CWCs in this region, with a pronounced peak at 300 hPa. Although MERRA-2 produces smaller cloud fractions in the tropical upper troposphere than its predecessor MERRA (Fig. 3F), it produces substantially larger CWCs (Fig. 4F). The assumed effective radius for ice particles was reduced between MERRA and MERRA-2, along with several other changes that collectively increased the average residence time of ice clouds aimed at increasing upper tropospheric humidity in the model (Molod et al., 2012, 2015). The large CWCs in MERRA-2 have significant impacts on radiative transfer , as discussed in (see Sect. 4below). CFSR/CFSv2 (Fig. 4E) produces a similarly pronounced vertical maximum in CWC, but shifted slightly higher in altitude and with a peak magnitude (15.4 mg kg^{-1} at 250 hPa) roughly half that produced by MERRA-2 (30.1 mg kg^{-1} at 300 hPa) when averaged over the inner tropics (10°S–10°N). JRA-55 (Fig. 4C) shows a qualitatively similar distribution to those of MERRA-2 and CFSR/CFSv2, but with much smaller magnitudes (maximum value: 2.4 mg kg^{-1} at 250 hPa). This difference is again consistent with JRA-55 underestimating cloud cover in the tropical upper troposphere. The zonal-mean distribution of CWC in ERA-Interim (Fig. 4B) is remarkably different from that in the other reanalyses, including ERA5 (Fig. 4A), with no distinct maximum in the tropical upper troposphere. Instead, ERA-Interim shows a monotonic decrease in CWC with increasing altitude above 500 hPa. Although it is difficult to pinpoint the reason for the difference in vertical profiles of CWC between ERA-Interim and ERA5, changes to the treatment of entrainment and detrainment in the convective scheme (Appendix A2) likely play a key rolemay contribute. These changes, together with improvements in prognostic microphysics, alter the structure of the convective mass flux and improve the coupling between convection and the tropical environment (Bechtold et al., 2008, 2014).

The tropical-mean profile of IWC based on CloudSat radar-only retrievals between August 2006 and July 2007 the CloudSat 2C-ICE product between 2007–2010 is shown for context in Fig. 4F. The diurnal sampling of CloudSat along its initial orbit in the A-Train constellation (equator crossing times around 01:30 and 13:30 local solar time) should be taken into account when comparing the profile observed by CloudSat to those produced by CloudSat profile to the reanalyses, as this orbit misses the late afternoon peak of continental convective activity in the tropics (e.g. Yang and Slingo, 2001). It is also important to note that the CloudSat estimate represents total IWC, including both precipitating and cloud ice. We may therefore expect the profile maximum to be both larger in magnitude and lower in altitude than one based on cloud ice alone (Li et al., 2012, 2016). This expectation is supported by Fig. 4F, as the peak value of IWC based on CloudSat is larger and lower in altitude relative to the reanalysis profiles (42.954.2 mg kg^{-1} at 300∼370 hPa). Despite this difference, the structure of the CloudSat profile is qualitatively more consistent with the pronounced anvil layers in ERA5, MERRA-2, and CFSR/CFSv2 than with JRA-55 or ERA-Interim.

The cumulus congestus peak in the middle troposphere that does not appear in reanalysis estimates of cloud fraction (but does appear in observations) is evident in the reanalysis estimates of CWC but not in the CloudSat estimate. The latter may be attributable to the exclusion of liquid water from the CloudSat estimate, although previous analyses of CloudSat CWCs did not show a clear maximum here even when the liquid phase was included (see, e.g. Su et al., 2011). By contrast, MERRA-2, ERA-Interim, ERA5, and JRA-55 all indicate large liquid water fractions in clouds at these altitudes. In ERA-Interim, 12.5% of cloud water at 400 hPa averaged over the inner tropics is liquid, rising to 63.3% at 500 hPa. These ratios are larger in ERA5 (28.6% and 86.0%, respectively) and MERRA-2 (86.4% and 99.8%), and smaller in JRA-55 (3.3% and 60.4%). CFSR does not provide separate outputs for liquid and ice water contents. The prevalence of liquid water content at these altitudes in MERRA and MERRA-2 relative to CloudSat is a known feature of the GEOS-5 data assimilation system (Su et al., 2011).

4 Radiative impacts

4.1 Top-of-atmosphere radiation budget

Figure 5 shows spatial distributions of ~~OLR and the LWCRE based on the MRM~~all-sky and clear-sky OLR based on CERES EBAF during 2001–2014, along with ~~observationally-based estimates of these quantities based on CERES EBAF and differences between six~~ differences between the five individual reanalysis products and ~~the MRM. The MRM suggests a time-mean tropical-mean OLR of 265.8~~CERES. Rather than direct observations (with clear-sky fluxes taken only from cloud-free columns), the CERES EBAF fluxes discussed in this section are estimates for the entire column with clouds removed, and are suitable for direct comparison with model-generated clear-sky fluxes (Loeb et al., 2020). CERES EBAF estimates a time mean tropical mean OLR of 260.3 $\mathrm{W\,m^{-2}}$ over ~~1980–2014, much larger than the CERES EBAF estimate of 260.4~~2001–2014, smaller than in any of the reanalyses except for MERRA-2.Better agreement is found for clear-sky OLR, with tropical-mean values from all reanalyses within ±2.5 $\mathrm{W\,m^{-2}}$ ~~over 2001–2014.~~ of the CERES EBAF estimate. Accordingly, the ~~time-mean tropical-mean~~ time mean tropical mean LWCRE based on ~~the MRM was 21.1~~CERES EBAF (27.3 $\mathrm{W\,m^{-2}}$~~over 1980–2014, much less than the 30.2~~) was larger than that produced by any of the reanalyses except for MERRA-2 (31.6 $\mathrm{W\,m^{-2}}$~~value indicated by CERES EBAF. Isolines of LWCRE closely match those of OLR~~). ERA-Interim, ~~confirming that the radiative effects of clouds dominate spatial variability in OLR within these datasets. Although differences between the MRM and the observational estimates shown in Fig. 5 may reflect differences in averaging period,~~ ERA5, and CFSR/CFSv2 underestimate clear-sky OLR even as they overestimate all-sky OLR, so that negative biases in the tropical-mean LWCRE are approximately twice as large as positive biases in tropical-mean OLR in each of these three reanalyses. Comparison with observationally-based estimates with longer durations ~~are either consistent with CERES EBAF (e. g.~~ further indicates that most of the reanalyses overestimate OLR and underestimate the LWCRE in the tropics. NASA GEWEX SRB indicates tropical-mean values of 259.4 $\mathrm{W\,m^{-2}}$ for all-sky OLR and 27.7 $\mathrm{W\,m^{-2}}$ for LWCRE ~~based on NASA GEWEX SRB during~~ over 1984–2007~~) or suggest even smaller values for the tropical-mean OLR (e.g.~~, while the NOAA Interpolated OLR product indicates a tropical-mean value of 250.7 $\mathrm{W\,m^{-2}}$ ~~based on NOAA Interpolated OLR during~~ for all-sky OLR over 1980–2014~~). Rather than direct observations (with clear-sky fluxes taken only from cloud-free columns), the CERES and SRB fluxes discussed in this section are adjusted fluxes that use both direct observations and RTM calculations as constraints on the final product (Sect. 2.2).~~.

~~The expected impacts of high clouds on OLR in the reanalyses are evident when panels C–H of Fig. 5 are compared to the corresponding panels of Fig. 1. For example, both ERA-Interim and CFSR/CFSv2 produce tropical mean values of OLR and LWCRE that are close to the corresponding MRM values, just as both ERA-Interim and CFSR/CFSv2 produce tropical mean high cloud fractions that are close to the MRM value. However, taking the deep convective portions of the Indo–Pacific domain as an example, ERA-Interim tends to underestimate OLR and overestimate LWCRE relative to the MRM, consistent with larger high cloud fractions in this region, while CFSR/CFSv2 tends to overestimate OLR and underestimate LWCRE, consistent with smaller high cloud fractions. ERA5 produces a slightly smaller tropical-mean OLR and slightly larger LWCRE than ERA-Interim, consistent with its larger tropical-mean high cloud fraction. The changes are again most pronounced over tropical land areas with strong convection, especially South America, Africa, and the South Asian monsoon region.~~ Many

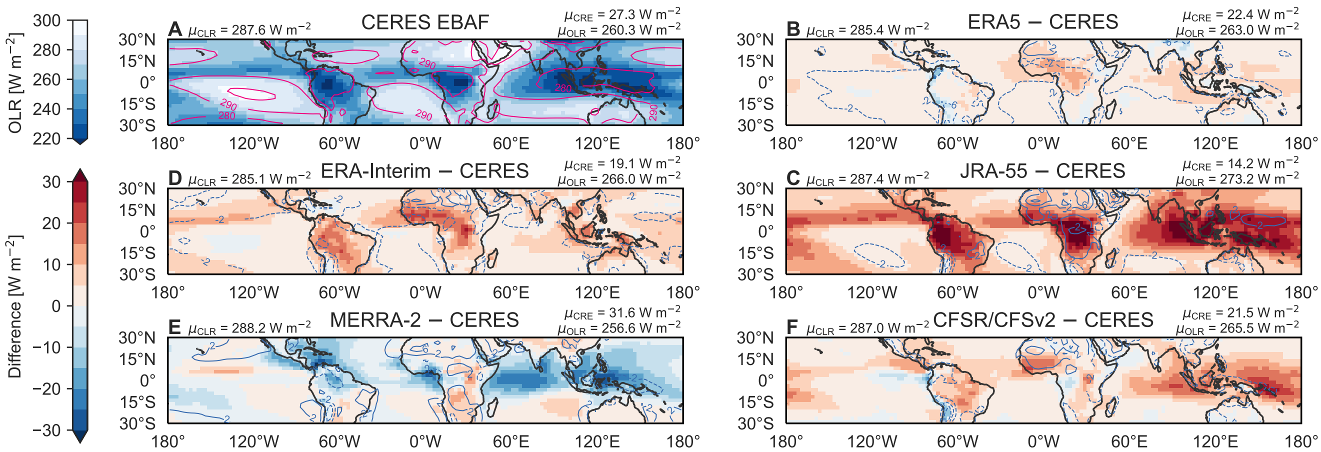

Figure 5. Climatological mean spatial distributions of all-sky outgoing longwave radiation (OLR; shading) and clear-sky outgoing longwave cloud radiative effect radiation (LWCRECLR; contours ranging from 10–60 W m^{-2} at intervals of 10 W m^{-2}) for (A) the multi-reanalysis mean (MRM) over 1980–2014, calculated by averaging the distributions for ERA-Interim, JRA-55, MERRA-2, and CFSR, and (B) CERES EBAF over 2001–2014. Differences relative to CERES EBAF for the MRM same period are shown for (CB) ERA5, (DC) ERA-Interim, (ED) JRA-55, (FE) CFSR/CFSv2, (G) MERRA-2, and (HF) MERRA over 1980–2014CFSR/CFSv2. Contours in panels (DC) through (HF) cover the range within ±2010 W m^{-2} at intervals of 54 W m^{-2}. Tropical mean (30°S–30°N°S–30°N) values of OLR and LWCRE CLR based on each product are shown at the upper right corner and left corners, respectively, of the corresponding panel, with . Tropical mean values for the longwave cloud radiative effect (LWCRE = CLR − OLR) are listed above those for the LWCREOLR.

differences among the reanalyses indicate an inverse relationship between relative biases in OLR and those in HCC. For example, JRA-55, which has the smallest high cloud fractions HCCs in the tropics among the reanalyses, likewise produces the largest tropical mean OLR and the smallest tropical mean LWCRE. Conversely, MERRA-2, with the largest high cloud fractions HCCs among the reanalyses, produces the smallest tropical mean OLR and the largest tropical mean LWCRE. There are some notable exceptions to these relationships, such as differences between ERA5 produces a slightly smaller OLR and a slightly larger LWCRE than ERA-Interimand CFSR over Africa. , and again shows maximum differences over tropical land areas with strong convection. As with HCC, ERA-Interim overestimates high cloud cover relative to the MRM over equatorial Africa but underestimates high cloud cover relative to the MRM over the Sahel. and CFSR/CFSv2 produces a similar qualitative pattern, with slightly smaller differences relative to the MRM. However, whereas produce similar tropical mean values of both OLR and LWCRE (within ±0.5 W m^{-2}). Most differences between these two reanalyses obey the same type of inverse relationship: ERA-Interim tends to overestimate OLR and underestimate the LWCRE relative to the MRM over most of Africa, especially over the Sahel, produces smaller values of OLR in the Indo–Pacific domain (consistent with larger HCCs in this region) while CFSR/CFSv2 tends to underestimate OLR and overestimate the LWCRE relative to the MRM over the same region . Such differences produces smaller values of OLR over tropical mountain ranges (consistent with relatively large HCCs in these locations). There are some notable exceptions though, such as over Africa. ERA-Interim produces slightly

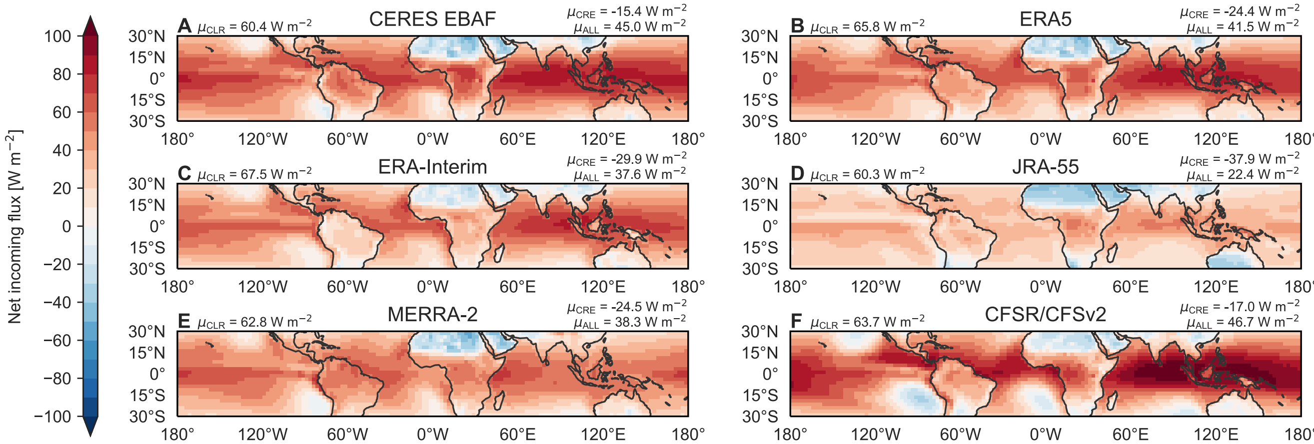

Figure 6. Joint Climatological mean spatial distributions of daily-mean high cloud fraction against all-sky net incoming radiation (AALL; shading) LWCRE and for (BA) SWCRE based on CERES SYN1Deg using gridded data from 2001–2010. Corresponding joint distributions are shown for (CEBAF, H(B) ERA5, (D, IC) ERA-Interim, (E, JD) JRA-55, (F, KE) MERRA-2, and (G, LF) CFSR/CFSv2 during 2001–2014. The 75th percentile of the LWCRE is marked in the upper row. Sub-distributions of high cloud fraction against SWCRE associated with the values of LWCRE that exceeded the corresponding 75th percentile threshold are shown as purple contours in panel Tropical mean (B30°S–30°N) values of ALL and panels clear-sky net incoming radiation (H–LCLR) . Distributions of the LWCRE, SWCRE, and total CRE based on each product are shown in at the upper right and left corners, with SWCRE multiplied by −1 for convenience respectively, of presentation. The thickest boxes mark the interquartile ranges, with the medians marked as horizontal lines and the means marked as starscorresponding panel. The narrower extended boxes indicate Tropical mean values for the 5th, 10th, 90th, and 95th percentilesnet cloud radiative effect (CRE = CLR − ALL) are listed above those for ALL.

larger HCCs in this region (Fig. 1) but CFSR produces smaller values of OLR (this difference is mitigated somewhat in CFSv2; cf. Fig. B2G). This type of inconsistency, in which biases in HCC and OLR do not align with simple expectations, may reflect systematic differences in the depth of convection (and thus cloud top temperature) or the water paths associated with convective anvil clouds. Although we do not directly evaluate differences in cloud top height here (owing in part to the lack of vertically-resolved cloud fraction profiles in CFSR/CFSv2), we note that CFSR/CFSv2 produces a more pronounced peak in cloud water content extending to relatively higher altitudes than ERA-Interim in the tropical mean (Fig. 4F).

Relationships between tropical high cloud fraction and the top-of-atmosphere radiation balance are Figure 6 shows spatial distributions of all-sky net radiation based on CERES EBAF and the five reanalyses, with positive values indicating time-mean energy fluxes into the tropical climate system. Mean values across the tropics are positive (incoming solar radiation exceeds OLR), as indicated here by CERES EBAF (net gain of 45.0 W m^{-2}). This excess of incoming energy in the already energy-rich tropics is essential to the ‘heat engine’ model of the atmospheric circulation, and is contributed primarily by imbalances in the clear-sky fluxes (e.g. Stephens and L’Ecuyer, 2015, and references therein). Net clear-sky fluxes into the tropics are typically somewhat larger in the reanalyses than in CERES, with overestimates as large as 7 W m^{-2} (in ERA-Interim). The closest match in the tropical mean is provided by JRA-55, which is within $0.1\,\mathrm{W\,m^{-2}}$ of CERES (this good agreement does not extend to the all-sky net radiation flux, as detailed below). Cloud effects reduce the energy excess provided by clear sky radiation, as the negative SWCRE outweighs the positive LWCRE. However, most of the reanalyses greatly overestimate the magnitude of this reduction relative to CERES. Such overestimates have implications for atmospheric energy transport, and could result at least in part from the lack of two-way coupling between cloud fields and SST in the reanalyses (e.g. Kolly and Huang, 2018; Wall et al., 2019) . For JRA-55, which overestimates the net CRE by $22.5\,\mathrm{W\,m^{-2}}$ relative to CERES, a little more than half of the bias in the net CRE is attributable to the bias in the LWCRE. The remainder is due to overestimated cloud albedo effects. Similar ratios hold for ERA5 and ERA-Interim, with biases in the LWCRE contributing approximately 55% of the overall biases in each case. For MERRA-2, overestimated cloud albedo effects more than compensate for the stronger LWCRE, producing a net CRE similar to that in ERA5 (approximately $9\,\mathrm{W\,m^{-2}}$ stronger than that from CERES). CFSR/CFSv2 produces a net CRE very similar to that indicated by CERES, implying compensating biases in the SWCRE and LWCRE. However, the horizontal gradients of net radiation are much sharper in this reanalysis than in any of the other data sets included in Fig. 6.

Relationships between tropical HCC and TOA radiation fluxes are examined in more detail in Fig. 7, which shows joint distributions of ~~high cloud fraction~~ HCC against the LW and SW cloud radiative effects. The joint distributions shown in Fig. 7 are two-dimensional frequency distributions analogous to scatter plots~~containing millions of points~~, where the shading indicates the density of the points and ~~outlier values that occur infrequently~~ outliers are omitted. The data used to construct these distributions are daily-mean gridded values within 10°S–10°N during the period 2001–2010~~. This approach provides additional context on both geographical~~ , and thus reflect both spatial and temporal covariability of ~~high cloud cover and radiative fluxes at the top-of-atmosphere~~TOA radiative fluxes and HCC. For this and other analyses that do not span the CFSR/CFSv2 transition (1 January 2011), we omit any reference to CFSv2 and refer to this reanalysis only as CFSR. Data have been interpolated ~~(if necessary)~~ when necessary to 1°×1° spatial grids. ~~As with the LWCRE, values of the SWCRE are computed as clear-sky minus all-sky radiative fluxes. Values are positive-upward, so that the SWCRE in the tropics is typically negative (clouds enhance albedo).~~ The abscissa is reversed for plots of the SWCRE so that larger absolute magnitudes of both LWCRE and SWCRE are located toward the right. Distributions of daily-mean gridded values of LWCRE, SWCRE, and total CRE ~~(LWCRE + SWCRE)~~ are included at the upper right of Fig. 7~~for context~~.

The joint distribution of ~~high cloud fraction~~ HCC against LWCRE based on CERES SYN1Deg indicates a tight, nearly linear relationship between these two variables, in which a large value of ~~high cloud fraction~~ HCC corresponds to a large LWCRE. The 75$^{\mathrm{th}}$ percentile value of LWCRE based on CERES SYN1Deg is $51.0\,\mathrm{W\,m^{-2}}$, which corresponds to ~~a high cloud fraction of roughly 57%~~an HCC of roughly 0.57. Among the reanalyses, ~~the joint distribution of high cloud fraction against LWCRE based on~~ CFSR is most similar to ~~that based on~~ CERES SYN1Deg in its joint distribution of HCC against LWCRE. However, ~~this distribution shows~~ the CFSR distribution has a stronger curvature, so that the 75$^{\mathrm{th}}$ percentile of LWCRE corresponds to a smaller value of LWCRE ($37.6\,\mathrm{W\,m^{-2}}$) despite a similar ~~high cloud fraction (58%~~value of HCC (0.58). JRA-55 has the smallest 75$^{\mathrm{th}}$ percentile value of LWCRE ($23.7\,\mathrm{W\,m^{-2}}$). This value of LWCRE corresponds to ~~a high cloud fraction of around 56%~~ an HCC value of around 0.56 in JRA-55, whereas it corresponds to ~~a high cloud fraction of only 27%~~ an HCC of only 0.27 in CERES SYN1Deg, implying that the relatively small mean ~~high cloud fraction~~ HCC in JRA-55 is not the only reason behind

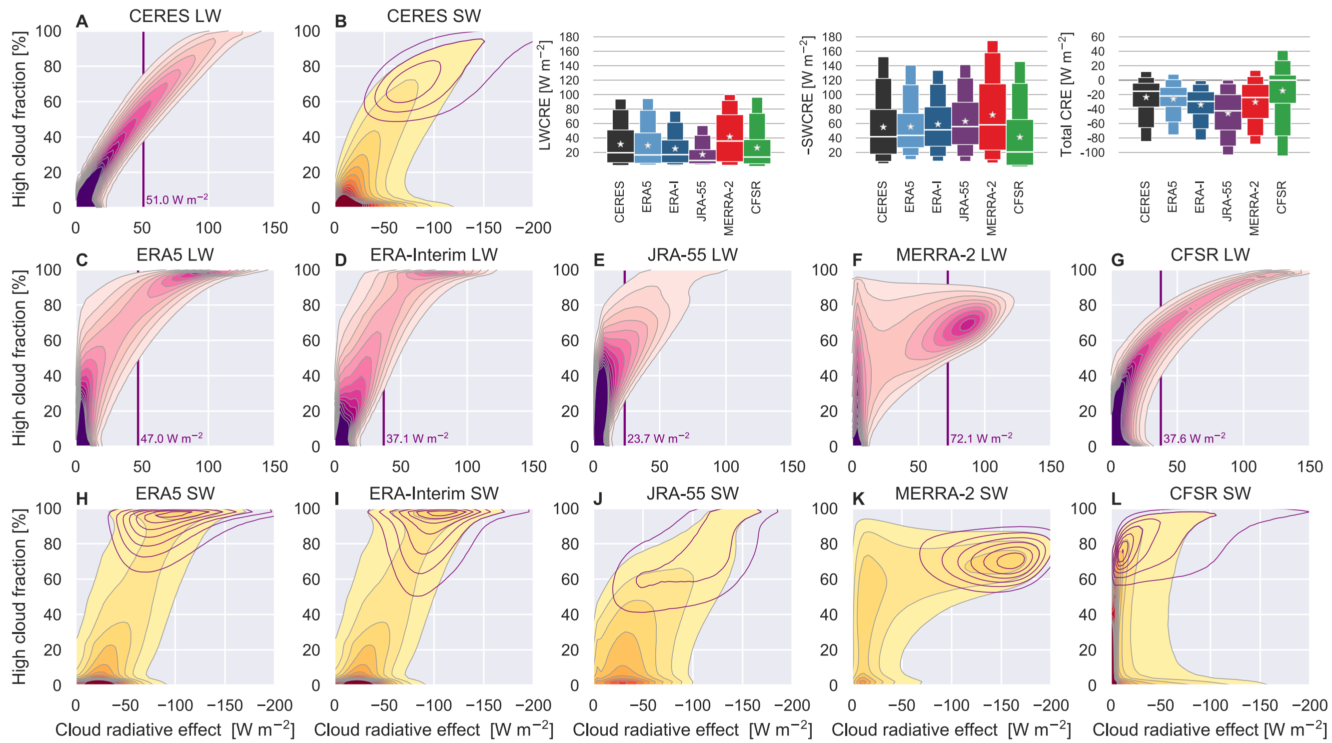

Figure 7. Joint distributions of daily-mean HCC against (A) LWCRE and (B) SWCRE based on CERES SYN1Deg using gridded data from 2001–2010. Corresponding joint distributions are shown for (C, H) ERA5, (D, I) ERA-Interim, (E, J) JRA-55, (F, K) MERRA-2, and (G, L) CFSR. The 75$^{\mathrm{th}}$ percentile of the LWCRE is marked in panels (A) and (C–G). Sub-distributions of HCC against SWCRE associated with the values of LWCRE that exceeded the corresponding 75$^{\mathrm{th}}$ percentile threshold are then shown as purple contours in panels (B) and (H–L). Distributions of the LWCRE, SWCRE, and total CRE are shown in the upper right, with SWCRE multiplied by –1 for convenience of presentation. The thickest boxes mark the interquartile ranges, with the medians marked as horizontal lines and the means marked as stars. The narrower extended boxes indicate the 5$^{\mathrm{th}}$, 10$^{\mathrm{th}}$, 90$^{\mathrm{th}}$, and 95$^{\mathrm{th}}$ percentiles.

relatively ~~low values of~~ weak LWCRE in this reanalysis. Joint distributions based on ERA5, ERA-Interim, and MERRA-2 are qualitatively more distinct, with secondary modes at large values of LWCRE. In ERA-Interim, there is a clear distinction in both variables between the primary mode (associated with small ~~high cloud fractions and small values of LWCRE~~ values of both HCC and LWCRE) and the secondary mode (associated with large ~~high cloud fractions and large values of~~ values of HCC and LWCRE). ~~High cloud fractions~~ HCCs associated with the latter mode are almost exclusively greater than ~~90%~~0.9. The 75$^{\mathrm{th}}$ percentile value (37.1 W m^{-2}) falls between the two modes and corresponds to ~~a high cloud fraction of 65%~~an HCC of 0.65. The distribution based on ERA5 is similar to that based on ERA-Interim, but with a greater fraction of the data (and greater variability) in the large-LWCRE mode. The 75$^{\mathrm{th}}$ percentile value is thus substantially larger in ERA5 (47.0 W m^{-2}) than in ERA-Interim, as is the mean cloud fraction associated with this value (~~75%~~0.75). Bimodality in MERRA-2 takes a different form. The first mode corresponds to small values of LWCRE. Although the peak of this distribution is at small values of ~~high cloud fraction~~HCC, this small-LWCRE mode still exhibits relatively large occurrence frequencies at values of ~~high cloud fraction approaching 100%. The mean high cloud fraction~~ HCC approaching 1. The mean HCC associated with this mode is around ~~35%~~0.35. The second mode peaks at relatively large values of both LWCRE ($\sim$88 W m^{-2}) and ~~high cloud fraction~~ HCC ($\sim$~~70%~~0.7). The 75$^{\mathrm{th}}$ percentile of LWCRE (72.1 W m^{-2}) is contained within the second mode, meaning that the large-LWCRE mode contains more than 25% of the inner tropical data points in MERRA-2. ~~A~~ An LWCRE of 72.1 W m^{-2} corresponds to ~~a high cloud fraction of approximately 68%~~ an HCC of approximately 0.68 in MERRA-2, slightly less than that associated with the same value of LWCRE in CERES SYN1Deg (~~73%~~0.73).

The unique bimodality of the ~~high cloud–LWCRE~~ HCC–LWCRE distribution in MERRA-2 is a consequence of the separation of cloud condensate in the prognostic cloud scheme into 'large-scale' and 'anvil' cloud types. Of these two types, anvil clouds are assigned higher number densities that translate into greater values of optical thickness when the radiation calculations are performed (Bacmeister et al., 2006). ~~Another potentially relevant difference is that the~~ The model used to produce MERRA-2 ~~does not prognostically consider reductions~~ also uses different procedures to relate the evolution of cloud fraction ~~due to autoconversion (Rienecker et al., 2008), which may~~ to autoconversion between the large-scale and anvil cloud types, which appears to result in relatively large values of cloud fraction persisting even as CWC declines ~~. This differs from ERA-Interim and ERA5, for which cloud fraction is among the prognostic variables treated by the cloud scheme (Tiedtke, 1993), and from CFSR, for which cloud fractions are explicitly tied to CWC (Xu and Randall, 1996). The~~ (the small-LWCRE mode in Fig. 7F). Although the treatment of prognostic cloud fraction used in MERRA-2 is conceptually similar to that used in JRA-55 ~~, in which a top-hat-type distribution is used to determine the portion of the grid box for which the total water content exceeds a threshold value (Smith, 1990; Molod, 2012).However, despite this similarity, the two reanalysis systems produce very different behaviors, presumably owing to different characteristic lifetimes of cloud condensate within the atmosphere and the separate treatment of anvil condensate in~~ (Appendix A1), JRA-55 and MERRA-2 produce very different relationships between cloud fraction and condensate. Tuning efforts to increase the amount of cloud ice in the upper troposphere in MERRA-2 were motivated by a desire to improve OLR (recognizing that convective detrainment altitudes are too low in GEOS5, the developers accepted overestimating cloud ice to get OLR right) and upper tropospheric humidity (Molod et al., 2015).The anvil cloud fraction was then kept small relative to the cloud ice content to prevent a worsening of the SWCRE as the LWCRE was increased.

Joint distributions of ~~high cloud fraction~~ HCC against SWCRE are consistent with ~~the expectation that the SWCRE is~~ SWCRE being less tightly linked ~~to high cloud fraction than the LWCRE~~ than LWCRE to HCC in the tropics. However, large ~~high cloud fractions are nonetheless~~ HCCs are typically associated with both large LWCREs and large SWCREs~~in most cases, as indicated by joint distributions conditional on the top quartile of LWCRE.~~ . CERES SYN1Deg and four of the five reanalyses show extensive overlap between large values of LWCRE and large values of SWCRE. CFSR is a notable exception, with large values of LWCRE often corresponding to small values of SWCRE. As a consequence, the distribution of total CRE based on CFSR is broader than those based on CERES or the other reanalyses, with the middle 90% spanning ~~more than 140 W m^{-2},~~ from less than -100 W m^{-2} to approximately $+40$ W m^{-2}. The weaker SWCRE associated with large ~~high cloud fractions in~~

~~CERES results in the total CRE being more positive~~ HCCs results in a more positive total CRE on average, with the median value in CFSR close to zero. These differences can also be seen in the CFSR/CFSv2 climatology, which has sharper spatial gradients of net TOA radiation (Fig. 6F) and a smaller tropical-mean net CRE than any other reanalysis. Although the LWCRE is ~~weaker~~ weakest in JRA-55 ~~than in any other data set~~ among the data sets evaluated here, the tropical-mean SWCRE is larger in JRA-55 than in any data set except MERRA-2. The total CRE is thus substantially more negative in JRA-55 than in any ~~of the other data sets.~~ other reanalysis (see also Fig. 6D). Fewer than 5% of gridded values of total CRE in the tropics are positive in JRA-55. This latter statement ~~is also true of~~ also holds for ERA-Interim; however, greater compensation between the LWCRE and SWCRE in ERA-Interim leads to a narrower distribution and ~~thus~~ a smaller negative bias in the tropical-mean total CRE relative to CERES. MERRA-2 tends to overestimate both the LWCRE and the SWCRE, especially for anvil clouds. However, compensation between these two biases produces a distribution of total CRE that is comparable to ~~but~~ (though slightly broader than) that based on CERES SYN1Deg. Among the five reanalyses, ERA5 shows the ~~greatest~~ closest agreement with CERES SYN1Deg across all three ~~flavors~~ flavours of CRE. The LWCRE in ERA5 is slightly weaker on average than that based on CERES, while the SWCRE is ~~very~~ similar on average but with a narrower distribution. The total CRE is thus slightly more negative in ERA5 than indicated by CERES~~SYN1Deg~~, with a narrower distribution but ~~very close~~ good agreement in the ~~average~~ mean value.

4.2 Radiative heating in the tropical UTLS

In addition to altering top-of-atmosphere radiative fluxes, differences in tropical high clouds may influence radiative heating rates locally within the UTLS. Among the reanalyses considered in this study, neither JRA-55 nor CFSR provide vertically-resolved estimates of radiative heating under clear-sky conditions. To skirt this limitation, we construct composite mean profiles of radiative heating rates conditional on the four quartiles of LWCRE in an adaptation of the approach employed by Zhang et al. (2017)~~, who composited heating rates on OLR rather than LWCRE.~~ . Figure 8 shows these composite profiles for the period 2001–2010, separated into total, LW, and SW radiative heating. Here, Q1 represents daily gridded heating rates for which the LWCRE (at TOA; Fig. 7A and C–G) is in the ~~lowest~~ smallest 25% of all daily gridded values. Q2 and Q3 represent the lower middle and upper middle quartiles, respectively, while Q4 represents heating rates for which the associated LWCRE exceeds the 75th percentile value marked in Fig. 7. The impact of clouds on heating rates is then estimated as the difference between the Q4 and Q1 profiles. Results are very similar for ranked quartiles of all-sky OLR, with OLR reversed so that Q4 corresponds to the smallest values of OLR.

Among these five ~~reanalysis systems~~reanalyses, cloud effects on radiative heating rates are generally smallest in ERA-Interim and largest in MERRA-2. ~~The results~~ Results for these two reanalyses are ~~essentially~~ consistent with those reported for ERA-Interim and MERRA by Wright and Fueglistaler (2013), who ~~showed~~ found that cloud impacts on radiative heating ~~rates~~ in MERRA are qualitatively opposite to those in ERA-Interim through much of the upper troposphere. The response in ERA-Interim is ~~concentrated~~ largest in the 100–200 hPa layer, where radiative heating rates are enhanced ~~by the presence of high clouds~~when LWCRE is large. At lower altitudes in the upper troposphere (200–400 hPa), cloud-induced increases in SW heating are effectively ~~balanced~~ offset by cloud-induced increases in LW cooling. By contrast, ERA5, JRA-55, and CFSR

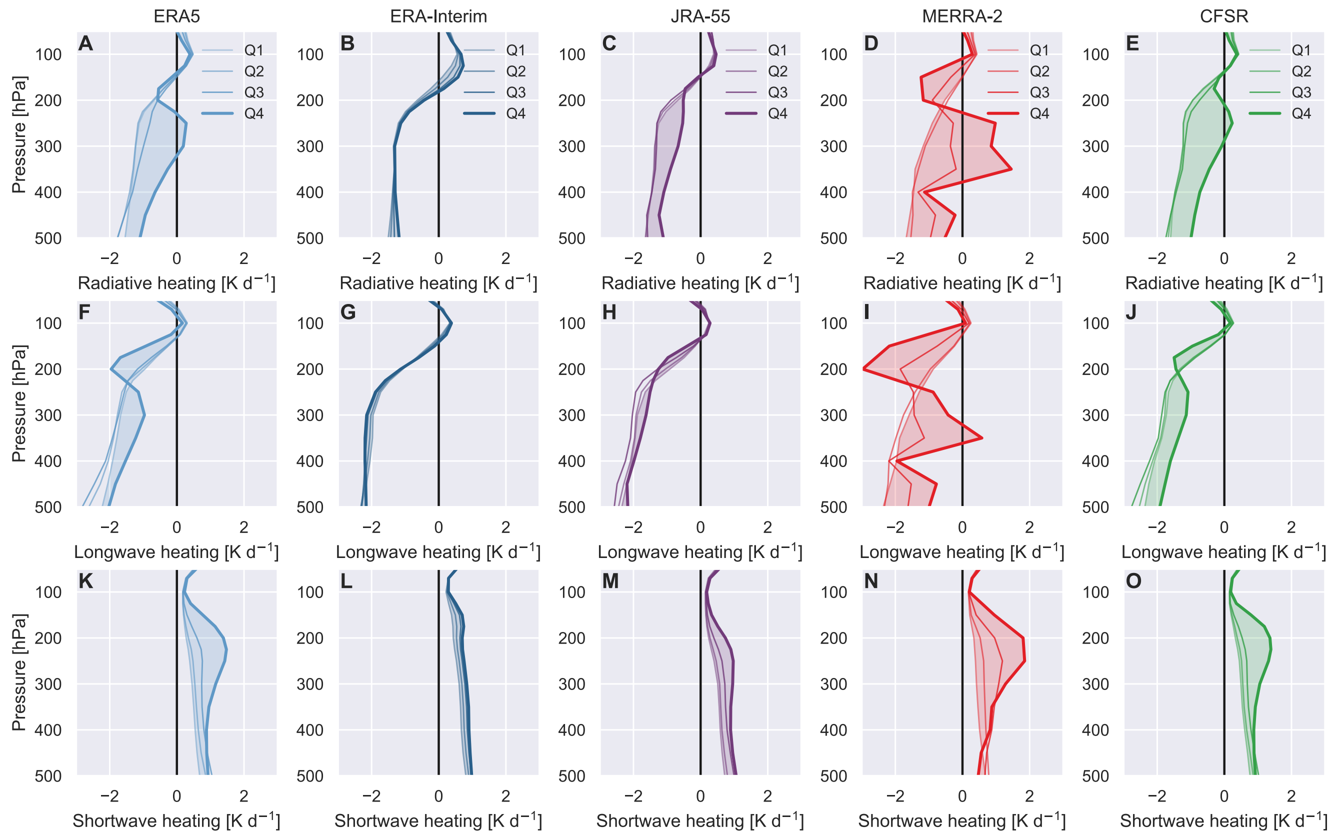

Figure 8. Composite mean profiles of daily-mean radiative heating rates as a function of pressure for the first through fourth quartiles (Q1–Q4) of ~~longwave cloud radiative effect~~ LWCRE in the inner tropics (10°S–10°N; see also Fig. 7) based on (A) ERA5, (B) ERA-Interim, (C) JRA-55, (D) MERRA-2, and (E) CFSR during 2001–2010. Here Q1 refers to the bottom quartile (weak longwave CRE) and Q4 to the top quartile (strong longwave CRE). Total radiative heating rates (upper row; A–E) are separated into (F–J) longwave and (K–O) shortwave components in the lower two rows.

show only weak cloud impacts on total radiative heating at pressures less than 175 hPa. In all three cases, the insensitivity in total radiative heating rates at these altitudes traces back to a near-complete compensation between enhanced LW cooling and enhanced SW heating~~at these altitudes~~. Substantial cloud-related perturbations in the LW and SW components extend upward to around 100 hPa in ERA5 and CFSR, but only to around 150 hPa in JRA-55. MERRA-2 produces the largest cloud impacts on radiative heating rates. Indeed, direct comparison of cloud radiative effects between MERRA and MERRA-2 (not shown) indicates that cloud ~~radiative impacts~~ effects in MERRA are further amplified in MERRA-2, consistent with the increase in CWC in the tropical upper troposphere between MERRA and MERRA-2 (Fig. 4F). ~~The effects of high clouds~~ High cloud effects in MERRA-2 ~~are to~~ reduce radiative heating rates in the 100–200 hPa layer (largely due to enhanced LW cooling, partially offset by enhanced SW heating) and increase radiative heating rates at pressures greater than 200 hPa. The latter

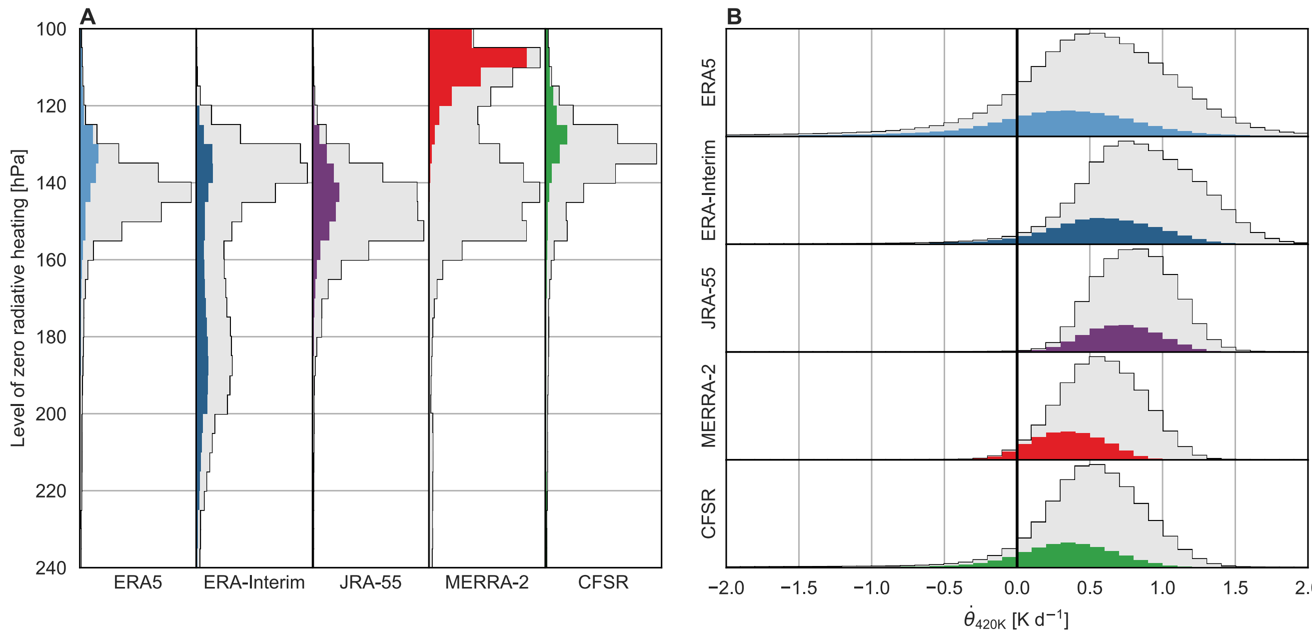

Figure 9. Histograms of (A) the vertical location of the level of zero net radiative heating (LZRH) and (B) the vertical velocity in isentropic coordinates ($\dot{\theta}$ on the 420 K isentropic surface. Data are based on daily mean products from (left-to-right and top-to-bottom) ERA5, ERA-Interim, JRA-55, MERRA-2, and CFSR during 2001–2010. Colored Colour histograms show distributions for the top quartile of longwave cloud radiative effect in each reanalysis (see Fig. 7).

is the result of results from enhanced SW heating near the top of the anvil layer (200–250 hPa) and enhanced LW heating near the base of the anvil layer (300–350 hPa), taking the MERRA-2 profile of tropical-mean cloud water content (Fig. 4F) as a guide. Cloud effects in ERA5 are qualitatively similar to intermediate between those in CFSR and MERRA-2, with an intermediate magnitude between CFSR and MERRA-2 and a smoother profile than MERRA-2. This is consistent with the relatively pronounced convective anvil in the ERA5 profile of tropical-mean CWC profile based on ERA5 (Fig. 4F), which is more consistent with better matches the profiles produced by CFSR and MERRA-2 than with that produced by ERA-Interim.

Differences in the radiative impacts of tropical high clouds can lead in turn are linked to differences in transport through the tropical tropopause layer TTL and lower stratosphere (Fueglistaler and Fu, 2006; Yang et al., 2010). Oft-used metrics in this regard Relevant metrics include the level of zero net radiative heating (LZRH) and the rate of diabatic ascent at the base of the ‘tropical pipe’, which defines the upward branch of the Brewer–Dobson circulation (e.g. Fueglistaler et al., 2009; Dessler et al., 2014). Here, the The LZRH marks the boundary between negative all-sky radiative heating rates (corresponding to net descent) in the tropical troposphere and positive radiative heating rates (corresponding to net ascent) in the tropopause layer TTL and lower stratosphere. We identify this level by using linear interpolation of daily-mean gridded radiative heating rates in $\ln(p)$ to determine pressure at the zero crossing. We further require that radiative heating rates remain positive above the identified LZRH to at least the 70 hPa isobaric level. To represent the radiative signature of (Sect. 2.3; see also Folkins et al., 1999; Gettelman et al., 2

. To represent ascent at the base of the tropical pipe, we use the vertical velocity in potential temperature coordinates ($\dot{\theta}_{\rm rad}$) ~~as diagnosed~~ at the 420 K isentropic level, near the top of the ~~tropical tropopause layer. Figure 9 shows~~ TTL. We evaluate distributions of LZRH pressure (Fig. 9A) and $\dot{\theta}_{\rm rad}$ (Fig. 9B) at 420 K based on ~~the~~ ERA5, ERA-Interim, JRA-55, MERRA-2, and CFSR ~~reanalyses~~ during 2001–2010. Distributions conditional on the top quartile of LWCRE (Q4) ~~are shaded in color~~for each reanalysis are shown in colour.

The largest differences in ~~the distributions of LZRH altitudes~~ LZRH distributions are between ERA-Interim and MERRA-2 (Fig. 9A). Neglecting the influence of clouds, the primary mode of the ERA-Interim distribution ($p \sim 140$ hPa) is ~~shifted to~~ located at slightly higher altitudes than that in MERRA-2 ($p \sim 150$ hPa). ~~The altitudes of these~~ These primary modes match the vertical locations of the clear-sky LZRH in each system well (not shown). The more striking distinction between ERA-Interim and MERRA-2 ~~concerns~~ is in the impacts of clouds on the LZRH altitude. Whereas clouds tend to lower the LZRH in ERA-Interim (to around 170 hPa on average), clouds raise the LZRH significantly in MERRA-2 (to around 110 hPa)~~, with~~ . This difference has important implications for the efficiency of mass and constituent transport from the deep convective detrainment level (200∼300 hPa) into the tropical lower stratosphere. In MERRA-2, the cloudy and clear-sky modes of the distribution are almost completely distinct~~, suggesting that transport regimes in the tropical upper troposphere are approximately binary in this model.~~ . By contrast, the breadth of the LZRH distribution based on ERA-Interim (and especially the breadth of the distribution associated with the largest values of LWCRE) indicates that ERA-Interim produces a broad spectrum of cloudy states. This diagnostic thus helps to clarify the environmental conditions ~~that give rise to~~ associated with the two very different tropical mean ~~cloud water content~~ CWC profiles in Fig. 4F, with the pronounced anvil layer in MERRA-2 in sharp contrast to the gradual decrease of ~~cloud water content~~ CWC with height in ERA-Interim. Distributions of the LZRH location based on ERA5, JRA-55, and CFSR are more consistent with each other. Each distribution has one major mode, although the altitude of the LZRH tends to be highest in CFSR (median: 134 hPa), followed by ERA5 (144 hPa) and JRA-55 (148 hPa). All three ~~of ERA5, JRA-55, and CFSR~~ reanalyses indicate slight upward shifts toward lower pressures (by around 5 hPa) in the median LZRH location associated with the largest values of LWCRE, but these shifts are much less pronounced than that ~~in~~ suggested by MERRA-2.

Distributions of $\dot{\theta}_{\rm rad}$ at 420 K (Fig. 9B) are more consistent among the reanalyses. Differences in the mean value are consistent with ~~those reported elsewhere~~previous assessments (Schoeberl et al., 2012; Abalos et al., 2015; Tao et al., 2019), with ERA-Interim (average: 0.82 K day^{-1}) and JRA-55 (0.80 K day^{-1}) ~~indicating~~ having stronger lower-stratospheric ascent than MERRA-2 (0.56 K day^{-1}) or CFSR (0.49 K day^{-1}). The mean value in ERA5 (0.49 K day^{-1}) is consistent with those in MERRA-2 and CFSR, but with a much broader distribution. Our focus here is ~~mainly~~ on the cloud effects and the role ~~that~~ they play in the overall differences. All five reanalyses indicate ~~that~~ weaker lower stratospheric radiative heating rates ~~are reduced~~ in atmospheric columns with large values of LWCRE. As with many of the diagnostics examined in this study, this effect is least pronounced in JRA-55, with ~~differences between~~ the mean for Q1 (smallest LWCREs) ~~and Q4 (largest LWCREs) of~~ only 0.13±0.03 K day^{-1} larger than that for Q4 (largest LWCREs). This relatively small cloud influence ~~likely contributes~~ may contribute to the relatively narrow distribution of $\dot{\theta}_{\rm rad}$ in JRA-55. By contrast, the much broader distributions of $\dot{\theta}_{\rm rad}$ in ERA5 and ERA-Interim are accompanied by large cloud effects, with differences of 0.49±0.12 K day^{-1} between Q1 and Q4 in ERA5 and 0.45±0.06 K day^{-1} in ERA-Interim. These large cloud effects ~~are consistent with~~ reflect sharper spatial gradients in ~~high cloud fraction~~ HCC (Fig. 1c) and LWCRE (Fig. 5c) between ~~the canonical~~ tropical deep convective regions ~~of the tropics~~ and surrounding areas in the ~~two~~ ECMWF reanalyses relative to JRA-55. The cloud influence on $\dot{\theta}_{\mathrm{rad}}$ in MERRA-2 is comparable to that in ERA-Interim, with a difference of 0.39±0.03 K day^{-1} between Q1 and Q4. However, the distribution based on MERRA-2 is compressed toward the mean relative to that based on ERA-Interim, with fewer extreme values and shorter tails. Only 8% of $\dot{\theta}_{\mathrm{rad}}$ values in MERRA-2 fall outside the interval $[0, 1]$ K day^{-1}, as opposed to 36% of values in ERA-Interim (33% in ERA5). This pairing of large cloud effect and narrow distribution implies a strict stratification of lower stratospheric heating rates with respect to LWCRE, with values of $\dot{\theta}_{\mathrm{rad}}$ ~~based on~~ in MERRA-2 approaching those ~~based on~~ in JRA-55 as the effects of clouds are reduced. The mean difference ~~in $\dot{\theta}_{\mathrm{rad}}$~~ between these two reanalyses is ∼0.4 K day^{-1} in Q4 (where the mean LWCRE in MERRA-2 is more than double that in JRA-55) ~~,~~ but only ∼0.1 K day^{-1} in Q1 (where mean values of LWCRE are 3.1 W m^{-2} in both systems). Our results thus support the suggestion by Tao et al. (2019) that differences in climatological ~~high cloud cover~~ HCC in the tropics can explain much but not all of the difference in lower stratospheric ~~air mass ascent~~ ascent rates between these reanalyses. The cloud effect on lower stratospheric heating rates is 0.31±0.09 K day^{-1} in CFSR. The uncertainty ~~in this estimate~~ is relatively large ~~because~~ in CFSR because of large variance in distributions of $\dot{\theta}_{\mathrm{rad}}$ ~~based on CFSR have larger variance within each quartile of LWCRE~~ within each LWCRE quartile (primarily due to higher occurrence frequencies of negative values in all four quartiles). Approximately 4% of $\dot{\theta}_{\mathrm{rad}}$ values associated with the relatively cloud-free Q1 and Q2 groupings in CFSR are negative~~(implying diabatic descent)~~, an order of magnitude larger than the fraction in ERA-Interim and several orders of magnitude larger than the fractions in JRA-55 and MERRA-2. However, ~~it is clear that~~ the largest variance in $\dot{\theta}_{\mathrm{rad}}$ is ~~that~~ produced by ERA5. ~~This~~ Although variance decreases with decreasing LWCRE~~; however~~, the fraction of negative $\dot{\theta}_{\mathrm{rad}}$ values in Q1 and Q2 (9%) is still more than double that in CFSR. The broader distribution of diabatic heating rates in this reanalysis may be related to improved consistency between diabatic and kinematic vertical motion in the lower stratosphere in ERA5 relative to ERA-Interim (Hoffmann et al., 2019).

5 Possible origins

The prognostic cloud parameterizations ~~used by~~ in the reanalysis models consider two sources of high clouds: detrainment from deep convection and in situ formation due to large-scale saturation (see Appendix A). Sinks include autoconversion of cloud water to precipitation and evaporation or sublimation of cloud water into ~~subsaturated~~ unsaturated air. In considering the origins of differences in high clouds among the reanalyses, we therefore focus on factors that ~~might~~ can influence the sources and sinks of high cloud ~~, as well as metrics that may reflect~~ or clarify coupled relationships between high clouds and their environment. With respect to the convective source, we examine relationships ~~between high cloud fraction and~~ with SST, thermodynamic stability in the lower troposphere, grid-scale vertical velocity and RH in the middle troposphere (500 hPa), and the mean vertical profile of moist static energy (MSE). ~~To assess the in situ source and evaporation sink, we examine~~ We then use relationships among CWC, RH, and radiative heating ~~rates~~ near the base of the ~~tropical tropopause layer~~ TTL (150 hPa) and ~~just below~~ near the cold point tropopause (100 hPa) to assess the relative balance of in situ versus convective clouds in

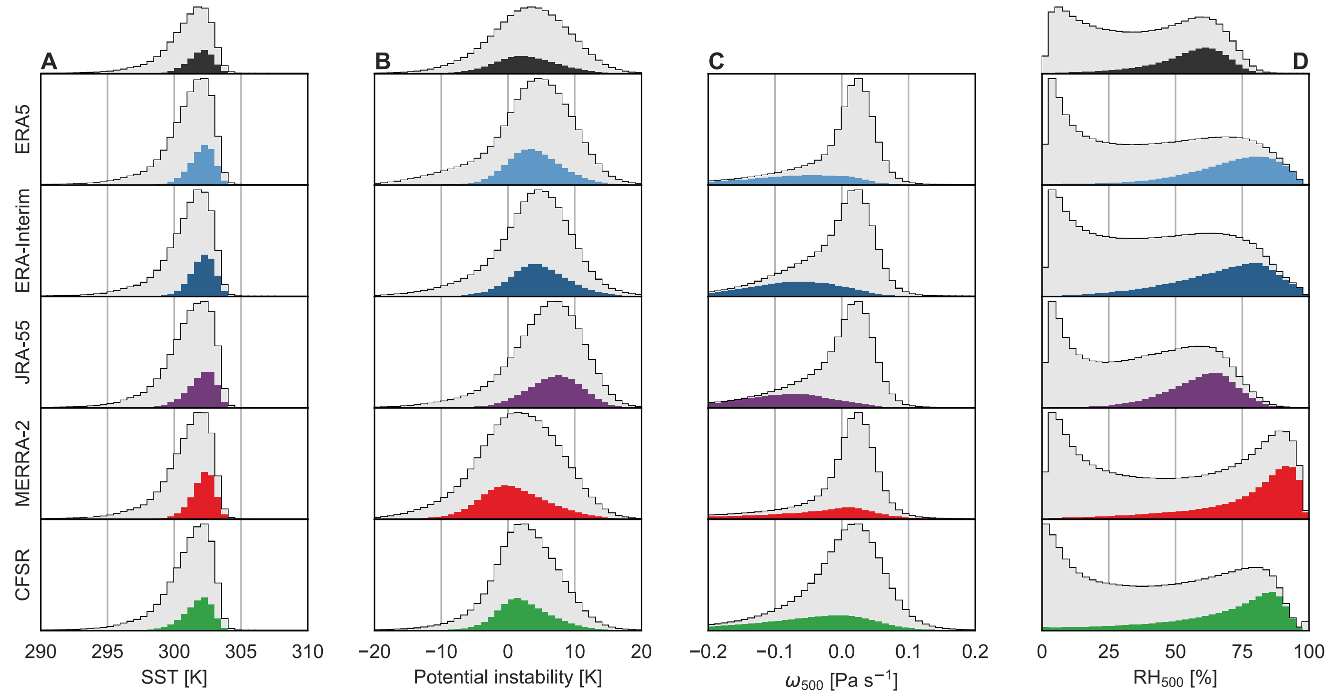

Figure 10. Histograms of (A) sea surface temperature (SST), (B) potential instability ($\theta_{e,850} - \theta_{e,500}$), (C) grid-scale vertical velocity in the middle troposphere (ω_{500}), and (D) relative humidity in the middle troposphere (RH_{500}). Data are based on daily mean products at $1° \times 1°$ resolution from (top-to-bottom) ERA5, ERA-Interim, JRA-55, MERRA-2, and CFSR during 2001–2010 ~~within~~ in the inner tropics (10°S–10°N). Observational estimates are shown along the top axis where available, ~~and include~~ with data from CERES SYN1Deg (LWCRE), OISST~~version 2~~ v2 (SST), and AIRS ~~TqJoint~~ (potential instability and RH_{500}). Distributions that include AIRS data are ~~based on data from~~ for 2003–2010 rather than 2001–2010. ~~Colored~~ Colour histograms show distributions for the top quartile of ~~longwave cloud radiative effect~~ LWCRE in each ~~reanalysis~~ data set (see Fig. 7). Mean values for each distribution are listed in Table 3.

the TTL. All relationships are assessed ~~at the daily timescale within~~ using daily mean data in the inner tropics (10°S–10°N). The use of daily means collapses ~~important~~ diurnal variations in tropical convective activity that may be poorly represented ~~by the~~ in reanalyses (e.g. Bechtold et al., 2014). ~~This diurnal~~ Diurnal variability may imprint on relationships among daily-mean variables, but we do not explore this possibility here. We cannot fully distinguish between causes and effects. All of the variables we examine in this section are intimately connected to cloud and convection processes, so that differences in these variables may indicate the causes of cloud biases, reflect the effects of those biases, or both of the above. To address this, we link differences in the examined variables to differences in model parameterizations or data assimilation procedures whenever possible. Although we cannot unequivocally tie each bias to a distinct origin of this type, this information may be helpful both for understanding differences between the reanalyses and for highlighting potential targets for improvement in the reanalysis systems.

Table 3. Mean values of the distributions shown in Fig. 10 for all data point points in the inner tropics ('All'; 10°S–10°N) and for the top quartile of LWCRE in the same region ('Q4'). The row labeled 'Observed' summarizes the results when LWCRE is taken from CERES SYN1Deg, SST from OISST v2, and potential instability and mid-tropospheric RH from AIRSTqJoint.

Product	Sea surface temperature All	Sea surface temperature Q4	Potential instability All	Potential instability Q4	Mid-tropospheric ω All	Mid-tropospheric ω Q4	Mid-tropospheric RH All	Mid-tropospheric RH Q4
ERA5	301.0 K	302.0 K	3.4 K	3.9 K	$-0.02\,\mathrm{Pa\,s^{-1}}$	$-0.11\,\mathrm{Pa\,s^{-1}}$	42%	70%
ERA-Interim	300.9 K	302.1 K	3.6 K	4.7 K	$-0.02\,\mathrm{Pa\,s^{-1}}$	$-0.09\,\mathrm{Pa\,s^{-1}}$	42%	67%
JRA-55	301.0 K	301.9 K	5.4 K	6.7 K	$-0.02\,\mathrm{Pa\,s^{-1}}$	$-0.11\,\mathrm{Pa\,s^{-1}}$	37%	58%
MERRA-2	300.9 K	302.1 K	1.4 K	1.0 K	$-0.02\,\mathrm{Pa\,s^{-1}}$	$-0.09\,\mathrm{Pa\,s^{-1}}$	49%	76%
CFSR	300.9 K	301.6 K	2.6 K	2.4 K	$-0.01\,\mathrm{Pa\,s^{-1}}$	$-0.08\,\mathrm{Pa\,s^{-1}}$	44%	67%
Observed	300.9 K	301.9 K	3.1 K	2.8 K	--	--	37%	54%

5.1 Convection and its environment

Tropical deep convection tends to cluster over the warmest SSTs. This behavior is captured in behaviour is captured by all five of the reanalysis systems, with the largest high cloud fractions LWCREs systematically associated with the largest SSTs. Tropical-mean SSTs prescribed during the 2001–2010 analysis period are very similar among the reanalyses (Table 3). CFSR exhibits the weakest relationship between SST and high cloud cover, with Q4 of the LWCRE associated with a mean SST of 301.6 K (relative to 301.9–302.1 K in the other four reanalyses). The observation-based benchmark, with CERES SYN1Deg used to estimate daily-mean LWCRE and OISST v2 (Reynolds et al., 2007) for daily-mean SST, likewise assigns a mean value of 301.9 K to Q4, 1 K warmer than the tropical mean. CFSR is the only coupled atmosphere–ocean data assimilation system among these five reanalyses, making it the only one with the potential for two-way interactions between high clouds and SST (although analyzed SST is still pegged quite tightly to observations; Saha et al., 2010). Note that OISST v2 (Reynolds et al., 2007) was used as an atmospheric lower boundary condition during portions of this intercomparison period by ERA-Interim (July–December 2001) and MERRA-2 (through March 2006), and as the primary input to SST analyses by CFSRthroughout (Fujiwara et al., 2017, their Table 4). The observational benchmark distribution of SST is therefore not strictly independent. This benchmark, using CERES SYN1Deg for daily-mean LWCRE and OISST v2 for daily-mean SST, suggests that the mean SST for Q4 is 1 K warmer than the tropical mean. Q4 in CFSR exhibits the weakest difference relative to tropical mean SST (0.7 K), with values in the other reanalyses ranging from 0.9 K (JRA-55) to 1.2 K (ERA-Interim and MERRA-2). CFSR is the only coupled atmosphere–ocean data assimilation system among these five reanalyses, giving it the potential for two-way interactions between high clouds and SST (although analyzed SST is still pegged quite tightly to observations; Saha e
.

Figure 10B summarizes distributions of lower tropospheric potential instability (defined as the difference in θ_e between 850 hPa and 500 hPa; Eq. 2) for all tropical points and for points associated with Q4 of LWCRE. Values of potential instability in the tropics tend to be positive in all five reanalyses. However, this tendency toward positive values is weaker for MERRA-

2 and CFSR than for ERA5, ERA-Interim, or JRA-55, indicating systematic differences in the moist thermodynamic state of the tropical atmosphere ~~among these reanalyses~~ (see also Table 3). Moreover, while ERA5, ERA-Interim, and JRA-55 indicate larger potential instabilities associated with Q4 of LWCRE than in the tropical mean, MERRA-2 and CFSR indicate the opposite. The latter is in better agreement with AIRS. For ERA-Interim, these differences may be linked to the convective closure (Appendix A2). The convection scheme in ERA-Interim specifies an adjustment timescale that, in practice, often exceeds the model time step (especially at coarser resolutions; Bechtold et al., 2008, their Fig. 1). ~~As such, potential~~ Potential instability in convective locations (Q4) may thus be shifted toward larger positive values in ERA-Interim (Fig. 10B). The new closure (Bechtold et al., 2014) and finer model resolution used in ERA5 reduce the difference between the Q4 and tropical mean values of potential instability by about ~~half~~ 50% (Table 3). The discrepancy between JRA-55 and the other reanalyses has a different origin. Figure 11A shows vertical profiles of MSE averaged over the upper and lower quartiles of daily gridded LWCRE within the inner tropics (10°S–10°N). A 'kink' is evident in the vertical profile for JRA-55 between 900 hPa and 850 hPa but not in any of the other profiles. This kink arises because the Q4 profile in JRA-55 has a warm bias at 850 hPa (+0.4 kJ kg^{-1} relative to ERA5; Fig. 11B, lower row) but a cool and dry bias at 900 hPa (total -1.0 kJ kg^{-1}; not shown). The convective scheme in JRA-55 restricts cloud base to the model level at ∼900 hPa (JMA, 2013). Thermodynamic instabilities that develop at higher levels (such as the 850 hPa level used to compute potential instability) are thus ~~more~~ difficult for the convection scheme to eliminate.

Decomposing differences in moist static energy into contributions from ~~differences in~~ temperature, specific humidity, and geopotential (~~not shown~~Fig. 11B–D), we find that ~~differences in atmospheric moisture content are the most influential at both the~~ the largest spreads result from differences in moisture content at both 850 hPa and 500 hPa~~levels~~. At 850 hPa, latent energy ($L_v q$) based on CFSR and MERRA-2 is 1–2 kJ kg~~−1~~ $^{-1}$ less than that based on JRA-55, ERA5, or ERA-Interim ~~.~~ (Fig. 11C, lower panel). Meanwhile, at 500 hPa, latent energy based on MERRA-2 is nearly 3 kJ kg^{-1} larger than that in JRA-55, and more than 1 kJ kg^{-1} larger than that in ERA5, ERA-Interim, or CFSR ~~. Biases in the dry enthalpy component (~~(Fig. 11C, middle panel). Biases in c_pT ~~)~~are on the order of ±0.5 kJ kg^{-1} at both levels ~~.~~(Fig. 11B, lower two panels). For JRA-55 and MERRA-2, temperature biases ~~tend to~~ compensate for humidity biases at 850 hPa but exacerbate the effects of humidity biases at 500 hPa. The relationship between potential instability and LWCRE ~~produced by~~ in CFSR is most similar to that based on observations in terms of mean values, with AIRS estimates 0.4–0.5 K larger than those based on CFSR for both the tropics as a whole and the top quartile of LWCRE (Table 3). However, the distribution of potential instability based on AIRS is broader than that based on CFSR, and in that sense is more reminiscent of the distributions based on MERRA-2 or ERA5 (Fig. 10B).

~~Negative biases in both moisture content and temperature at 500 hPa in JRA-55 relative to the other reanalyses may stem in part from the inability to trigger convection from instabilities at altitudes above 900 hPa; however, the shift of the liquid–ice transition toward warmer temperatures also plays a role in dehydrating the middle troposphere. The much larger moisture content at 500 hPa in can also be linked to details of the cloud parameterization. We discuss these possibilities further after briefly highlighting~~ We briefly highlight two other features of the MSE profiles shown in Fig. 11A. First, lower tropospheric values of MSE associated with Q4 are evidently larger in ~~all of~~ the reanalyses than ~~those based on~~ in the AIRS observations. This may indicate that the reanalyses are systematically too moist or too warm in the lower troposphere, but may also reflect

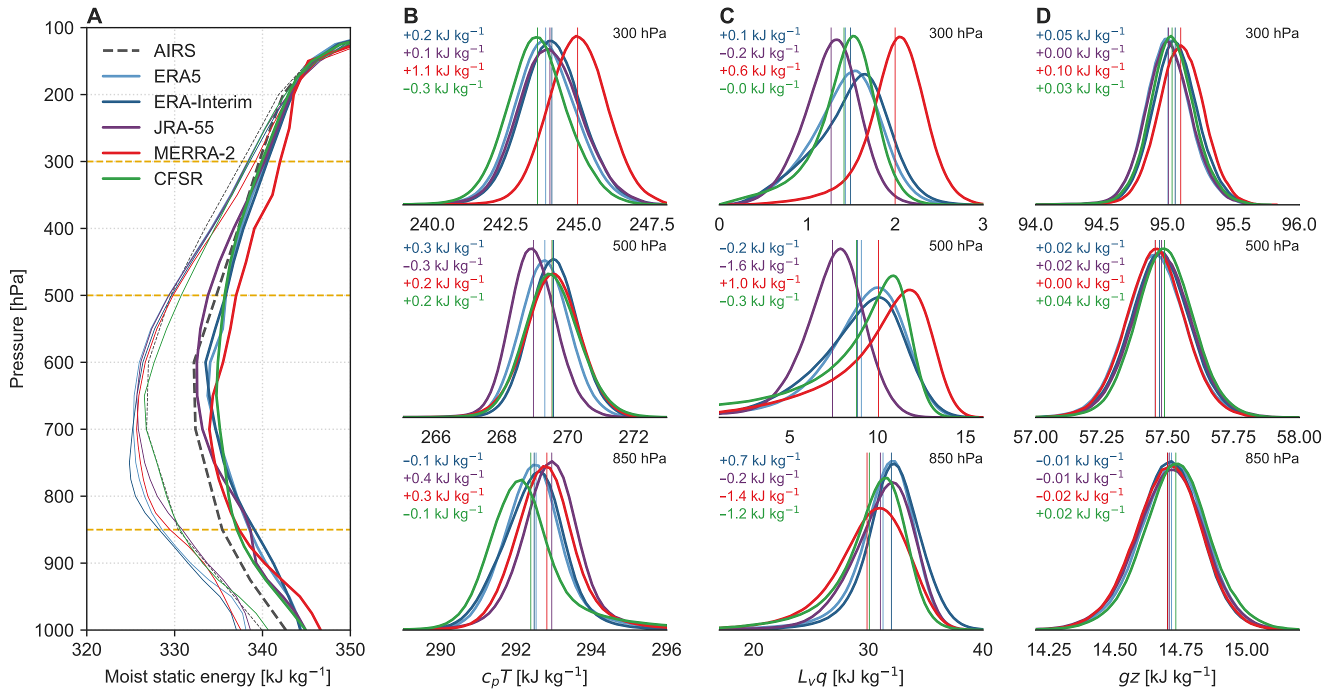

Figure 11. (A) Composite vertical profiles of moist static energy (MSE) for ERA5 (cyan), ERA-Interim (blue), JRA-55 (purple), MERRA-2 (red), and CFSR (green) averaged for the upper (Q4; thick lines) and lower (Q1; thin lines) quartiles of daily-mean LWCRE during 2001–2010. Profiles calculated from AIRS observations (September 2002–December 2010; grey dashed lines) are ~~shown for context. AIRS profiles are~~ conditioned on quartiles of daily-mean LWCRE from CERES SYN1Deg. At right are distributions of the (B) temperature (c_pT), (C) moisture (L_vq), and (D) geopotential (gz) components of MSE for Q4 from each reanalysis at the levels marked by yellow dashed lines in (A): 850 hPa (lower row), 500 hPa (centre row), and 300 hPa (upper row). Mean values are marked as vertical lines; biases in these mean values relative to the mean value from ERA5 are colour-coded at the upper left of each panel (each list from top: ERA-Interim, JRA-55, MERRA-2, CFSR).

systematic errors or sampling biases (e.g. cloud clearing) in the AIRS observations. Second, MERRA-2 shows ~~substantially~~ much larger values of MSE in the upper troposphere ~~in~~ of convective regions relative to ~~the~~ other reanalyses. This bias results from both greater humidity (perhaps due to greater detrainment of cloud water and subsequent condensate evaporation; Fig. 4) and systematic warm biases (possibly linked to more intense cloud radiative heating at anvil level; Fig. 8). At 300 hPa, the excess Q4 MSE in MERRA-2 relative to ~~ERA-Interim~~ ERA5 is on average ~~62~~61% attributable to differences in ~~the dry enthalpy component~~ temperature (c_pT~~) and 35~~; upper panel of Fig. 11B) and 33% attributable to differences in ~~the latent energy component~~ moisture content (L_vq; Fig. 11C). The ~~residual discrepancy (3~~remainder (~6%) arises from differences in geopotential ~~. This difference~~ (Fig. 11D). This bias in upper tropospheric MSE is systematic throughout the tropics (e.g. the Q1 profile in Fig. 11), but with smaller magnitudes and temperature biases ~~a proportionally greater contributor outside of the~~

contributing more outside of deep convective regions. Greater upper tropospheric MSE in MERRA-2 implies stronger gross moist stability, and specifically a stabilization of the upper troposphere that may suppress the average depth of convection. The ~~resulting~~ lower, more extensive anvil deck in MERRA-2 ~~appears to be a key factor in the relatively~~ contributes to both strong cloud-top radiative cooling ~~in this reanalysis~~ around 200 hPa (Fig. 8) and the inability of convective heating to compensate for this cooling. As noted previously for MERRA, this combination yields a physically implausible layer of time-mean zonal-mean diabatic descent centered near 200 hPa that extends across the entire tropics (Wright and Fueglistaler, 2013).

Figure 10C ~~and D show~~ shows distributions of grid-scale vertical velocity (ω) ~~and RH~~ in the middle troposphere (500 hPa). Distributions ~~of vertical velocity~~ for the whole tropics are qualitatively similar across the five reanalyses, with peaks at small positive values (subsidence) and long tails toward large negative values (ascent). Larger values of LWCRE in ERA-Interim and JRA-55 are associated almost exclusively with grid-scale ascent in the middle troposphere. This relationship is less pronounced in MERRA-2 and CFSR~~(i.e. large LWCREs are more frequently associated with mid-tropospheric descent),~~ , although the strongest mid-tropospheric ascent rates are associated with Q4 in all five reanalyses. These differences may be understood in terms of differences in the convective triggers (Appendix A2), which explicitly consider large-scale convergence in ERA-Interim and JRA-55 but not in MERRA-2 or CFSR. ~~Explicit dependence~~ Dependence of the convective trigger on large-scale vertical velocity was eliminated from the ECMWF atmospheric model between the version used for ERA-Interim and that used for ERA5 (Bechtold et al., 2008). No observational benchmark is available for evaluating these distributions.

Distributions of mid-tropospheric RH (Figure 10D; defined here with respect to liquid water) are bimodal in all five reanalyses, with peaks at both very small values ($< 10\%$) and relatively large values ($> 50\%$). The largest values of LWCRE tend to be associated with large values of mid-tropospheric relative humidity, although this relationship is tighter for MERRA-2 and CFSR than for ERA5, ERA-Interim, or JRA-55. The largest differences among the distributions are at the upper end of the range, and can be ~~explained to some extent~~ at least partially explained by differences in the treatment of the liquid–ice transition (Appendix A; Fig. A1). As JRA-55 has the strictest transition from liquid to ice, mid-tropospheric RH with respect to liquid water is generally less than 75%. ERA-Interim and ERA5 prescribe more gradual transitions from liquid to ice, and thus produce larger relative humidities with respect to liquid water. Another potentially important parameter is the critical RH at which large-scale cloud formation (or evaporation of cloud water) is assumed to occur. This value is more than 90% in MERRA-2 at 500 hPa as opposed to around 80% in ERA5 and ERA-Interim, leading MERRA-2 to produce a larger frequency of very high relative humidities at this level. Tighter distributions of mid-tropospheric RH associated with the largest values of LWCRE (Fig. 10D) also suggest that deep convection may be more sensitive to mid-tropospheric entrainment of dry air in MERRA-2 and CFSR than in ERA5, ERA-Interim, or JRA-55. For MERRA-2 this is consistent with the application of a Tokioka-type entrainment condition (Bacmeister and Stephens, 2011): ~~whether a plume is triggered depends on whether the required entrainment rate exceeds~~ entrainment rates smaller than a randomly-selected minimum (the Tokioka parameter) are disallowed. For small values of RH, entrainment is efficient in diluting the updraft, so that ~~only small entrainment rates will permit plumes that~~ plumes can only reach the upper troposphere ~~. If the required value of entrainment is smaller than the randomly-selected Tokioka parameter, plumes that reach the upper troposphere will not be allowed. The application of the~~ when the entrainment rate is small. The Tokioka condition thus tightens the preference for deeper convection to occur in

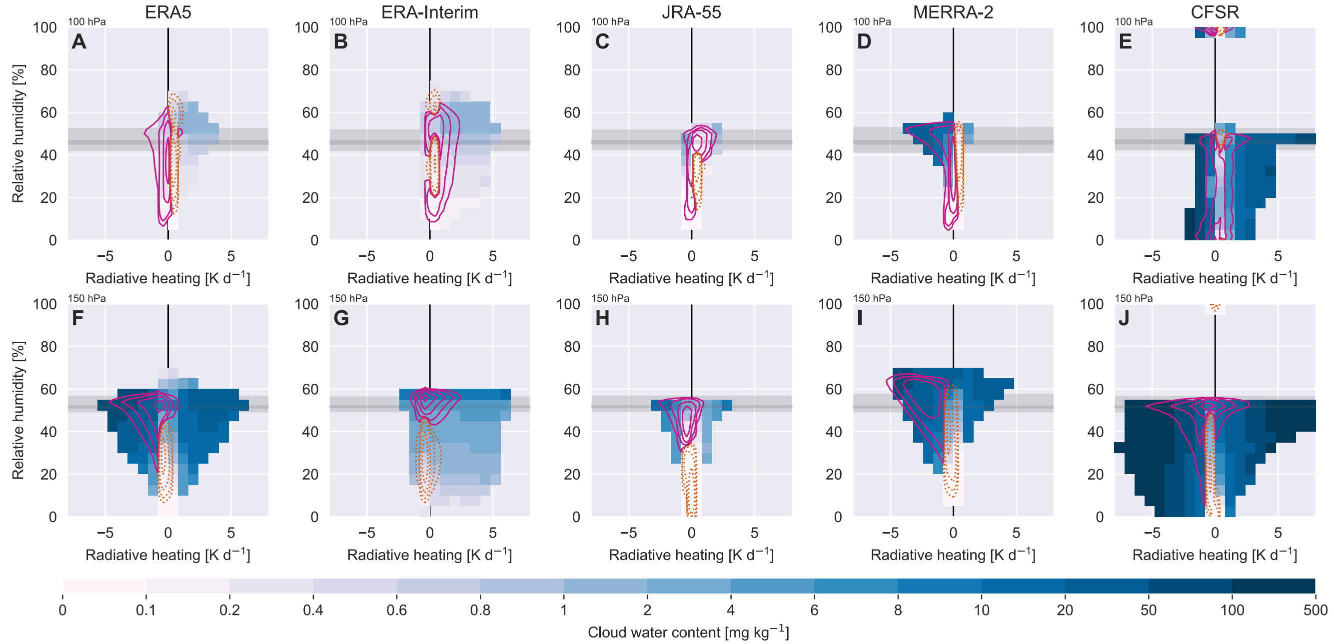

Figure 12. Composite distributions of daily-mean ~~high cloud fraction~~ CWC as a function of radiative heating rate and grid-scale relative humidity (RH) in (A, F) ERA5, (B, G) ERA-Interim, (C, H) JRA-55, (D, I) MERRA-2, and (E, J) CFSR on the 100 hPa (upper row; A–E) and 150 hPa (lower row; F–J) isobaric surfaces. RH is calculated with respect to liquid water. Grey shaded regions in each panel mark ranges of ice saturation ratios (e_i^*/e_ℓ^*) at these levels, with light shading marking the minimum and maximum and dark shading marking the interquartile range. Solid pink contours mark paired values of radiative heating and RH that are more commonly associated with cloudy conditions (Q4 of the daily-mean LWCRE) than with clear-sky conditions (Q1 of the LWCRE); dashed orange contours mark the opposite (values more commonly associated with Q1 than Q4). Composite mean CWCs are masked for bins containing fewer than 200 samples.

more humid environments. Entrainment rates are also relatively large in CFSR, which uses a base entrainment rate equal to the maximum ~~entrainment~~ rate in JRA-55 and ~~approximately~~ about an order of magnitude larger than the base ~~entrainment~~ rate in ERA-Interim (Appendix A2). Among the reanalyses, the distribution of mid-tropospheric RH in JRA-55 is most consistent with that based on AIRS. However, ~~just~~ as for lower tropospheric MSE, caveats concerning sampling and cloud-clearance biases apply when interpreting ~~AIRS-based estimates~~the AIRS distribution.

5.2 Clouds in the TTL

Tropical high clouds in the reanalyses may also originate via the parameterized effects of grid- or subgrid-scale saturation. In the TTL, such in situ cloud formation is often associated with adiabatic cooling linked to wave activity or ~~radiatively-driven~~ slow ascent (Massie et al., 2002; Schoeberl et al., 2019). Figure 12 summarizes relationships among CWC, radiative heating rates, and RH at isobaric levels near the base of the TTL (150 hPa) and near the tropopause (100 hPa). ~~This figure links average~~

CWCs with paired ranges of heating rate and RH, along with differences in occurrence frequency between the largest (Q4) and smallest (Q1)values of LWCRE.The TTL is located above the typical levels of convective detrainment (200∼300 hPa; Fig. 4), with a lower boundary near the LZRH (140∼150 hPa; Fig. 9A). Clouds in this layer are often associated with slow radiatively-balanced ascent, and occasionally with very deep convection that penetrates into the TTL (e.g. Fueglistaler et al., 2009) . These two cloud populations may be distinguished by their CWCs (smaller for in situ cirrus; larger for convective anvil clouds) and associated radiative heating rates (weak radiative heating for slow ascent; strong cloud-top cooling for most anvil clouds, possibly supplanted by strong warming for clouds reaching very high altitude). The essential radiative signature of cloud-top cooling and cloud-base warming can be seen by comparing the radiative heating profiles in Fig. 8A–E and the vertical locations of the anvil cloud layers in Fig. 4F. Radiative heating thus helps to distinguish different types of clouds in the lower part of the TTL: (1) in situ cirrus clouds, which are associated with weak positive heating rates balancing large-scale ascent (i.e. close to the 'spine' of the plot); (2) deep convection that detrains near the base of the TTL, which is associated with large CWCs and negative radiative heating (the left 'wing'); and (3) deep convection that detrains inside the TTL, which is associated with large CWCs and positive heating rates (the right 'wing'). The latter two types are distinguished by both the depth and water content of the anvil cloud (Fig. 13), and the third type grows increasingly rare with increasing altitude. Compositing on RH in addition to radiative heating helps to highlight some differences and unrealistic features among the reanalyses, as discussed below.

At 150 hPa, the distributions based on ERA5 (Fig. 12F) and MERRA-2 (Fig. 12I) show striking similarities, with 'wings ' wings of large CWCs at large positive and negative negative and large positive radiative heating rates bracketing a central axis in which radiative heating is weak and CWC depends mainly on RH. The largest values of LWCRE are mainly associated with strong radiative cooling at 150 hPa (the left wing), while strong radiative heating (the right wing) is more often associated with Q2 or Q3 rather than Q4(not shown). This difference is consistent with composite mean profiles of CWC , as (Fig. 13): large negative heating rates at this level 150 hPa are associated with lower and more extensive anvils than shallower anvils and larger CWCs, while large positive heating rates (Fig. 13; see also Fig. 8). The two wings may thus represent the different radiative impacts of growing versus mature convective systems, and specifically the more extensive anvil clouds associated with the latter (Machado et al., 1998). are associated with deeper anvils and smaller CWCs. The distribution based on JRA-55 (Fig. 12H) is similar to those based on ERA5 and MERRA-2 but with a much smaller range of radiative heating rates, consistent with less extensive anvil clouds and smaller water paths in this reanalysis smaller anvil water contents (Fig. 4C). The distribution based on CFSR also shows similar features(Fig. 12J) also shows similarities, but with additional variance in radiative heating that results from linked to the occasional occurrence of very large daily mean extremely large daily-mean CWCs (up to 1408 mg kg^{-1}) at this level. Approximately 1% of daily mean CWCs at 150 hPa in CFSR exceed 100 mg kg^{-1}, far more than in the other reanalyses any other reanalysis (maximum: 0.1% in ERA5). The distribution based on ERA-Interim distribution (Fig. 12G) is more distinctive, with CWC (and LWCRE) more tightly linked to RH and an asymmetry toward positive heating rates. ERA-Interim produces very few instances of large negative heating rates, as cloud effects tend to increase clouds are associated with enhanced radiative heating at 150 hPa in this reanalysis (Fig. 8).

At 100 hPa, ERA5 and ERA-Interim (Fig. 12A–B) show similar distributions of composite mean CWC, with larger values concentrated in regions of as the largest values are associated with positive radiative heating and supersaturation with respect to

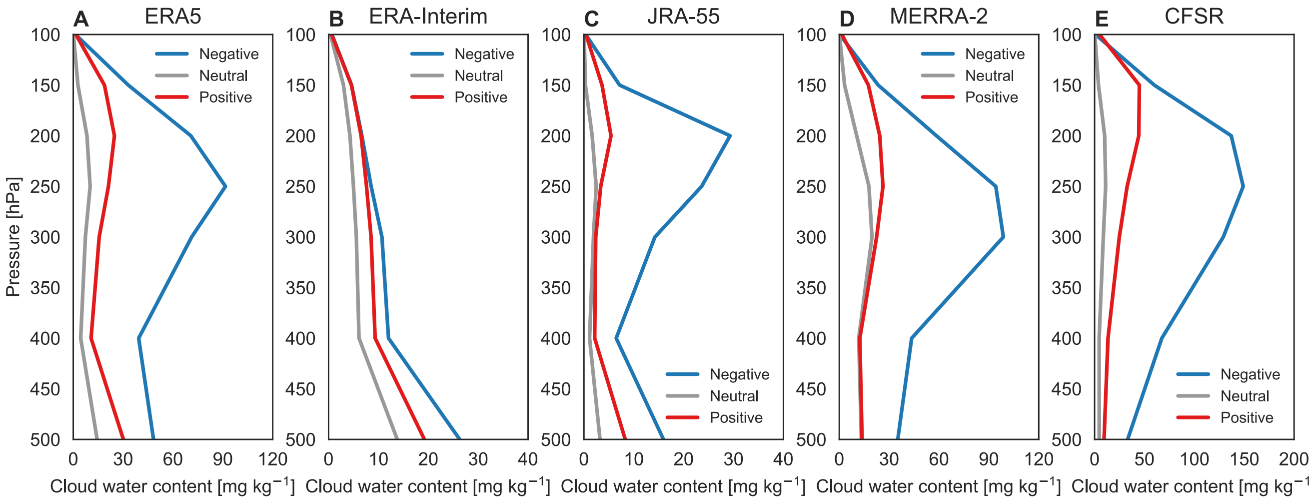

Figure 13. Composite mean profiles of cloud water content (CWC) from (A) ERA5, (B) ERA-Interim, (C) JRA-55, (D) MERRA-2, and (E) CFSR associated with different ranges of radiative heating rates at 150 hPa: negative rates less than $-1\,\mathrm{K\,d^{-1}}$ (blue), neutral rates within $\pm 1\,\mathrm{K\,d^{-1}}$ (grey), and positive rates greater than $+1\,\mathrm{K\,d^{-1}}$ (red). Note different x axis ranges for CWC.

ice. However, these two systems show ~~opposite~~ different relationships with LWCRE. Whereas large values of LWCRE ~~are more commonly associated with~~ often correspond to positive heating rates at ~~this level~~ 100 hPa in ERA-Interim, the largest values of LWCRE ~~are mainly associated with~~ typically correspond to negative heating rates at this level in ERA5. ERA5 and ERA-Interim are the only models considered here that explicitly consider supersaturation with respect to ice. Figure 12~~indicates that preferred locations of in situ cloud formation near the tropopause may differ between these two reanalyses because convective clouds influence radiative heating differently~~ A–B indicates that, owing to different radiative signatures of deep convection within the TTL~~(see also Fig. 8A, B). The distribution in JRA-55 (Fig. 12C) also shows a peak in composite-mean CWC associated with high RH and positive heating rates, along with a secondary peak at high RH and weak negative heating rates.~~, in situ cirrus clouds form preferentially above strong convective regions in ERA-Interim but outside of these regions in ERA5. The distribution based on MERRA-2 ~~likewise has a bimodal structure~~ is also bimodal (Fig. 12D), but in this reanalysis the most prominent mode ~~evokes the wing-like structure at 150 hPa. This mode features~~ is a leftward-facing wing with relatively large CWCs, negative radiative heating rates, and large LWCREs~~, and is thus consistent with anvil clouds that penetrate to~~. This mode is consistent with cooling at the tops of anvil clouds near the tropical tropopause. The second mode features positive radiative heating rates and saturation with respect to ice, and is thus consistent with expectations for ~~high clouds with small water contents that form~~ thin high clouds near the tropopause ~~(Fusina et al., 2007). Indeed, with~~ (e.g. Fusina et al., 2007).

With the exception of ERA-Interim, the largest CWCs at 100 hPa are associated with very large water paths through the UTLS and large negative radiative heating at 100 hPa. The smallest CWCs at 100 hPa ~~are associated with~~ correspond to near-zero radiative heating~~rates~~. Mean CWCs associated with positive radiative heating ($> +0.5\,\mathrm{K\,d^{-1}}$) are significantly larger, but still ~~at least 1–2 orders of magnitude~~ more than a factor ten smaller than those associated with ~~large~~ strong negative radiative heating~~rates. Taking large~~. Taking strong negative radiative heating ($< -0.5\,\mathrm{K\,d^{-1}}$) and large CWCs ($> 10\,\mathrm{mg\,kg^{-1}}$) at 100 hPa as a crude indicator of overshooting convection ~~reaching~~ that reaches the tropopause, these events occur around 0.2% of the time in MERRA-2 and 0.1% of the time in CFSR and ERA5. These criteria are never met in JRA-55 or ERA-Interim. Conversely, taking large positive radiative heating ($> +0.5\,\mathrm{K\,d^{-1}}$) and above-average CWCs ($> 0.01\,\mathrm{mg\,kg^{-1}}$) as indicative of ~~thin~~ in situ cirrus in air rising through the TTL, this regime covers 35% of the tropics in ERA-Interim, 24% in JRA-55, and ~~9–11~~around 10% in ERA5, MERRA-2, and CFSR.

The distribution based on CFSR at 100 hPa (Fig. 12E) indicates severe problems with humidity fields around the tropopause. Values of RH in CFSR at this level cluster around three values: zero (7% of samples), saturation with respect to ice (6%~~of samples~~), and saturation with respect to liquid water (77%~~of samples~~). Values between zero and saturation with respect to ice account for the remaining 10% of samples. ~~Relatively large values of CWC are found throughout the range of RH at 100 hPa.~~ Saturation with respect to liquid water ~~in CFSR~~ occurs occasionally at 150 hPa in CFSR as well (Fig. 12J), although these instances differ from those at 100 hPa in that they are associated mainly with small values of LWCRE and negligible CWCs, and only represent a small fraction of samples (1.5%). Humidity fields in the stratosphere are ~~known to be~~ unrealistically small in ~~this reanalysis (Davis et al., 2017). Figure~~CFSR (Davis et al., 2017); Fig. 12 shows that ~~this unrealistic behavior~~ unrealistic behaviour often extends downward into the TTL. In Appendix B, we show that the situation is much improved in CFSv2.

Although MERRA-2 contains no explicit representation of ~~supersaturation with respect to ice~~ ice supersaturation, RH in this reanalysis exceeds ~~the saturation threshold~~ saturation with respect to ice ~~for~~ in around 33% of gridded daily means at 150 hPa and 20% of gridded daily means at 100 hPa. This decrease with height differs from the parameterized behaviour in ERA-Interim and ERA5, in which daily-mean supersaturation frequencies increase from 15–25% at 150 hPa to 30–40% at 100 hPa. The occurrence of ice supersaturation in MERRA-2 can result from the partitioning of liquid and ice and subsequent gradual relaxation of liquid condensate to ice as implemented in the model's prognostic cloud scheme (Appendix A1), but it is surprising that it remains so prevalent in the TTL. This feature may ~~be explained by~~ result from temporal truncation: the model limits the water ~~vapor~~ vapour content at grid-scale saturation, the temperature is then modified by some other process, and output is written without further adjustment to the water ~~vapor~~ vapour field. All of the supersaturated points in MERRA-2 have non-zero CWCs, and CWC tends to increase with increasing supersaturation ($r = 0.24$). Liquid water is present in trace amounts for almost all supersaturated points at 150 hPa (93%) and a ~~large~~ substantial fraction of supersaturated points at 100 hPa (31%). This persistence of positive liquid water contents at very low temperatures will be addressed in a forthcoming version of the GEOS-5 model.

6 Temporal variability

Figure 14 shows deseasonalized monthly anomalies for ~~high cloud cover, OLR,~~ HCC, all-sky OLR, clear-sky OLR, and LWCRE in the inner tropics (10°S–10°N) based on the five reanalyses and CERES-based data sets (CERES SYN1Deg for ~~high cloud cover~~HCC; CERES EBAF for OLR and LWCRE). Anomalies are calculated relative to the mean annual cycle over all full years in the CERES overlap period (2001–2014). Most of the reanalyses produce temporary increases in high-cloud fraction and LWCRE (and corresponding decreases in OLR) around the major El Niño events of 1982–83 and 1997–98, although the timing, amplitude, and duration of these excursions varies. However, the most pronounced variations appear to be systemic rather than physical.artificial.Most notably, the tropical-mean high cloud fraction HCC in CFSR jumped suddenly by more than 0.1 between the end of 2009, when CFSR was initially planned to end, and the beginning of 2010. Tropical-mean high cloud fraction then increased HCC then jumped again at the beginning of 2011 with the transition to CFSv2, to a value very close to that in MERRA-2 (not shown). The bridge year 2010 is not well documented, but has been shown to feature discontinuities in other variables as well (e.g. stratospheric water vapor; Davis et al., 2017). Sudden jumps (e.g. stratospheric water vapour; Davis et al., 2017). Abrupt changes in the CFSR time series are not limited solely to the CFSR/CFSv2 CFSR–CFSv2 transition, with transient reductions in tropical-mean high cloud fraction HCC after every production stream transition in the initial 1979–2009 run (1 January 1987, 1990, and 1995; 1 April 1999 and 2005 Saha et al., 2010; Fujiwara et al., 2017). However, whereas these latter stream-related discontinuities are also evident seen in OLR and LWCRE (as is the transition at the beginning of 2010), neither OLR nor LWCRE shows large sudden changes following the transition to CFSv2 in January 2011. Despite suggestions that CFSv2 can serve as an extension of CFSR, researchers should be cautious in adopting this approach for any study that spans studies that span the 2010 bridge year or the 2011 transition to CFSv2. Further discussion of the CFSR–CFSv2 transition is provided in Appendix B.

In addition to the production stream transitions in CFSR/CFSv2, several of the anomaly time series show long-term drifts. To assess whether the consistency of these long-term changes are consistent across data sets, we evaluate trends over the 1980–2014 and 2001–2014 periods (Fig. 14D–E).Trends and confidence intervals are calculated using the robust Theil–Sen estimator (Sen, 1968). Note that even where trends are statistically significant, the their signs and magnitudes of these trends are subject to uncertainties associated with data processing and changes in the observing system over time. These caveats apply not only to reanalyses, but also to observationally-based analyses (like the ISCCP and CERES cloud products; e.g. Dai et al., 2006) and derived products that depend on these analyses (like the SRB and CERES radiation products; e.g. Trenberth et al., 2009) . The trend values shown here are (like the SRB and CERES clear-sky radiation products; e.g. Trenberth et al., 2009). Trends are shown here for intercomparison purposes, without assessment of their realism or reliability.

Over the full record, JRA-55 shows the most obvious and temporally consistent increase in high cloud fractionHCC, along with corresponding changes in OLR (towards smaller values) and LWCRE (towards larger values). These changes bring JRA-55 closer to the other reanalysesby the later part of the record, although absolute biases in tropical-mean OLR relative to ERA-Interim and CFSR/CFSv2 remain on the order of $10\,\mathrm{W\,m^{-2}}$ over 2010–2014 (as opposed to $\sim 15\,\mathrm{W\,m^{-2}}$ in the early 1980s). Most of the other reanalyses show qualitatively similar trends in high cloud fraction HCC (increasing), OLR (decreasing), and LWCRE (increasing) over 1980–2014, although but with magnitudes smaller than those based on JRA-55. Decreasing trends in clear-sky OLR are qualitatively robust, except for the 1980–2014 trend in MERRA-2. Decreasing trends in clear-sky OLR suggest that increases in atmospheric greenhouse gas absorption outpace increases in the effective emission temperature in the tropics over this period, changes that which may be explained by the so-called ‘hiatus’ in surface warming during the early 2000s (Song et al., 2016). Prescribed greenhouse gas concentrations in the reanalyses increased throughout this

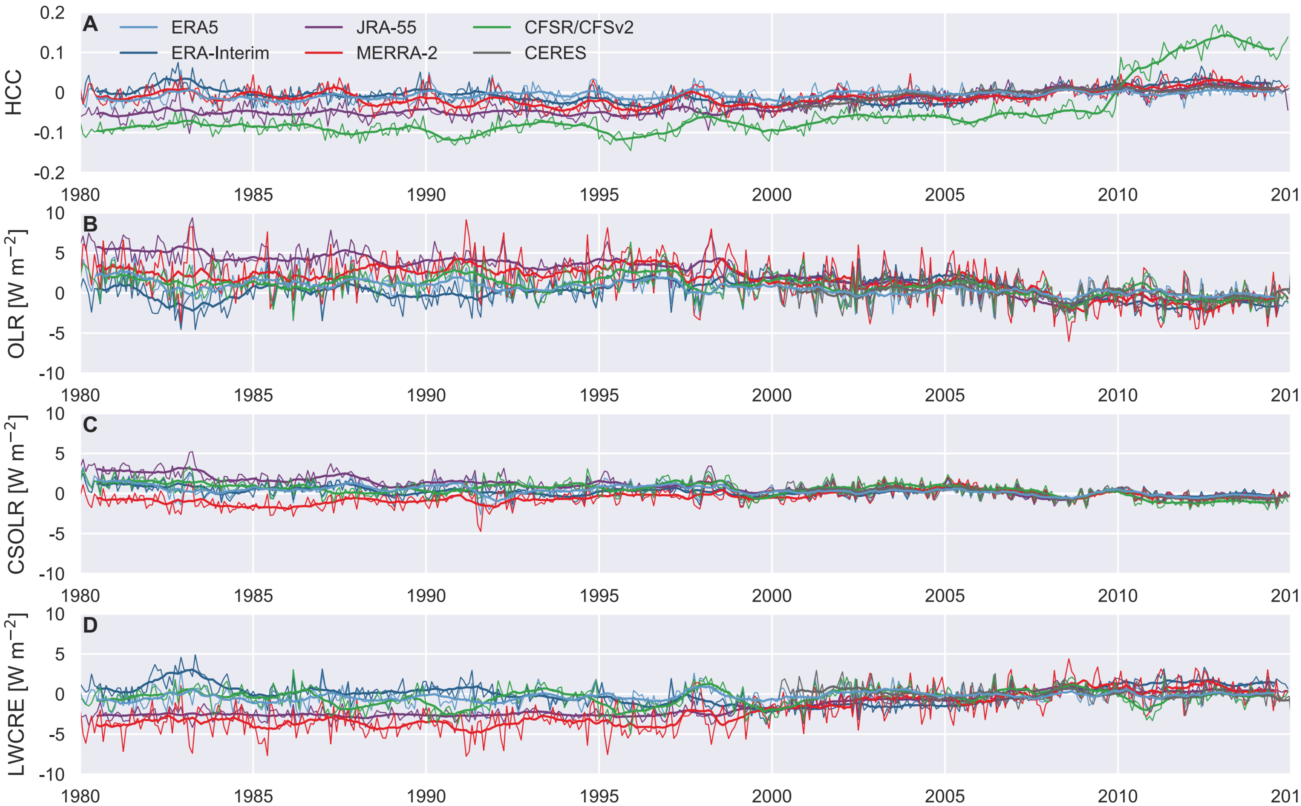

E Trends (1980–2014)

	ERA5	ERA-I	JRA-55	MRR-2	CFSR/v2	CFSR 1980-2009	SRB 1984-2007	NOAA	ISCCP 1984-2014
HCC	**** +0.5	+0.1	**** +2.3	* +0.7	**** +2.3	**** +1.3			** –0.7
OLR	**** –0.56	–0.07	**** –2.06	**** –1.23	**** –0.68	**** –0.55	* +0.46	+0.14	
CSOLR	**** –0.34	**** –0.29	**** –0.90	**** +0.38	**** –0.49	* –0.26	**** –1.15		
LWCRE	**** +0.22	–0.23	**** +1.1	**** +1.60	+0.15	* +0.28	**** –1.57		

F Trends (2001–2014)

	ERA5	ERA-I	JRA-55	MRR-2	CFSR/v2	CFSR 2001-2009	CERES	ISCCP/ NOAA	MODIS
HCC	+0.2	**** +5.0	**** +2.5	**** +3.4	**** +16.6	+1.9	**** +2.3	–0.7	–0.3
OLR	–0.41	**** –3.30	**** –1.97	*** –2.19	**** –1.51	–1.58	–0.73	–1.17	
CSOLR	** –0.56	–0.34	** –0.85	** –0.90	**** –1.93	–1.60	*** –0.94		
LWCRE	–0.07	**** +2.96	**** +1.17	*** +1.47	–0.48	+0.56	–0.43		

Figure 14. Time series of deseasonalized anomalies in ~~(A)~~ monthly mean ~~high cloud cover~~ (~~HCC~~A) HCC, (B) ~~monthly mean~~ all-sky OLR, ~~and~~ (C) ~~monthly mean~~ clear-sky OLR, and (D) LWCRE averaged over the inner tropics (10°S–10°N) for 1980–2014 based on ERA5 (cyan), ERA-Interim (blue), JRA-55 (purple), MERRA-2 (red), and CFSR/CFSv2 (green). Observational analyses from CERES SYN1Deg (A; March 2000–December 2014) and CERES EBAF (B and C; March 2000–December 2014) are shown for context. Anomalies are calculated relative to the mean annual cycle during 2001–2014. Thick lines show time series after applying a 12-month uniformly-weighted rolling mean. Trends are listed for annual-mean anomalies during the (~~D~~E) 1980–2014 and (~~E~~F) 2001–2014 periods in percentage points per decade for HCC and units of W m^{-2} per decade for OLR, clear-sky OLR, and LWCRE. Stars indicate statistical significance at the 90% (*), 95% (**), 99% (***), and 99.5% (****) confidence levels. Light grey shading indicates that the 90% confidence interval of the Theil–Sen slope (Sen, 1968) contains zero. Blue ~~colors~~ colours mark negative trends and red ~~colors~~ colours positive trends, with darker shades signifying larger trend magnitudes (0 to 1, 1 to 2, 2 to 3, and greater than 3).

period (Fujiwara et al., 2017, their Fig. 4), even as observed surface temperatures cooled or stayed roughly constant through much of the tropics~~for more than a decade~~ (e.g. Kosaka and Xie, 2013). Although these trends should be interpreted with care, their consistency with expectations is a promising sign for the use of broadband OLR fluxes in climate monitoring, given the potential for compensating effects to damp signals of climate change in these fields (e.g. Huang and Ramaswamy, 2009).

Most of the reanalyses also suggest decreasing trends in all-sky OLR over this period, although the signs (over 1980–2014) and magnitudes (over 2001–2014) of these trends are not supported by observations. Associated declines in upwelling LW radiation at the tropopause may help to explain long-term decreases in tropical cold point temperatures based on JRA-55, MERRA-2, and CFSR ~~(Tegtmeier et al., 2020). With the~~ (Tegtmeier et al., 2020). Decreasing trends in all-sky OLR seem at first glance to contradict the fixed anvil temperature hypothesis of Hartmann and Larson (2002). However, increasing trends in HCC are qualitatively consistent with decreases in all-sky OLR above and beyond those in clear-sky OLR; reductions in all-sky OLR therefore do not necessarily imply reductions in anvil cloud emission temperatures. Indeed, with the exception of CFSR/CFSv2 (affected by discontinuities around the CFSR–CFSv2 transition as discussed ~~above~~in Appendix B) and ERA5 (for which trends are small), relatively large decreasing trends in all-sky OLR among reanalyses reflect relatively large increases in LWCRE, which are linked in turn to increases in ~~high cloud fraction~~HCC. The increases in LWCRE and ~~high cloud cover~~ HCC implied by reanalyses are generally not supported by the observationally-based time series; however, discrepancies in ~~high cloud cover~~ HCC trends among CERES (positive), ISCCP (negative), and MODIS (no significant trend) reveal endemic uncertainty regarding whether and in what direction this variable changed. Long-term trends over 1980–2014 are small in both ERA5 and ERA-Interim. This picture changes considerably in the later part of the record, ~~over~~ for which trends in ERA5 remain small but trends in ERA-Interim are among the largest across all data sets. For ERA-Interim, weak long-term trends thus reflect relatively large excursions in these variables in the early 1980s acting to offset relatively large changes in the same direction after the turn of the century. These early-1980s excursions have also been reported for TTL temperatures based on ERA-Interim (Tegtmeier et al., 2020).

Figure 15 summarizes paired correlations and normalized standard deviations among the five reanalyses and available observation-based benchmarks. Monthly anomalies and evaluation metrics are calculated for the longest overlapping period common to both datasets (CERES: 2001–2014; ISCCP/SRB: 1984–2007; CFSR: 1980–2009; all other reanalyses: 1980–2014). For CFSR we truncate the time series after 2009 to avoid the 2010 bridge year and the CFSR–CFSv2 transition. Extending the time series through 2014 reduces the correlations and increases the normalized standard deviations. Two sets of summary results are provided, one for the tropics as a whole (30°S–30°N; Fig. 15A–C) and one for the inner tropics (10°S–10°N; Fig. 15D–F). Correlations and standard deviations are calculated first for data on a common 2.5°×2.5° latitude–longitude grid and then averaged for the corresponding region.

Among the reanalyses, monthly anomalies based on ERA5 consistently show the highest correlations against observational benchmarks for all metrics (~~high cloud cover~~HCC, OLR, and LWCRE), regions (full tropics and inner tropics), and analysis periods (1984–2007 for ISCCP/SRB and 2001-2014 for CERES). By contrast, MERRA-2 shows relatively poor correlations for ~~high cloud cover~~HCC, especially in the inner tropics. Correlations for ~~high cloud cover~~ HCC relative to CERES are larger than those relative to ISCCP for all five reanalyses. Although this difference is also found for CERES versus SRB with respect

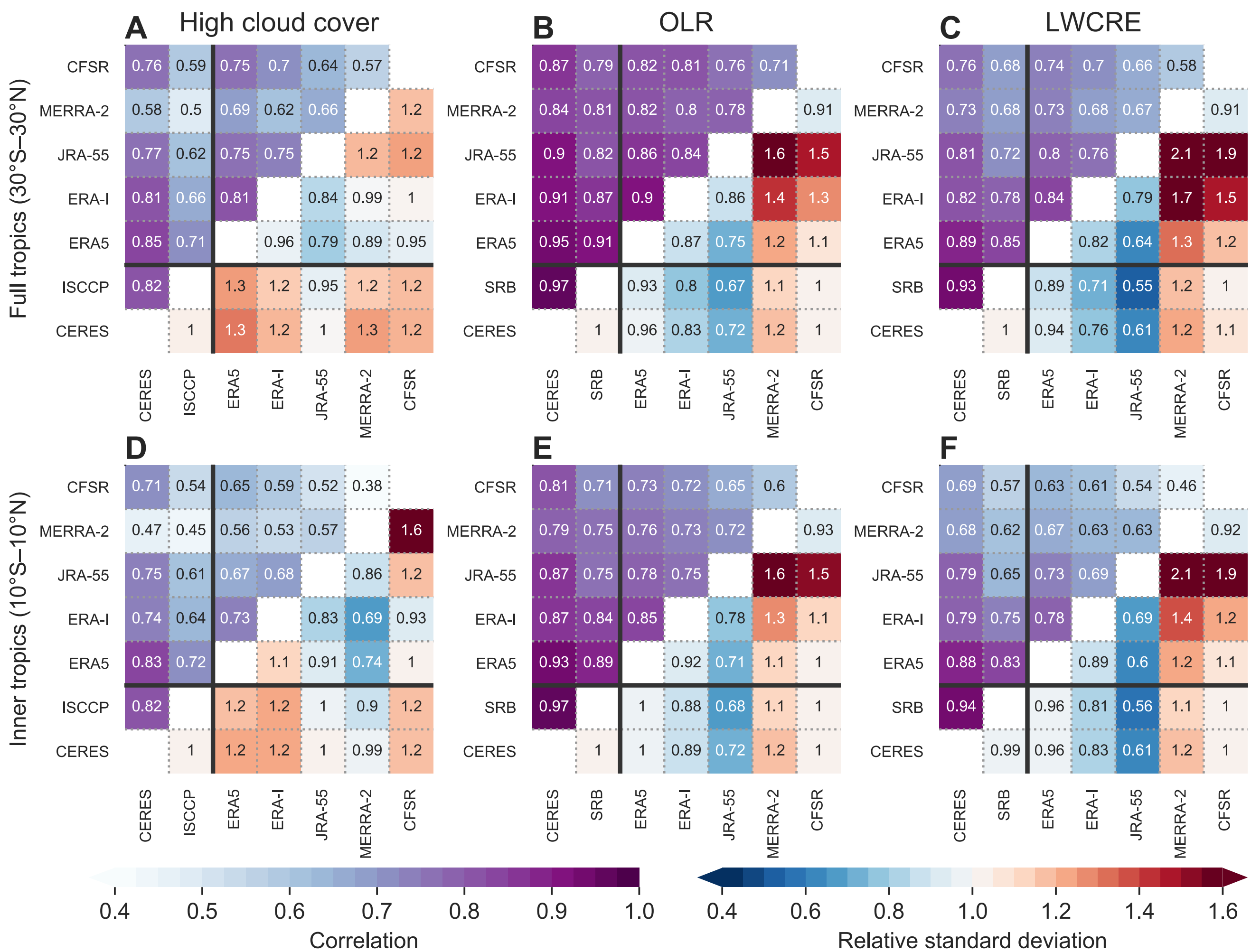

Figure 15. Metrics measuring agreement in monthly anomalies of (A, D) ~~high cloud fraction~~HCC, (B, E) ~~outgoing longwave radiation~~OLR, and (C, F) the ~~longwave cloud radiative effect~~ LWCRE among the reanalyses and observational data sets examined in this paper. The upper left triangle in each panel shows correlation coefficients between each pair of products, while the lower right triangle shows the standard deviation in the product marked on the horizontal axis relative to that in the product marked on the vertical axis. Both metrics are evaluated first for individual grid cells in the 2.5° common grid (see, e.g., Fig. 1) and then averaged. The upper row (A–C) shows results for the entire tropics (30°S–30°N), while the lower row (D–F) shows results for the inner tropics only (10°S–10°N). Solid ~~grey~~ black lines separate evaluations relative to the observational benchmarks based on CERES, ISCCP, and NASA-GEWEX SRB from those based on intercomparison of reanalysis products.

to variability in OLR and LWCRE, the difference is less pronounced in these cases. Paired correlations for OLR and LWCRE almost all exceed 0.7, with only correlations against CFSR (complicated by the issues around production stream transitions) falling below 0.6.

Most of the reanalyses (except for JRA-55 in both regions and MERRA-2 in the inner tropics) show stronger variability in ~~high cloud fraction~~ HCC than indicated by CERES SYN1Deg or ISCCP D2. However, this may reflect shortcomings in the observational analyses, such as sampling biases or limited sensitivity to ~~thinner high~~ optically thin clouds. The smaller standard deviation in ~~high cloud cover~~ HCC in JRA-55 is likewise consistent with JRA-55 tending to underestimate ~~high cloud cover~~ HCC relative to the other reanalyses (Fig. 1E). Conversely, the results for MERRA-2, where variability is stronger than observed when averaged over the full tropics and weaker than observed when averaged over the inner tropics, may be associated with MERRA-2 producing ~~relatively~~ persistently large cloud fractions outside of the core convective regions (Fig. 1G). Results for variations in OLR and LWCRE are fairly robust, with JRA-55 consistently underestimating variability and MERRA-2 consistently overestimating variability relative to all other data sets. ERA-Interim also tends to underestimate variations in OLR and LWCRE relative to CERES or SRB~~, while standard~~ . Standard deviations based on ERA5 and CFSR are similar to observed.

7 Summary and outlook

We have presented and evaluated differences in tropical high clouds and their radiative impacts in five recent reanalyses: ERA5, ERA-Interim, JRA-55, MERRA-2, and CFSR. As a general rule, JRA-55 has less cloud water and smaller high cloud fractions than other reanalyses in the tropical upper troposphere ~~.~~ (Figs. 1, 3, 4). MERRA-2 represents the opposite bookend, with more cloud water and larger high cloud fractions. Accordingly, JRA-55 significantly overestimates OLR and underestimates the top-of-atmosphere LWCRE in the tropics relative to observations and other reanalyses, while MERRA-2 produces smaller values of OLR and larger values of the LWCRE, in better agreement with observations ~~.~~ (Figs. 5–7). Tropical-mean values from ERA-Interim and CFSR are similar to each other (and to the multi-reanalysis means) despite substantially different bias distributions. Relative to these two reanalyses, ERA5 produces slightly larger cloud fractions and smaller values of OLR.

Systematic differences in CWC translate into differences in radiative heating rates within the tropical upper troposphere and lower stratosphere (Fig. 8), with the largest CWCs (MERRA-2) corresponding to extensive disruption of the radiative heating profile and the smallest CWCs (ERA-Interim and JRA-55) corresponding to relatively weak effects. On one extreme, large CWCs in MERRA-2 result in a physically unreasonable time-mean zonal-mean layer of diabatic cooling in the tropics around 200 hPa (e.g. Tao et al., 2019, their Fig. D1). A similar layer in MERRA ~~is known~~ has been shown to cause problems with transport simulations in the TTL (e.g. Schoeberl et al., 2012). On the other extreme, the vertical distribution of CWC in ERA-Interim lacks the distinctive anvil layer found in observations and other reanalyses ~~.~~ (Fig. 4). As a result, only ERA-Interim among these five reanalyses indicates that cloud effects typically shift the LZRH toward lower altitudes ~~on average.~~(Fig. 9A). All other reanalyses indicate upward shifts, with the largest shift in MERRA-2. It is worth noting that an upward shift ~~runs counter to~~ contradicts results based on applying radiative transfer models to observed cloud distributions, which indicate that cloud effects lower the LZRH (Corti et al., 2005; Fueglistaler and Fu, 2006; Yang et al., 2010). This disagreement appears to arise from a combination of (1) the the reanalyses locating the peak positive shortwave effect being located at lower altitudes in the reanalyses and (2) and overestimating the negative longwave effectbeing much stronger in the reanalyses (Fig. 8; cf. Yang et al., 2010, their Fig. 10). The former suggests that the reanalyses may systematically underestimate the depth of convective anvil clouds, although this is not immediately evident in Figs. 3 or 4. For the latter, systematic underrepresentation of thin cirrus and /or their radiative effects within the TTL seems the most a likely explanation (Corti et al., 2005; Yang et al., 2010), especially as we represent cloud effects here in terms of the relative magnitude of the LWCRE.

Heating rates in the lower stratosphere are also impacted (Norton, 2001; Fueglistaler and Fu, 2006; Tao et al., 2019)by differences in high clouds (Fig. 9B; Norton, 2001; Fueglistaler and Fu, 2006; Tao et al., 2019). Large CWCs and a strong LWCRE, as in MERRA-2, correspond to weaker convergence of LW radiation in the lower stratosphere and hence smaller diabatic ascentrates (and hence weaker diabatic ascent) in the tropical lower stratosphere. Conversely, small CWCs and a weak LWCRE, as in JRA-55 or ERA-Interim, correspond to larger rates of stronger diabatic ascent in this region. At the nominal TOA, most of the reanalyses show substantial compensation between the LWCRE and SWCRE associated with thick high clouds, as the largest LWCREs are also associated with relatively large opposing SWCREs . (Figs. 6, 7). Exceptions are JRA-55, in which a weak LWCRE and a strong SWCRE result in a negative bias in the total CRE, and CFSR, in which a moderate LWCRE and a weak SWCRE result in a positive bias in the total CRE . Assuming equal in the inner tropics. The latter is compensated by negative biases in the subtropics (Fig. 6), yielding a net CRE in good agreement with CERES over the entire 30°S–30°N band but with much sharper horizontal gradients. As differences in clear-sky fluxes , these systematic differences are comparatively small, these differences in cloud effects translate to a net loss of energy by the tropical atmosphere in JRA-55 and a net gain of energy by the tropical atmosphere in CFSR relative to the other reanalyses. These radiative biases may in turn contribute to differences in other processes, such as horizontal energy advection, convective activity, or the effects of adjustments due to data assimilation. Many of the differences in high clouds and their radiative impacts can be traced back to assumptions and simplifications applied in the model convection schemes or in special treatments of detrained condensate in the prognostic cloud scheme. However, these differences also often the differences also involve feedbacks between parameterized cloud fields and the tropical environment that are not completely mitigated by assimilation of observational data into the reanalysis systemfully mitigated by observational data assimilation.

The reanalyses demonstrate a range of cloud behaviors behaviours near the tropical tropopause . (Figs. 12, 13). Further evaluation will be needed given the current lack of suitable observational constraintson these behaviorsobservational constraints, but values in CFSR are often unrealistic . Water vapor noticably unrealistic (Fig. 12E,J). Water vapour and cloud fields from CFSR should be avoided at these levels., although these issues appear to be improved in CFSv2 (Fig. B1). We have also reported evident discontinuities at production stream transitions in CFSR (Fig. 14), indicating that this data set should be used with caution, especially in analyses that span the 2010 bridge year and/or the 2011 transition to CFSv2 (see also Appendix B). Taking all factors into account (an absence of major drifts or jumps, consistently high correlations, and standard deviations quite close to those found in observationally-based analyses), ERA5 appears to provide a better representation of temporal variability in high cloud fractionHCC, OLR, and LWCRE within the tropics than other recent reanalyses. However, it is important to note that the current version of ERA5 contains known discontinuities in some variables in the early 2000s (e.g. temperature biases around and above the tropopause; Hersbach et al., 2018). ~~A replacement version~~ ERA5.1, a rerun covering the problematic period~~is intended~~ , has recently been released to address this issue.

We have highlighted several notable differences between ERA-Interim and ERA5 that may be of interest to users familiar with ERA-Interim. First, ERA5 produces more extensive cloud cover than ERA-Interim over continental convective regions in the tropics ~~.~~ (Fig. 1C,D). This difference has previously been reported to reduce brightness temperature biases in these regions (Bechtold et al., 2014). Second, the maximum cloud fraction in the tropical upper troposphere is shifted to lower altitudes in ERA5 ~~(∼175 hPa)~~ relative to ERA-Interim (~~∼150 hPa~~Fig. 3A,B). Comparison with observations does not clearly demonstrate which of these is more realistic ~~.~~ (Fig. 3F). Third, a pronounced anvil maximum in CWC is present in the tropical upper troposphere in ERA5 but not in ERA-Interim ~~.~~ (Fig. 4A,B). The distribution in ERA5 is more consistent with ~~observations of ice water content from CloudSat~~ , CloudSat observations CloudSat but still shows substantial discrepancies ~~.~~ (Fig. 4F). Fourth, as a consequence of the increased CWC in the upper troposphere, the ~~high~~ positive bias in OLR and ~~low~~ negative bias in LWCRE in ERA-Interim are both reduced in ERA5 ~~.~~ (Fig. 5). Distributions of the LWCRE, SWCRE, and total CRE based on ERA5 are more consistent with those inferred from CERES data ~~.~~ (Fig. 7). However, in both ERA5 and ERA-Interim, ~~the~~ low biases in LWCRE relative to CERES EBAF are twice as large in absolute magnitude as ~~the~~ high biases in OLR ~~, indicating that~~ because clear-sky OLR ~~may be underestimated in these reanalyses even as~~ is underestimated while all-sky OLR is overestimated. This may indicate issues with composition, emissivity, or other aspects of the LW radiation scheme in addition to clouds. We find the same ~~feature in CFSR~~behaviour in CFSR/CFSv2, which uses the same base model for LW radiative transfer as ERA5 and ERA-Interim (Appendix A3). Finally, cloud effects on radiative heating rates in the tropical upper troposphere, tropopause layer, and lower stratosphere are very different between ERA5 and ERA-Interim ~~.~~ (Fig. 8). Results for ERA5 are more in line with those found in other reanalyses (as noted above for the LZRH; Fig. 9), but should be further evaluated against independent data types (such as the CloudSat FLXHR-LIDAR product; L'Ecuyer et al., 2008).

Much of the information on the origins and impacts of biases in high clouds in this paper derives from relationships between cloud cover and other variables, including radiative exchange and the moist thermodynamic environment. Such comparisons not only help to reveal issues in the cloud parameterizations, but also highlight where and in what ways such issues may affect reanalysis variables more tightly constrained by the data assimilation, such as temperatures, winds, and humidities. The vertical profile of moist static energy (Fig. 11) is an instructive example. MSE is calculated solely using variables targeted ~~during~~ by data assimilation. However, our results reveal important differences in the vertical profile of MSE, especially in convective regions. Nor are these differences attributable solely to discrepancies in the water ~~vapor~~ vapour fields, as illustrated by the stabilizing effects of upper tropospheric warm biases in MERRA-2. Biases in upper tropospheric temperatures imply differences in the vertical location and spatiotemporal variability of isentropic surfaces as well. Such differences may impact the results of reanalysis-driven transport model simulations, regardless of whether those studies assume isentropic, diabatic, or kinematic representations of vertical motion. It is worth reiterating that we use the 'assimilated' (ASM) products from MERRA-2, which derive from the IAU corrector forecast, as opposed to the 'analyzed' (ANA) outputs, which derive from the 3D-FGAT analysis directly. The latter are expected to provide a closer match with the assimilated observations. However, in the case of MSE the ANA and ASM products are still in closer agreement with each other (figure not shown) than with AIRS or other reanalyses: both MERRA-2 products show large positive biases in the upper troposphere over convective regions~~, with comparable biases in the temperature, moisture, and geopotential components, respectively~~. We have focused on the ASM products in this intercomparison both because these variables are self-consistent with MERRA-2 cloud and radiation products and because NASA GMAO recommends the use of ASM products over ANA products in transport model simulations.

Several observationally-based data sets are used to establish context for the cloud fields. Such observationally-based analyses are limited by perspective, especially when clouds occur ~~into~~ in multiple overlapping layers, and the information that goes into them is neither homogeneous in space nor continuous in time. Both issues can be addressed to some extent, the former through the use of active remote sensing techniques such as lidar and radar (Stephens and Kummerow, 2007), and the latter through systematic analyses of imagery collected by the global network of geostationary satellites (Rossow and Schiffer, 1999), but no current observational platform addresses both simultaneously. Moreover, discrepancies among observationally-based estimates arising from differences in measurement capabilities and techniques remain ~~quite~~ large (e.g. Pincus et al., 2012; Stubenrauch et al., 2013)~~. Our results suggest that the range of variability among observational estimates of cloud fraction is~~ , and appear to be at least comparable in magnitude to ~~that~~ discrepancies among recent reanalyses ~~, suggesting that current observations may not by themselves constrain quantitative biases in reanalysis (or~~ (Fig. 3). Observational constraints on reanalysis (and other model-based) ~~products~~cloud fields therefore remain more qualitative than quantitative. Observation simulators can help, not least by enabling new sets of sensitivity tests (e.g. Stengel et al., 2018), but are still limited to the cloud populations that can be effectively observed by the observational platforms being emulated.

~~Beyond occasional references in the context of other variables, we have~~ We have largely neglected cloud top height and cloud top temperature in this intercomparison. The rationale for this omission is that the reanalyses do not typically provide these metrics directly ~~, so that~~ and they must be inferred by other means. However, systematic biases in cloud top ~~height~~ heights or temperatures may have implications for the magnitude and ~~spatial~~ distribution of cloud radiative effects. Such biases may also influence the spatiotemporal distribution of convective source regions ~~for~~ of air entering the stratosphere as inferred from transport model simulations. A systematic intercomparison of cloud top ~~height metrics based on consistent methodologies~~ heights and temperatures may be useful for revealing further deficiencies or idiosyncrasies of the convective parameterizations used in the reanalysis models~~, as well as~~ . Further investigation along these lines may also consider how these features ~~might imprint upon both~~ can imprint upon more widely-used reanalysis products and model simulations that use reanalysis fields to drive ~~transport within the atmosphere~~atmospheric transport.

Appendix A: Cloud and radiation parameterizations in the reanalyses

In this appendix, we briefly document selected aspects of the cloud, convection, and radiation parameterizations in the reanalysis atmospheric models. Additional information on the models, data assimilation schemes, and other elements of the reanalysis systems has been provided by Fujiwara et al. (2017) and in Chapter 2 of the forthcoming SPARC Reanalysis Intercomparison Project report (Wright et al., 2020, review version available at https://jonathonwright.github.io/S-RIPChapter2E.pdf).

A1 Prognostic cloud parameterizations

All reanalyses examined in this paper use prognostic parameterizations of large-scale clouds that consider two sources of high clouds: detrainment from deep convection and in situ condensation associated with large-scale vertical motion or diabatic cooling.

The evolution of high clouds in ERA-Interim is governed by the scheme outlined by Tiedtke (1993), in which a pair of equations are used to simultaneously track cloud water mass and cloud fraction accounting for transport, convective and large-scale source terms, as well as losses due to evaporation and precipitation. The scheme does not distinguish between liquid water and ice; rather, the ice-phase fraction is diagnosed as a quadratic function of temperature between 0°C (entirely liquid) and –23°C (entirely ice) at each time step (Fig. A1). The model also includes a parameterization to represent supersaturation with respect to ice at temperatures below –23°C. ERA5 uses an updated version of the same scheme. One of the most important changes is that both liquid and ice condensate are treated prognostically in ERA5, eliminating diagnostic partitioning between the two phases. The resulting behavior behaviour cannot be easily summarized in Fig. A1, but a comparison between the approach used in ERA5 and that used in ERA-Interim has been provided by Forbes et al. (2011, their Fig. 3). Clouds are assumed to be exclusively ice at temperatures below –40°C. Parameterized supersaturation with respect to ice applies at all temperatures below the freezing point in ERA5, rather than only at temperatures below –23°C as in ERA-Interim. JRA-55 uses a version of the approach suggested by Sommeria and Deardorff (1977) and modified by Smith (1990) to represent large-scale clouds at high altitudes. Cloud fraction depends on joint probability density functions (PDFs) of total water content and liquid water temperature , ($T_L = T - [L_v/c_p]q_c$, with q_c the cloud water content), assuming uniform distributions of subgrid fluctuations in both variables. Note that this formulation differs from the large-scale condensation scheme used to represent the evolution of marine stratocumulus, which follows Kawai and Inoue (2006). Partitioning between the ice and liquid phases is determined as a linear function of temperature between 0°C and –15°C (Fig. A1). Like JRA-55, MERRA-2 also uses a two-moment PDF-based approach to represent cloud cover and cloud water content, but with the total water PDF constrained as suggested by Molod (2012). Condensate formed in anvil clouds and condensate formed via large-scale saturation are tracked separately in the prognostic cloud scheme, with 'anvil' condensate gradually converted to 'large-scale' condensate (Bacmeister et al., 2006). New condensate is partitioned among the liquid and ice phases as a linear function of temperature between 0°C and –20°C (Fig. A1), with liquid condensate gradually converted to ice in the prognostic scheme when temperatures are less than 0°C. The approach used in MERRA is similar to that used in MERRA-2, but with a quartic function governing the partitioning of new condensate into liquid and ice (Fig. A1) and without the constraints on total water proposed by Molod (2012). In CFSR and CFSv2, cloud water content is parameterized using the formulation of Zhao and Carr (1997). Cloud fraction is then diagnosed following Xu and Randall (1996). Cloud water content is the primary determinant of cloud fraction, with RH a secondary contributor. The cloud scheme does not explicitly distinguish between liquid and ice. Condensate is assumed to be liquid for temperatures greater than 0°C and ice for temperatures less than –15°C (Fig. A1). At temperatures between these bounds, condensate is assumed to be liquid unless ice crystals already exist at or above the grid cell.

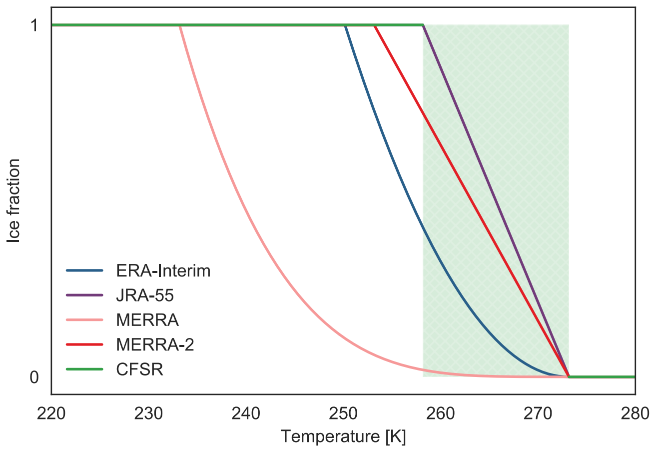

Figure A1. Fraction of new condensate in the ice phase as a function of temperature for ERA-Interim (blue), JRA-55 (purple), MERRA (light red), MERRA-2 (dark red), and CFSR (green). The green shaded region with hatching marks the range of temperatures for which new condensate in CFSR is assigned to the ice phase if ice already exists at or above the grid cell in question, and is assigned to the liquid phase otherwise.

All six reanalyses allow for evaporation and sublimation of condensed water and ice, along with losses of condensate due to autoconversion, accretion, and sedimentation. As with the parameterized formation of clouds, parameterizations of these loss processes differ amongst the reanalyses. For example, while all six reanalyses allow for condensate loss to ~~vapor~~ vapour when grid-scale RH falls below a critical threshold, only ERA5, ERA-Interim, MERRA, and MERRA-2 explicitly include representations of ‘cloud munching’ (evaporative loss due to turbulent mixing with clear air near the edges of the cloud; e.g. Del Genio et al., 1996). These parameterizations depend on the saturation specific humidity or ~~vapor~~ vapour pressure, and therefore have less effect for clouds at high altitudes (where temperatures are low) than for clouds at low altitudes. The ‘cloud munching’ parameterizations in MERRA and MERRA-2 apply only to anvil-type condensate detrained from deep convection. Implementations of the critical threshold for cloud evaporation are also influential. For example, lowering the critical threshold from saturation to the critical RH used for cloud formation contributes to increases in cloud residence times and re-evaporation of ice particles between MERRA and MERRA-2 (Molod et al., 2012).

A2 Parameterizations of deep convection

All ~~four~~ six reanalyses apply mass-flux representations of deep convection (e.g. Arakawa and Schubert, 1974; Tiedtke, 1989), but with substantially different treatments (Table A1). Mass-flux convective parameterizations represent the statistical effects of convection in a given grid cell via one or more updraft and downdraft plumes. Both updraft and downdraft plumes are then coupled to the background environment via entrainment and detrainment, diabatic heating, and the vertical transport of tracers and momentum. Differences in the convective parameterizations used by the reanalysis systems include the trigger function, the principal closure, whether and to what extent momentum and tracer transport are included, constraints on the properties of

Table A1. Summary information on deep convective parameterizations used in the reanalyses. Here CAPE is convective available potential energy, PCAPE is an entraining CAPE evaluated in pressure coordinates (Bechtold et al., 2014), LCL is the lifting condensation level, ABL is the atmospheric boundary layer, and A-S stands for Arakawa–Schubert.

Reanalysis	Plumes	Trigger	Closure	Cloud base	Detrainment
ERA5[a]	updraft: single downdraft: single	buoyancy > threshold Bechtold et al. (2006)	PCAPE + ABL coupling Bechtold et al. (2014)	LCL $\sim$lowest 350 hPa	above max ascent (RH dependence)
ERA-Interim[a]	updraft: single downdraft: single	buoyancy > threshold Bechtold et al. (2006)	CAPE-based Gregory et al. (2000)	LCL $\sim$lowest 350 hPa	above max ascent
JRA-55[b]	updraft: ensemble downdraft: single	dynamic CAPE Xie and Zhang (2000)	quasi-equilibrium	$p \sim 900$ hPa	$T < 0$°C
MERRA-2[c]	updraft: ensemble downdraft: ensemble	sub-cloud RH > 60%	quasi-equilibrium	ABL top	plume top
CFSR/CFSv2[d]	updraft: single downdraft: single	buoyancy > threshold Hong and Pan (1998)	quasi-equilibrium	LCL $\sim$lowest 300 hPa	plume top

[a] deep convection based on the scheme described by Tiedtke (1989).
[b] deep convection based on the 'economical prognostic' Arakawa–Schubert scheme described by JMA (2013).
[c] deep convection based on the 'relaxed' Arakawa–Schubert scheme described by Moorthi and Suárez (1992).
[d] deep convection based on the simplified Arakawa–Schubert scheme described by Pan and Wu (1995) and Moorthi et al. (2001).

the individual plumes (e.g. entrainment, detrainment, cloud base, and cloud top), and assumptions governing the production and partitioning of rainfall and cloud condensate.

ERA-Interim uses the scheme proposed by Tiedtke (1989), with a single pair of plumes representing updrafts and downdrafts. Deep convection is triggered when the updraft vertical velocity diagnosed at the lifting condensation level (LCL) is positive and the estimated cloud depth exceeds 200 hPa (Bechtold et al., 2006). Convection can be triggered from any level in the lowest 350 hPa of the atmosphere. Active convection consumes convective available potential energy (CAPE) over a specified time scale of 60 minutes. ERA5 uses the same core convection scheme as ERA-Interim (Table A1), but with several important modifications. The deep convective closure has been reformulated in terms of an effective CAPE where only a fraction of the daytime surface heating is available for deep convection and the remainder goes into turbulent and shallow convective mixing of the boundary-layer. This produces a more realistic diurnal cycle of convection over land, with maximum convective rainfall and heating occuring in the late afternoon as opposed to around noon in ERA-Interim (Bechtold et al., 2014). The convective adjustment time scale has also been set proportional to convective turnover, replacing the constant time scale for CAPE consumption used in ERA-Interim (Bechtold et al., 2008). JRA-55 uses the 'economical prognostic Arakawa–Schubert' scheme developed by the Japan Meteorological Administration (JMA, 2013). Convection is triggered using the 'dynamic CAPE' approach proposed by Xie and Zhang (2000), in which convection occurs when the time rate of change in CAPE due to large-scale forcing exceeds a critical value. Cloud base is restricted to the model level at $\sim$900 hPa. The convective closure is based on a modified version of the 'quasi-equilibrium' hypothesis, in which the generation of convective instability by the large-scale circulation is balanced by an ensemble of convective plumes that act to reduce the cloud work function below zero (Arakawa and Schubert, 1974). MERRA-2 uses the relaxed Arakawa–Schubert parameterization proposed

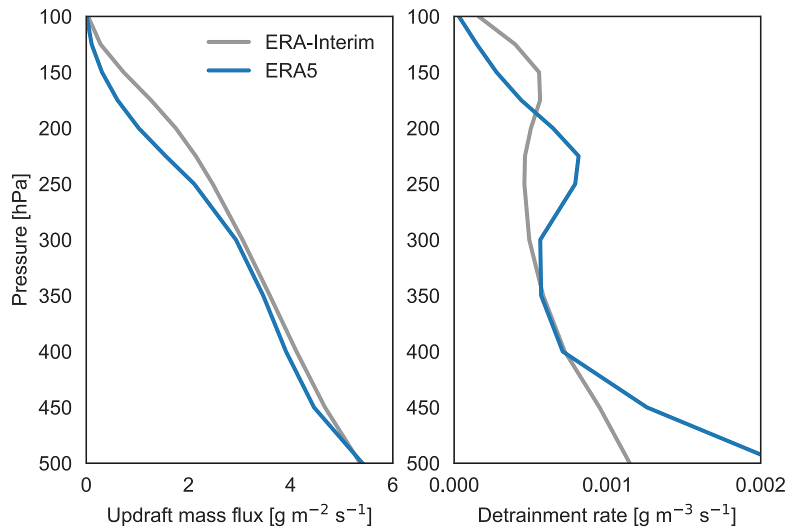

Figure A2. Vertical profiles of updraft mass fluxes and fractional detrainment rates in ERA5 (blue) and ERA-Interim (grey) for 10°S–10°N during January 2010.

by Moorthi and Suárez (1992). The convection scheme is triggered when the sub-cloud RH exceeds 60%. Convection is then represented via an ensemble of plumes with different ~~levels of entrainment~~ entrainment rates, subject to a Tokioka-type entrainment condition (Bacmeister and Stephens, 2011). The scheme randomly samples an empirically-based power-law distribution to set a minimum entrainment rate, disallowing any plume for which the diagnosed entrainment rate ~~falls below this level~~is less than this value. This triggering procedure means that MERRA-2 only occasionally permits the deepest convective clouds (Lim et al., 2015). Cloud base in MERRA-2 is defined as the top of the atmospheric boundary layer (ABL). A modified CAPE-based closure is used to determine mass flux for each plume at this cloud base. The ensemble of convective plumes acts to gradually relax the environment toward a specified equilibrium state. Convection in MERRA is similar, but without the stochastic trigger (potentially allowing more low-entrainment plumes with very high cloud tops) and with cloud base assigned to the lowest two model levels (rather than the boundary layer top). CFSR and CFSv2 use the simplified Arakawa–Schubert parameterization proposed by Pan and Wu (1995), updated as described by Moorthi et al. (2001). The convective trigger couples boundary layer turbulence and deep convection following the approach proposed by Hong and Pan (1998). Convection occurs when an air parcel corresponding to the maximum moist static energy (MSE) within the boundary layer would be positively buoyant at the LCL. Sub-grid variability associated with surface conditions, parameterized turbulent mixing in the boundary layer and lower free troposphere, grid-scale vertical velocity, and entrainment during ascent to the LCL are considered. The cloud base can be any level between the surface and 700 hPa, provided the trigger condition is met. Convective closure is based on the quasi-equilibrium hypothesis as in JRA-55.

Different treatments of entrainment into convective clouds and detrainment from convection into the large-scale cloud scheme also ~~have important impacts on the behaviors~~ influence the behaviours and distributions of high clouds in reanalyses.

ERA-Interim allows for turbulent exchange through the lower half of the convective column (equal entrainment and detrainment at fractional rates of $1.2 \times 10^{-4}\,\mathrm{m}^{-1}$), as well as organized entrainment below the level of maximum ascent and organized detrainment above this level. Organized entrainment is diagnosed as proportional to moisture convergence and organized detrainment according to decreases in upward mass flux assuming a constant cloud area. ERA5 includes several major changes to entrainment and detrainment (Bechtold et al., 2008). First, the dependence of organized entrainment on large-scale moisture convergence has been eliminated and replaced by a local approach where the bulk entrainment of positively buoyant plumes decreases with height according to the saturation specific humidity. The base entrainment rate at cloud base ~~of O($10^{-3}\,\mathrm{m}^{-1}$)~~ is also an order of magnitude larger than that in ERA-Interim and more in line with data from large-eddy simulations. This adjustment allows a unified treatment of the turbulent and organized components of entrainment. Second, RH-dependent factors have been introduced for both entrainment and detrainment. Outside of this new RH dependence the treatments of turbulent and organized detrainment are similar to those in ERA-Interim, but with a reduced turbulent detrainment rate ($0.75 \times 10^{-4}\,\mathrm{m}^{-1}$). Figure A2 shows that fractional detrainment rates in ERA5 are enhanced in both the middle (∼500 hPa) and upper (200∼300 hPa) troposphere relative to ERA-Interim, but reduced in the TTL (100∼150 hPa). This reflects ~~larger variability in the cloud field, with~~ a more realistic occurence frequency of cumulus congestus clouds and fewer quasi-undilute convective cores reaching the TTL relative to ERA-Interim. JRA-55 diagnoses entrainment rates for each deep convective plume based on a zero-buoyancy condition at cloud top, suppressing fractional entrainment rates greater than $1 \times 10^{-3}\,\mathrm{m}^{-1}$. Detrained cloud water is distributed among layers with temperatures below the freezing level according to a fixed, height-dependent relationship for partitioning rain and cloud water content. MERRA-2 specifies the cloud top for each updraft plume in the ensemble, with all model levels between $p = 100$ hPa and the level immediately above cloud base considered as candidates. Assuming that cloud top corresponds to the level of neutral buoyancy ~~(LNB)~~ for a candidate plume, the entrainment rate for that plume is then diagnosed based on conditions at the cloud base. Only plumes with diagnosed entrainment rates larger than the stochastically-determined minimum are triggered. In CFSR and CFSv2, the cloud top is randomly chosen from the set of levels between the level of minimum MSE and the ~~LNB~~level of neutral buoyancy. The base entrainment rate ($1 \times 10^{-3}\,\mathrm{m}^{-1}$) is then adjusted to achieve this randomly-chosen cloud top. Detrainment in both MERRA-2 and CFSR/CFSv2 occurs exclusively at the plume top. However, where MERRA-2 considers an ensemble of plumes with different entrainment rates, CFSR and CFSv2 use only a single pair of updraft/downdraft plumes.

A3 Parameterizations of radiative transfer

Details of the radiation parameterizations and their treatments of clouds are listed in Table A2. All of the parameterizations are broadband schemes, in which the radiative spectrum is discretized into a ~~discrete~~ predetermined set of spectral bands. The form of this discretization is dictated primarily by the presence of radiatively active constituents in the atmosphere and the wavelengths at which these constituents are active (e.g. Clough et al., 2005). Each band may feature parameterizations of radiative transfer due to multiple species, as well as scattering, absorption, and emission by clouds ~~or~~ and aerosols. Radiative fluxes and heating rates (~~defined as the~~ i.e. the vertical convergence of radiative fluxes) are computed by integrating across all spectral bands. ERA-Interim, JRA-55, MERRA-2, and CFSR (~~ending in~~ through 2010) all assume maximum–random

Table A2. Summary information on radiation parameterizations, cloud overlap, and cloud optical properties used in the reanalyses. In the column labeled 'Optical properties', L stands for liquid water clouds and I for ice clouds. Sources of cloud optical properties may differ between the LW and SW schemes.

	Radiation scheme		Cloud representations	
Reanalysis	Longwave	Shortwave	Overlap	Optical properties
ERA5	RRTMG-LW Iacono et al. (2008) 16 bands (3.08–1000 µm)	RRTMG-SW Iacono et al. (2008) 14 bands (0.2–12.195 µm)	McICA w/ generalized overlap	L_{SW}: Slingo (1989) L_{LW}: Lindner and Li (2000) I_{SW}: Fu (1996) I_{LW}: Fu et al. (1998)
ERA-Interim	RRTMG-LW Mlawer et al. (1997) 16 bands (3.33–1000 µm)	Fouquart and Bonnel (1980) 6 bands (0.2–4.0 µm)	max–random	L_{SW}: Fouquart (1988) L_{LW}: Smith and Shi (1992) I: Ebert and Curry (1992)
JRA-55	Murai et al. (2005) 11 bands (3.33–400 µm)	Briegleb (1992) Freidenreich and Ramaswamy (1999) 16 bands (0.174–5.0 µm)	max–random (LW) random (SW)	L_{SW}: Slingo (1989) L_{LW}: Hu and Stamnes (1993) I: Ebert and Curry (1992)
MERRA-2	CLIRAD-LW Chou et al. (2001) 11 bands (3.33–400 µm)	CLIRAD-SW Chou and Suárez (1999) 10 bands (0.175–10.0 µm)	max–random	L: Tsay et al. (1989) I_{SW}: Fu (1996) I_{LW}: Fu et al. (1998)
CFSR	RRTMG-LW Clough et al. (2005) 16 bands (3.08–1000 µm)	RRTMG-SW Clough et al. (2005) 14 bands (0.2–12.195 µm)	max–random	L: Hu and Stamnes (1993) I_{SW}: Fu (1996) I_{LW}: Fu et al. (1998)
CFSv2	RRTMG-LW Clough et al. (2005) 16 bands (3.08–1000 µm)	RRTMG-SW Clough et al. (2005) 14 bands (0.2–12.195 µm)	McICA w/ max–random overlap	L: Hu and Stamnes (1993) I_{SW}: Fu (1996) I_{LW}: Fu et al. (1998)

overlap for cloudy columns: cloud layers that are contiguous in the vertical are assumed to have maximal overlap and cloud layers that are not contiguous in the vertical coordinate are assumed to overlap randomly. The Monte Carlo Independent Column Approximation (McICA; Pincus et al., 2003) is used in ERA5 (with generalized overlap; Morcrette et al., 2008) and CFSv2 (with maximum–random overlap, starting from 2011; Saha et al., 2014). The introduction of McICA is therefore a potential source of discontinuity at the CFSR–CFSv2 transition. Representations of the optical properties of ice and liquid water clouds are also noted in Table A2.

Appendix B: The CFSR–CFSv2 transition

As documented in section 6, there is a sharp jump in HCC between the end of the original run of CFSR (December 2009) and the beginning of the CFSv2 extension (January 2011). Despite this sudden increase, changes in OLR and the LWCRE around this transition were relatively small. In this appendix, we provide additional information on changes in cloud and radiation products at the CFSR–CFSv2 transition that helps to clarify some but not all of the changes in clouds and radiation. Figure B1 shows differences in zonal-mean RH and CWC between the last four years of CFSR (2006–2009) and the first four years of CFSv2 (2011–2014), while Figure B2 shows horizontal distributions of HCC and OLR for the same periods. Figure B2D

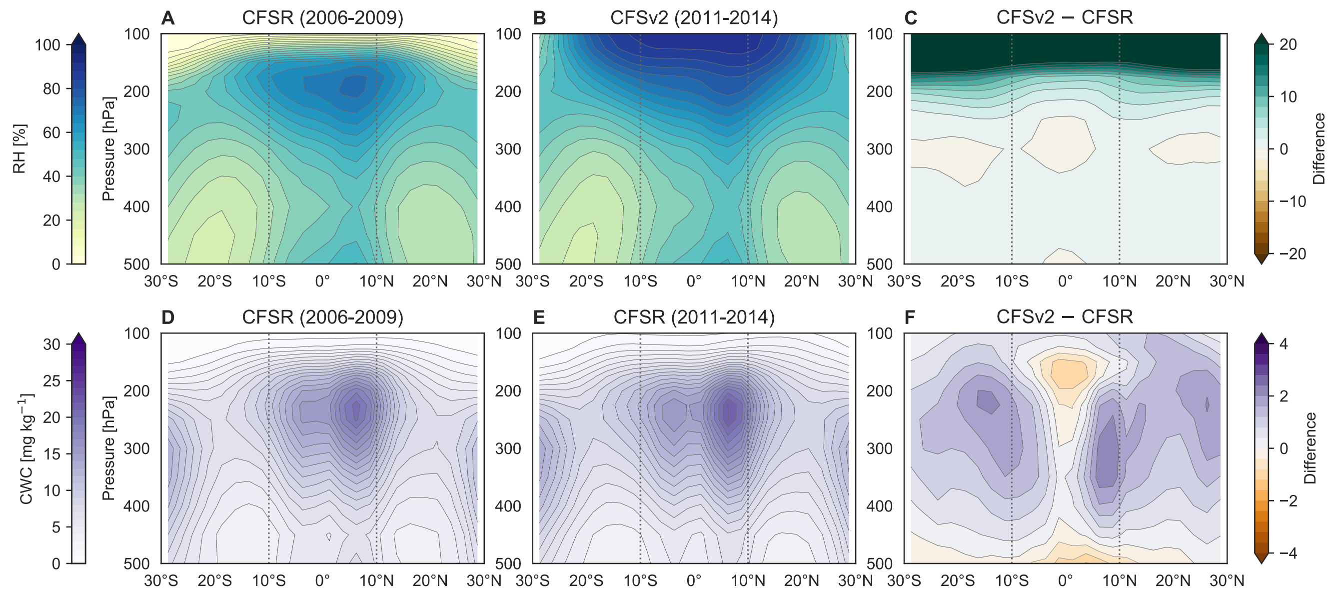

Figure B1. Upper row: Zonal-mean distributions of relative humidity based on (A) the last four years of the original CFSR (2006–2009) and (B) the first four years of CFSv2 (2011–2014), along with (C) differences between the two products. Lower row: as in the upper row, but for cloud water content.

shows changes in HCC based on ISCCP HGM for the 2011–2014 mean minus the 2006–2009 mean as an illustration of natural variability between these two periods, while Fig. B2H shows changes in upward SW radiation at the TOA to further illustrate differences between the two systems.

Relative humidities near the tropical tropopause are much larger in CFSv2 (Fig. B1B) than in CFSR (Fig. B1A). Whereas CFSR produced RH near zero at 100 hPa, conditions approach saturation at this level in CFSv2. The latter better matches observations in this part of the atmosphere (e.g. Fueglistaler et al., 2009), although the mean values are somewhat larger than expected. Consistent with this increase in humidity, values of CWC are enhanced in CFSv2 relative to CFSR near the tropopause. CWCs are also much larger in CFSv2 on the flanks of the tropics, but slightly reduced near the convective detrainment layer in the deep tropics. CFSR and CFSv2 do not provide vertical distributions of cloud fraction; however, the underlying models determine cloud fractions primarily as a function of CWC, with RH as a secondary factor (Appendix A1). Zonal-mean changes in the vertical distribution of cloud fraction should therefore be similar to those in CWC, with increases close to the tropopause and on the flanks of the tropics balanced against decreases in the inner tropics around 150–200 hPa. The spatial distribution of differences in cloud fraction between CFSR and CFSv2 (Fig. B2C) supports this view. In particular, the sudden jump in tropical-mean HCC seen in the time series (Fig. 14A) results primarily from large increases in cloud fraction outside of the core equatorial convective regions.

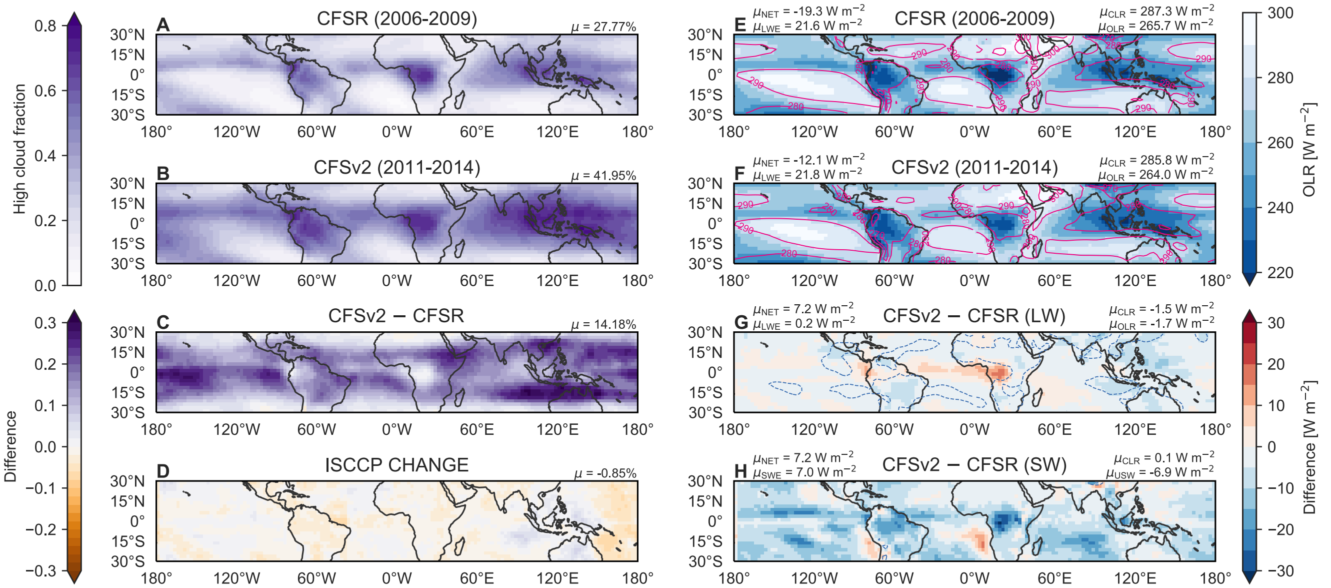

Figure B2. At left: distributions of high cloud fraction based on (A) the last four years of the original CFSR (2006–2009) and (B) the first four years of CFSv2 (2011–2014), along with (C) the difference between CFSv2 and CFSR. The change in ISCCP HGM high cloud fraction between the 2006–2009 mean and the 2011–2014 mean is shown for context in panel (D). At right: as in the left column, but for all-sky (shading) and clear-sky (contours) OLR, and with the change in all-sky upward SW flux between the 2006–2009 CFSR mean and the 2011–2014 CFSv2 mean shown in panel (H). Tropical mean (30°S–30°N) values of HCC (or ΔHCC) are listed at upper right of panels (A) through (D). Tropical mean values of the all-sky flux, clear-sky flux, CRE (LW or SW), and net CRE (or corresponding Δ values) are listed at upper right (all-sky and clear-sky flux) or upper left (CRE and net CRE) of panels (E) through (H).

Differences in OLR between CFSR and CFSv2 are shown in Fig. B2E–G. Although the small magnitude of changes in OLR involves some measure of compensation between different regions of the tropics (e.g. increases over Africa balanced by decreases over the western Pacific warm pool), it is clear that the changes in OLR do not match those in HCC. Indeed, the bulk of the change in OLR ($-1.7\,\mathrm{W\,m^{-2}}$) can be attributed to a decrease in the clear-sky OLR ($-1.5\,\mathrm{W\,m^{-2}}$), which may be contributed at least in part by the changes in TTL humidity (Fig. B1C). The transition to CFSv2 involved an increase in model horizontal resolution and changes in the radiation scheme (Saha et al., 2014; Fujiwara et al., 2017), including the adoption of McICA (Appendix A3). Model tuning conducted to re-establish TOA energy balance after these changes may have smoothed out the change in OLR that would otherwise have resulted from such a large jump in HCC. In this sense, it is interesting to note an increase of $7.2\,\mathrm{W\,m^{-2}}$ in the net CRE between the last four years of CFSR and the first four years of CFSv2. Given the near-zero change in the LWCRE ($0.2\,\mathrm{W\,m^{-2}}$), this implies a decrease of $7.0\,\mathrm{W\,m^{-2}}$ in the magnitude of the SWCRE (i.e. cloud albedo). This change in the SWCRE was undoubtedly also impacted by model changes aimed at marine low-level clouds (Saha et al., 2014). However, the spatial distribution of decreases in upward SW flux at the TOA (Fig. B2H) indicates that reductions in planetary albedo resulted more from differences in high clouds than differences in marine stratocumulus, as the latter seems to have produced regional increases in albedo.

It is perplexing that increases in HCC and upper-level CWC lead to an unchanged LWCRE and a reduced planetary albedo between CFSR and CFSv2, as increases in these cloud variables would typically be expecred to strengthen both the LWCRE and the planetary albedo. The flux balances match expectations internally for both CFSR and CFSv2; indeed, the net all-sky radiative flux is in good agreement with CERES EBAF (Fig. 6). It is only when we evaluate the changes at the transition that these inconsistencies crop up, implicating changes in the model. Precisely which changes to the model are responsible is unclear at present; however, both the existence of these discrepancies and the scale of the associated changes underscore our summary recommendation that users of CFSR/CFSv2 should approach any analysis spanning the transition with extreme care.

Data availability. ERA-Interim products were acquired from the public MARS archive maintained by ECMWF (http://apps.ecmwf.int/datasets) using the Python API (https://confluence.ecmwf.int/display/WEBAPI). Daily average heating rates and TOA fluxes were constructed from 12-h forecasts. Daily averages of all other data are from instantaneous 6-hourly products. ERA5 heating rates were also acquired from the ECMWF MARS archive using the Python API; all other ERA5 products were acquired from the Copernicus Climate Data Store (https://cds.climate.copernicus.eu). Due to bandwidth and storage limitations, vertically-resolved data from ERA5 were obtained at 3-hourly resolution, while two-dimensional data (cloud fractions, OLR) were obtained at the full hourly resolution. Daily average heating rates and TOA fluxes were constructed from time-averaged data while daily averages of all other variables were constructed from instantaneous outputs. JRA-55 heating rates were obtained from the NCAR Research Data Archive (RDA; https://rda.ucar.edu); all other JRA-55 products were obtained from archives maintained by the Japan Meteorological Agency (http://jra.kishou.go.jp/JRA-55). Daily means of heating rates and TOA fluxes were calculated from time-averaged diagnostic fields, while daily means of other variables were calculated from instantaneous outputs at the standard temporal resolution (6-hourly for vertically-resolved fields; 3-hourly for high cloud cover). CFSR and CFSv2 products were acquired exclusively through the NCAR RDA. Daily averages of heating rates and TOA fluxes were calculated from time-averaged forecast fields; daily averages of all other variables were calculated from 6-hourly instantaneous fields. MERRA and MERRA-2 products were obtained from the NASA Goddard Earth Sciences Data and Information Services Center (GES DISC; https://disc.gsfc.nasa.gov/daac-bin/FTPSubset2.pl). For MERRA we exclusively used monthly-mean IAU products. For MERRA-2 daily means we use the 3-hourly 3-hourly time-averaged heating rates and 3-hourly instantaneous profile fields, both from the IAU (ASM) product set. Hourly time-averaged fields were used for high cloud fraction and TOA radiative fluxes. Access dates for these products range from March 2015 to August 2019 depending on reanalysis, variable, and temporal resolution. ISCCP HGM products were acquired from the NOAA National Centers for Environmental Information (https://www.ncdc.noaa.gov/isccp; accessed 9 December 2019). CERES data were obtained from the NASA Langley Research Center Atmospheric Science Data Center, and AIRS data from the GES DISC; see related data citations for availability and access information. CloudSat–CALIPSO combined cloud fractions were provided by Jennifer Kay (personal communication, 15 December 2017), and CFMIP-GOCCP products by the Institute Pierre Simon Laplace (http://climserv.ipsl.polytechnique.fr/cfmip-obs/goccp_v3.html; v3.1.2 accessed 21 June 2018). CloudSat IWC retrievals were acquired from the CloudSat ftp server (ftp.cloudsat.cira.colostate.edu; CWC-RO R04 v5.1). NOAA Interpolated OLR data were acquired from the NOAA/OAR/ESRL Physical Science Division, Boulder, Colorado, USA (https://www.esrl.noaa.gov/psd; accessed 23 March 2017). The NASA GEWEX-SRB data were acquired from the NASA Langley Atmospheric Science Data Center (https://gewex-srb.larc.nasa.gov; v3.1 accessed 6 July 2019).

Author contributions. JSW and XS conducted the analysis and wrote the initial draft. XZ processed the CloudSat IWC data and helped to interpret the results. PK, KK, AM, ST, and GJZ suggested additional analyses and revisions for the manuscript. AM checked and clarified key aspects of MERRA-2.

Competing interests. The authors declare no competing interests.

Acknowledgements. This work was supported by the Ministry of Science and Technology of the People's Republic of China (2017YFA0603902) and a joint research project funded by the National Natural Science Foundation of China (NSFC project number 41761134097) and the German Research Foundation (DFG project number 392169209). We thank Peter Bechtold from ECMWF, Yayoi Harada and Ryoji Nagasawa from the JMA Meteorological Research Institute, and Kris Wargan from NASA GMAO for help in clarifying aspects of the reanalysis data, and Yi Huang and an anonymous reviewer for comments and suggestions that have greatly improved the manuscript. We are also grateful to Xianglei Huang for advice on OLR data and radiative transfer models~~and~~ , to Jennifer Kay for providing the CloudSat–CALIPSO data, and to Yi Qin and Xiaolu Yan for helpful discussions. A condensed version of this material has been prepared for Chapter 8 of the S-RIP report. We thank Masatomo Fujiwara, Gloria Manney, and Lesley Gray for their leadership of this activity, and all S-RIP participants for their contributions.

References

Abalos, M., Legras, B., Ploeger, F., and Randel, W. J.: Evaluating the advective Brewer-Dobson circulation in three reanalyses for the period 1979–2012, J. Geophys. Res. Atmos., 120, 7534–7554, https://doi.org/10.1002/2015JD023182, 2015.

Anber, U., Wang, S., and Sobel, A.: Response of atmospheric convection to vertical wind shear: Cloud-system-resolving simulations with parameterized large-scale circulation. Part II: Effect of interactive radiation, J. Atmos. Sci., 73, 199–209, https://doi.org/10.1175/JAS-D-15-0151.1, 2016.

Arakawa, A. and Schubert, W. H.: Interaction of a cumulus cloud ensemble with the large-scale environment, part I, J. Atmos. Sci., 31, 674–701, 1974.

Austin, R. T., Heymsfield, A. J., and Stephens, G. L.: Retrieval of ice cloud microphysical parameters using the CloudSat millimeter-wave radar and temperature, J. Geophys. Res. Atmos., 114, D00A23, https://doi.org/10.1029/2008JD010049, 2009.

Bacmeister, J. T. and Stephens, G. L.: Spatial statistics of likely convective clouds in CloudSat data, J. Geophys. Res. Atmos., 116, D04104, https://doi.org/10.1029/2010JD014444, 2011.

Bacmeister, J. T., Suárez, M. J., and Robertson, F. R.: Rain reevaporation, boundary layer–convection interactions, and Pacific rainfall patterns in an AGCM, J. Atmos. Sci., 63, 3383–3403, https://doi.org/10.1175/JAS3791.1, 2006.

Bannister, R. N., Chipilski, H. G., and Martinez-Alvarado, O.: Techniques and challenges in the assimilation of atmospheric water observations for numerical weather prediction towards convective scales, Q. J. Roy. Meteor. Soc., 146, 1–48, https://doi.org/10.1002/qj.3652, 2020.

Bechtold, P., Chaboureau, J.-P., Beljaars, A., Betts, A. K., Köhler, M., Miller, M., and Redelsperger, J.-L.: The simulation of the diurnal cycle of convective precipitation over land in a global model, Q. J. Roy. Meteor. Soc., 130, 3119–3137, https://doi.org/10.1256/qj.03.103, 2006.

Bechtold, P., Köhler, M., Jung, T., Doblas-Reyes, F., Leutbecher, M., Rodwell, M. J., Vitart, F., and Balsamo, G.: Advances in simulating atmospheric variability with the ECMWF model: From synoptic to decadal time-scales, Q. J. Roy. Meteor. Soc., 134, 1337–1351, https://doi.org/10.1002/qj.289, 2008.

Bechtold, P., Semane, N., Lopez, P., Chaboureau, J.-P., Beljaars, A., and Bormann, N.: Representing Equilibrium and Nonequilibrium Convection in Large-Scale Models, J. Atmos. Sci., 71, 734–753, https://doi.org/10.1175/JAS-D-13-0163.1, 2014.

Bloom, S. C.: Data assimilation using incremental analysis updates, Mon. Wea. Rev., 124, 1256–1271, 1996.

Bodas-Salcedo, A., Webb, M. J., Bony, S., Chepfer, H., Dufresne, J. L., Klein, S. A., Zhang, Y., Marchand, R., Haynes, J. M., and Pincus, R.: COSP: Satellite simulation software for model assessment, Bull. Am. Meteor. Soc., 92, 1023–1043, https://doi.org/10.1175/2011BAMS2856.1, 2015.

Bolton, D.: The computation of equivalent potential temperature, Mon. Wea. Rev., 108, 1046–1053, 1980.

Bony, S., Stevens, B., Frierson, D. M. W., Jakob, C., Kageyama, M., Pincus, R., Shepherd, T. G., Sherwood, S. C., Siebesma, A. P., Sobel, A. H., Watanabe, M., and Webb, M. J.: Clouds, circulation, and climate sensitivity, Nature Geosci., 8, 261–268, https://doi.org/10.1038/ngeo2398, 2015.

Briegleb, B. P.: Delta-Eddington approximation for solar radiation in the NCAR community climate model, J. Geophys. Res. Atmos., 97, 7603–7612, https://doi.org/10.1029/92JD00291, 1992.

Cao, G. and Zhang, G. J.: Role of vertical structure of convective heating in MJO simulation in NCAR CAM5.3, J. Climate, 30, 7423–7439, https://doi.org/10.1175/JCLI-D-16-0913.1, 2017.

Carr, M. T. and Bretherton, C. S.: Convective momentum transport over the tropical Pacific: Budget estimates, J. Atmos. Sci., 58, 1673–1693, 2001.

Chepfer, H., Bony, S., Winker, D., Cesana, G., Dufresne, J. L., Minnis, P., Stubenrauch, C. J., and Zeng, S.: The GCM-Oriented CALIPSO Cloud Product (CALIPSO-GOCCP), J. Geophys. Res. Atmos., 115, D00H16, https://doi.org/10.1029/2009JD012251, 2010.

Chou, M.-D. and Suárez, M.: A solar radiation parameterization for atmospheric studies, Technical Report Series on Global Modeling and Data Assimilation, No. 15, NASA/TM-1999-104606, Greenbelt, Maryland, available at https://ntrs.nasa.gov/search.jsp?R=19990060930 (accessed August 2018), 1999.

Chou, M.-D., Suárez, M., Liang, X.-Z., and Yan, M. M.-H.: A thermal infrared radiation parameterization for atmospheric studies, Technical Report Series on Global Modeling and Data Assimilation, No. 19, NASA/TM-2001-104606, Greenbelt, Maryland, available at https://ntrs.nasa.gov/search.jsp?R=20010072848 (accessed August 2018), 2001.

Clough, S., Shephard, M., Mlawer, E., Delamere, J., Iacono, M., Cady-Pereira, K., Boukabara, S., and Brown, P.: Atmospheric radiative transfer modeling: a summary of the AER codes, J. Quant. Spectrosc. Radiat. Transfer, 91, 233–244, https://doi.org/10.1016/j.jqsrt.2004.05.058, 2005.

Corti, T., Luo, B. P., Peter, T., Vömel, H., and Fu, Q.: Mean radiative energy balance and vertical mass fluxes in the equatorial upper troposphere and lower stratosphere, Geophys. Res. Lett., 32, L06802, https://doi.org/10.1029/2004GL021889, 2005.

Courtier, P., Thépaut, J.-N., and Hollingsworth, A.: A strategy for operational implementation of 4D-Var, using an incremental approach, Q. J. Roy. Meteor. Soc., 120, 1367–1387, https://doi.org/10.1002/qj.49712051912, 1994.

Dai, A., Karl, T. R., Sun, B., and Trenberth, K. E.: Recent trends in cloudiness over the United States: A tale of monitoring inadequacies, Bull. Am. Meteor. Soc., 87, 597–606, https://doi.org/10.1175/BAMS-87-5-597, 2006.

Davis, S. M., Hegglin, M. I., Fujiwara, M., Dragani, R., Harada, Y., Kobayashi, C., Long, C., Manney, G. L., Nash, E. R., Potter, G. L., Tegtmeier, S., Wang, T., Wargan, K., and Wright, J. S.: Assessment of upper tropospheric and stratospheric water vapor and ozone in reanalyses as part of S-RIP, Atmos. Chem. Phys., 17, 12 743–12 778, https://doi.org/10.5194/acp-17-12743-2017, 2017.

Dee, D. P., Uppala, S. M., Simmons, A. J., Berrisford, P., Poli, P., Kobayashi, S., Andrae, U., Balmaseda, M. A., Balsamo, G., and Bauer, P.: The ERA-Interim reanalysis: configuration and performance of the data assimilation system, Q. J. Roy. Meteor. Soc., 137, 553–597, https://doi.org/10.1002/qj.828, 2011.

Del Genio, A. D., Yao, M.-S., Kovari, W., and Lo, K. K.-W.: A prognostic cloud water parameterization for global climate models, J. Climate, 9, 270–304, 1996.

Deng, M., Mace, G. G., Wang, Z., and Berry, E.: CloudSat 2C-ICE product update with a new Z_e parameterization in lidar-only region, J. Geophys. Res. Atmos., 120, 12 198–12 208, https://doi.org/10.1002/2015JD023600, 2015.

Dessler, A. E.: A determination of the cloud feedback from climate variations over the past decade, Science, 330, 1523–1527, https://doi.org/10.1126/science.1192546, 2010.

Dessler, A. E. and Yang, P.: The distribution of tropical thin cirrus clouds inferred from Terra MODIS data, J. Climate, 16, 1241–1247, 2003.

Dessler, A. E., Schoeberl, M. R., Wang, T., Davis, S. M., Rosenlof, K. H., and Vernier, J.-P.: Variations of stratospheric water vapor over the past three decades, J. Geophys. Res. Atmos., 119, 12,588–12,598, https://doi.org/10.1002/2014JD021712, 2014.

Doelling, D.: CERES SYN1DEG-DAYTerra+Aqua - Edition 4A, https://doi.org/10.5067/terra+aqua/ceres/syn1degday_l3.004a, accessed: 2018-06-17, 2017.

Doelling, D.: CERES Energy Balanced and Filled (EBAF) TOA and Surface Monthly means data in netCDF Edition 4.1, https://doi.org/10.5067/TERRA-AQUA/CERES/EBAF_L3B.004.1, https://asdc.larc.nasa.gov/project/CERES/CERES_EBAF_Edition4.1, accessed: 2020-05-02, 2019.

Doelling, D. R., Scarino, B. R., Morstad, D., Gopalan, A., Bhatt, R., Lukashin, C., and Minnis, P.: The intercalibration of geostationary visible imagers using operational hyperspectral SCIAMACHY radiances, IEEE Trans. Geosci. Remote Sens., 51, 1245–1254, https://doi.org/10.1109/TGRS.2012.2227760, 2013.

Dolinar, E. K., Dong, X., and Xi, B.: Evaluation and intercomparison of clouds, precipitation, and radiation budgets in recent reanalyses using satellite-surface observations, Clim. Dyn., 46, 2123–2144, https://doi.org/10.1007/s00382-015-2693-z, 2016.

Ebert, E. E. and Curry, J. A.: A parameterization of ice cloud optical properties for climate models, J. Geophys. Res. Atmos., 97, 3831–3836, https://doi.org/10.1029/91JD02472, 1992.

Emanuel, K.: Atmospheric Convection, Oxford University Press, New York, 580 pp., 1994.

Emanuel, K. A., Neelin, D. J., and Bretherton, C. S.: On large-scale circulations in convecting atmospheres, Q. J. Roy. Meteor. Soc., 120, 1111–1143, https://doi.org/10.1002/qj.49712051902, 1994.

Fiehn, A., Quack, B., Hepach, H., Fuhlbrügge, S., Tegtmeier, S., Toohey, M., Atlas, E., and Krüger, K.: Delivery of halogenated very short-lived substances from the west Indian Ocean to the stratosphere during the Asian summer monsoon, Atmos. Chem. Phys., 17, 6723–6741, https://doi.org/10.5194/acp-17-6723-2017, 2017.

Folkins, I., Loewenstein, M., Podolske, J., Oltmans, S. J., and Proffitt, M.: A barrier to vertical mixing at 14 km in the tropics: Evidence from ozonesondes and aircraft measurements, J. Geophys. Res. Atmos., 104, 22 095–22 102, https://doi.org/10.1029/1999JD900404, 1999.

Folkins, I., Braun, C., Thompson, A. M., and Witte, J.: Tropical ozone as an indicator of deep convection, J. Geophys. Res. Atmos., 107, https://doi.org/10.1029/2001JD001178, 2002.

Forbes, R. M., Tompkins, A. M., and Untch, A.: A new prognostic bulk microphysics scheme for the IFS, Technical Memorandum 649, ECMWF, Shinfield Park, Reading, UK, https://doi.org/10.21957/bf6vjvxk, available at https://www.ecmwf.int/node/9441 (accessed August 2019), 2011.

Fouquart, Y.: Radiative transfer in climate models, in: Physically-Based Modelling and Simulation of Climate and Climatic Change: Part 1, edited by Schlesinger, M. E., pp. 223–283, Springer Netherlands, Dordrecht, https://doi.org/10.1007/978-94-009-3041-4_5, 1988.

Fouquart, Y. and Bonnel, B.: Computation of solar heating of the Earth's atmosphere: a new parameterization, Beitr. Phys., 53, 35–62, 1980.

Fowler, L. D., Wielicki, B. A., Randall, D. A., Branson, M. D., Gibson, G. G., and Denn, F. M.: Use of a GCM to explore sampling issues in connection with satellite remote sensing of the Earth radiation budget, J. Geophys. Res. Atmos., 105, 20 757–20 772, https://doi.org/10.1029/2000JD900239, 2000.

Freidenreich, S. M. and Ramaswamy, V.: A new multiple-band solar radiative parameterization for general circulation models, J. Geophys. Res. Atmos., 104, 31 389–31 409, https://doi.org/10.1029/1999JD900456, 1999.

Fu, Q.: An accurate parameterization of the solar radiative properties of cirrus clouds for climate models, J. Climate, 9, 2058–2082, 1996.

Fu, Q., Yang, P., and Sun, W. B.: An accurate parameterization of the infrared radiative properties of cirrus clouds for climate models, J. Climate, 11, 2223–2237, 1998.

Fu, R., Liu, W. T., and Dickinson, R. E.: Response of tropical clouds to the interannual variation of sea surface temperature, J. Climate, 9, 616–634, 1996.

Fueglistaler, S. and Fu, Q.: Impact of clouds on radiative heating rates in the tropical lower stratosphere, J. Geophys. Res. Atmos., 111, D23202, https://doi.org/10.1029/2006JD007273, 2006.

Fueglistaler, S., Dessler, A. E., Dunkerton, T. J., Folkins, I., Fu, Q., and Motte, P. W.: Tropical tropopause layer, Rev. Geophys., 47, RG1004, https://doi.org/10.1029/2008RG000267, 2009.

Fujiwara, M., Wright, J. S., Manney, G. L., Gray, L. J., Anstey, J., Birner, T., Davis, S., Gerber, E. P., Harvey, V. L., Hegglin, M. I., Homeyer, C. R., Knox, J. A., Krüger, K., Lambert, A., Long, C. S., Martineau, P., Molod, A., Monge-Sanz, B. M., Santee, M. L., Tegtmeier, S., Chabrillat, S., Tan, D. G. H., Jackson, D. R., Polavarapu, S., Compo, G. P., Dragani, R., Ebisuzaki, W., Harada, Y., Kobayashi, C., McCarty, W., Onogi, K., Pawson, S., Simmons, A., Wargan, K., Whitaker, J. S., and Zou, C.-Z.: Introduction to the SPARC Reanalysis Intercomparison Project (S-RIP) and overview of the reanalysis systems, Atmos. Chem. Phys., 17, 1417–1452, https://doi.org/10.5194/acp-17-1417-2017, 2017.

Fusina, F., Spichtinger, P., and Lohmann, U.: Impact of ice supersaturated regions and thin cirrus on radiation in the midlatitudes, J. Geophys. Res. Atmos., 112, D24S14, https://doi.org/10.1029/2007JD008449, 2007.

Gelaro, R., McCarty, W., Suárez, M. J., Todling, R., Molod, A., Takacs, L., Randles, C., Darmenov, A., Bosilovich, M. G., Reichle, R., Wargan, K., Coy, L., Cullather, R., Draper, C., Akella, S., Buchard, V., Conaty, A., da Silva, A., Gu, W., Kim, G.-K., Koster, R., Lucchesi, R., Merkova, D., Nielsen, J. E., Partyka, G., Pawson, S., Putman, W., Rienecker, M., Schubert, S. D., Sienkiewicz, M., and Zhao, B.: The Modern-Era Retrospective Analysis for Research and Applications, Version 2 (MERRA-2), J. Climate, 30, 5419–5454, https://doi.org/10.1175/JCLI-D-16-0758.1, 2017.

Geller, M. A., Zhou, T., and Yuan, W.: The QBO, gravity waves forced by tropical convection, and ENSO, J. Geophys. Res. Atmos., 121, 8886–8895, https://doi.org/10.1002/2015JD024125, 2016.

Gettelman, A., Forster, P. M. d. F., Fujiwara, M., Fu, Q., Vömel, H., Gohar, L. K., Johanson, C., and Ammerman, M.: Radiation balance of the tropical tropopause layer, J. Geophys. Res. Atmos., 109, D07103, https://doi.org/10.1029/2003JD004190, 2004.

Gregory, D., Morcrette, J.-J., Jacob, C., Beljaars, A. C. M., and Stockdale, T.: Revision of convection, radiation and cloud schemes in the ECMWF integrated forecast system, Q. J. Roy. Meteor. Soc., 126, 1685–1710, 2000.

Hartmann, D. L. and Larson, K.: An important constraint on tropical cloud - climate feedback, Geophys. Res. Lett., 29, 1951, https://doi.org/10.1029/2002GL015835, 2002.

Hartmann, D. L. and Michelsen, M. L.: Large-scale effects on the regulation of tropical sea surface temperature, J. Climate, 6, 2049–2062, 1993.

Hearty, T. J., Savtchenko, A., Tian, B., Fetzer, E., Yung, Y. L., Theobald, M., Vollmer, B., Fishbein, E., and Won, Y.: Estimating sampling biases and measurement uncertainties of AIRS/AMSU-A temperature and water vapor observations using MERRA reanalysis, J. Geophys. Res. Atmos., 119, 2725–2741, https://doi.org/10.1002/2013JD021205, 2014.

Hersbach, H., de Rosnay, P., Bell, B., Schepers, D., Simmons, A., Soci, C., Abdalla, S., Alonso-Balmaseda, M., Balsamo, G., Bechtold, P., Berrisford, P., Bidlot, J.-R., de Boisséson, E., Bonavita, M., Browne, P., Buizza, R., Dahlgren, P., Dee, D., Dragani, R., Diamantakis, M., Flemming, J., Forbes, R., Geer, A. J., Haiden, T., Hólm, E., Haimberger, L., Hogan, R., Horányi, A., Janiskova, M., Laloyaux, P., Lopez, P., Munoz-Sabater, J., Peubey, C., Radu, R., Richardson, D., Thépaut, J.-N., Vitart, F., Yang, X., Zsótér, E., and Zuo, H.: Operational global reanalysis: progress, future directions and synergies with NWP, ERA Report Series, 27, https://doi.org/10.21957/tkic6g3wm, 2018.

Hersbach, H., Bell, B., Berrisford, P., Hirahara, S., Horányi, A., Muñoz-Sabater, J., Nicolas, J., Peubey, C., Radu, R., Schepers, D., Simmons, A., Soci, C., Abdalla, S., Abellan, X., Balsamo, G., Bechtold, P., Biavati, G., Bidlot, J., Bonavita, M., De Chiara, G., Dahlgren, P., Dee, D., Diamantakis, M., Dragani, R., Flemming, J., Forbes, R., Fuentes, M., Geer, A., Haimberger, L., Healy, S., Hogan, R. J., Hólm, E., Janisková, M., Keeley, S., Laloyaux, P., Lopez, P., Lupu, C., Radnoti, G., de Rosnay, P., Rozum, I., Vamborg, F., Villaume, S., and Thépaut, J.-N.: The ERA5 Global Reanalysis, Q. J. Roy. Meteor. Soc., accepted manuscript, https://doi.org/10.1002/qj.3803, 2020.

Hoffmann, L., Günther, G., Li, D., Stein, O., Wu, X., Griessbach, S., Heng, Y., Konopka, P., Müller, R., Vogel, B., and Wright, J. S.: From ERA-Interim to ERA5: the considerable impact of ECMWF's next-generation reanalysis on Lagrangian transport simulations, Atmos. Chem. Phys., 19, 3097–3124, https://doi.org/10.5194/acp-19-3097-2019, 2019.

Hong, S.-Y. and Pan, H.-L.: Convective trigger function for a mass-flux cumulus parameterization scheme, Mon. Wea. Rev., 126, 2599–2620, 1998.

Hu, Y. X. and Stamnes, K.: An accurate parameterization of the radiative properties of water clouds suitable for use in climate models, J. Climate, 6, 728–742, 1993.

Huang, Y. and Ramaswamy, V.: Evolution and trend of the outgoing longwave radiation spectrum, J. Climate, 22, 4637–4651, https://doi.org/10.1175/2009JCLI2874.1, 2009.

Iacono, M. J., Delamere, J. S., Mlawer, E. J., Shephard, M. W., Clough, S. A., and Collins, W. D.: Radiative forcing by long-lived greenhouse gases: Calculations with the AER radiative transfer models, J. Geophys. Res. Atmos., 113, D13103, https://doi.org/10.1029/2008JD009944, 2008.

Jiang, J. H., Livesey, N. J., Su, H., Neary, L., McConnell, J. C., and Richards, N. A. D.: Connecting surface emissions, convective uplifting, and long-range transport of carbon monoxide in the upper troposphere: New observations from the Aura Microwave Limb Sounder, Geophys. Res. Lett., 34, L18812, https://doi.org/10.1029/2007GL030638, 2007.

JMA: Outline of the operational numerical weather prediction at the Japan Meteorological Agency, Tech. rep., Japan Meteorological Agency, Tokyo, http://www.jma.go.jp/jma/jma-eng/jma-center/nwp/outline2013-nwp/index.htm, 2013.

Johnson, R. H., Rickenbach, T. M., Rutledge, S. A., Ciesielski, P. E., and Schubert, W. H.: Trimodal characteristics of tropical convection, J. Climate, 12, 2397–2418, 1999.

Kawai, H. and Inoue, T.: A simple parameterization scheme for subtropical marine stratocumulus, SOLA, 2, 17–20, https://doi.org/10.2151/sola.2006-005, 2006.

Kay, J. E. and Gettelman, A.: Cloud influence on and response to seasonal Arctic sea ice loss, J. Geophys. Res. Atmos., 114, D18204, https://doi.org/10.1029/2009JD011773, 2009.

Kim, J., Randel, W. J., and Birner, T.: Convectively driven tropopause-level cooling and its influences on stratospheric moisture, J. Geophys. Res. Atmos., 123, 590–606, https://doi.org/10.1002/2017JD027080, 2017.

Kobayashi, S., Ota, Y., Harada, Y., Ebita, A., Moriya, M., Onoda, H., Onogi, K., Kamahori, H., Kobayashi, C., Endo, H., Miyaoka, K., and Takahashi, K.: The JRA-55 Reanalysis: General Specifications and Basic Characteristics, J. Meteorol. Soc. Jpn., 93, 5–48, https://doi.org/10.2151/jmsj.2015-001, 2015.

Kolly, A. and Huang, Y.: The radiative feedback during the ENSO cycle: observations versus models, J. Geophys. Res. Atmos., 123, 9097–9108, https://doi.org/10.1029/2018JD028401, 2018.

Kosaka, Y. and Xie, S.: Recent global-warming hiatus tied to equatorial Pacific surface cooling, Nature, 501, 403–407, https://doi.org/10.1038/nature12534, 2013.

Lane, T. P. and Moncrieff, M. W.: Stratospheric gravity waves generated by multiscale tropical convection, J. Atmos. Sci., 65, 2598–2614, https://doi.org/10.1175/2007JAS2601.1, 2008.

L'Ecuyer, T. S., Wood, N. B., Haladay, T., Stephens, G. L., and Stackhouse Jr., P. W.: Impact of clouds on atmospheric heating based on the R04 CloudSat fluxes and heating rates data set, J. Geophys. Res. Atmos., 113, D00A15, https://doi.org/10.1029/2008JD009951, 2008.

LeMone, M. A., Barnes, G. M., and Zipser, E. J.: Momentum flux by lines of cumulonimbus over the tropical oceans, J. Atmos. Sci., 41, 1914–1932, 1984.

Li, J., Mao, J., and Wang, F.: Comparative study of five current reanalyses in characterizing total cloud fraction and top-of-the-atmosphere cloud radiative effects over the Asian monsoon region, Int. J. Climatol., 37, 5047–2741, https://doi.org/10.1002/joc.5143, 2017.

Li, J.-L. F., Waliser, D. E., Chen, W.-T., Guan, B., Kubar, T., Stephens, G., Ma, H.-Y., Deng, M., Donner, L., Seman, C., and Horowitz, L.: An observationally based evaluation of cloud ice water in CMIP3 and CMIP5 GCMs and contemporary reanalyses using contemporary satellite data, J. Geophys. Res. Atmos., 117, D16105, https://doi.org/10.1029/2012JD017640, 2012.

Li, J.-L. F., Waliser, D. E., Stephens, G., and Lee, S.: Characterizing and understanding cloud ice and radiation budget biases in global climate models and reanalysis, Meteor. Monogr., 56, 13.1–13.20, https://doi.org/10.1175/AMSMONOGRAPHS-D-15-0007.1, 2016.

Lim, Y.-K., Schubert, S. D., Reale, O., Lee, M.-I., Molod, A. M., and Suárez, M. J.: Sensitivity of tropical cyclones to parameterized convection in the NASA GEOS-5 model, J. Climate, 28, 551–573, https://doi.org/10.1175/JCLI-D-14-00104.1, 2015.

Lindner, T. H. and Li, J.: Parameterization of the optical properties for water clouds in the infrared, J. Climate, 13, 1797–1805, 2000.

Loeb, N. G., Rose, F. G., Kato, S., Rutan, D. A., Su, W., Wang, H., Doelling, D. R., Smith, W. L., and Gettelman, A.: Toward a consistent definition between satellite and model clear-sky radiative fluxes, J. Climate, 33, 61–75, https://doi.org/10.1175/JCLI-D-19-0381.1, 2020.

Long, C. S., Fujiwara, M., Davis, S., Mitchell, D. M., and Wright, C. J.: Climatology and interannual variability of dynamic variables in multiple reanalyses evaluated by the SPARC Reanalysis Intercomparison Project (S-RIP), Atmos. Chem. Phys., 17, 14 593–14 629, https://doi.org/10.5194/acp-17-14593-2017, 2017.

Machado, L. A. T., Rossow, W. B., Guedes, R. L., and Walker, A. W.: Life cycle variations of mesoscale convective systems over the Americas, Mon. Wea. Rev., 126, 1630–1654, 1998.

Massie, S., Gettelman, A., Randel, W., and Baumgardner, D.: Distribution of tropical cirrus in relation to convection, J. Geophys. Res. Atmos., 107, 4591, https://doi.org/10.1029/2001JD001293, 2002.

May, R., Arms, S., Marsh, P., Bruning, E., and Leeman, J.: MetPy: A Python package for meteorological data, https://doi.org/10.5065/D6WW7G29, version 0.8.0, Unidata, Boulder, Colorado, 2008 - 2020.

Minnis, P., Sun-Mack, S., Young, D. F., Heck, P. W., Garber, D. P., Chen, Y., Spangenberg, D. A., Arduini, R. F., Trepte, Q. Z., Smith, W. L., Ayers, J. K., Gibson, S. C., Miller, W. F., Hong, G., Chakrapani, V., Takano, Y., Liou, K.-N., Xie, Y., and Yang, P.: CERES Edition-2 cloud property retrievals using TRMM VIRS and Terra and Aqua MODIS data. Part I: Algorithms, IEEE Trans. Geosci. Remote Sens., 49, 4374–4400, https://doi.org/10.1109/TGRS.2011.2144601, 2011.

Mlawer, E. J., Taubman, S. J., Brown, P. D., Iacono, M. J., and Clough, S. A.: Radiative transfer for inhomogeneous atmospheres: RRTM, a validated correlated-k model for the longwave, J. Geophys. Res. Atmos., 102, 16 663–16 682, https://doi.org/10.1029/97JD00237, 1997.

Molod, A.: Constraints on the profiles of total water PDF in AGCMs from AIRS and a high-resolution model, J. Climate, 25, 8341–8352, https://doi.org/10.1175/JCLI-D-11-00412.1, 2012.

Molod, A., Takacs, L., Suárez, M., Bacmeister, J., sun Song, I., and Eichmann, A.: The GEOS-5 atmospheric general circulation model: Mean climate and development from MERRA to Fortuna, Technical Report Series on Global Modeling and Data Assimilation, No. 28, NASA/2012-104606, Greenbelt, Maryland, 124 pp., available at https://ntrs.nasa.gov/search.jsp?R=20120011790 (accessed September 2019), 2012.

Molod, A., Takacs, L., Suárez, M., and Bacmeister, J.: Development of the GEOS-5 atmospheric general circulation model: evolution from MERRA to MERRA2, Geosci. Model Dev., 8, 1339–1356, https://doi.org/10.5194/gmd-8-1339-2015, 2015.

Moorthi, S. and Suárez, M. J.: Relaxed Arakawa-Schubert. A parameterization of moist convection for general circulation models, Mon. Wea. Rev., 120, 978–1002, 1992.

Moorthi, S., Pan, H.-L., and Caplan, P.: Changes to the 2001 NCEP operational MRF/AVN global analysis/forecast system, Tech. rep., Technical Procedures Bulletin No. 484, NOAA National Weather Service, Silver Spring, MD, 2001.

Morcrette, J.-J., Barker, H. W., Cole, J. N. S., Iacono, M. J., and Pincus, R.: Impact of a new radiation package, McRad, in the ECMWF Integrated Forecasting System, Mon. Wea. Rev., 136, 4773–4798, https://doi.org/10.1175/2008MWR2363.1, 2008.

Murai, S., Yabu, S., and Kitagawa, H.: Development of a new radiation scheme for the global atmospheric NWP model, American Meteorological Society 21st Conference on Weather Analysis and Forecasting and 17th Conference on Numerical Weather Prediction, 1–5 August 2005, Washington D.C., 5 pp., available at https://ams.confex.com/ams/pdfpapers/94316.pdf (accessed November 2019), 2005.

Norton, W. A.: Longwave heating of the tropical lower stratosphere, Geophys. Res. Lett., 28, 3653–3656, https://doi.org/10.1029/2001GL013379, 2001.

O'Gorman, P. A., Allan, R. P., Byrne, M. P., and Previdi, M.: Energetic constraints on precipitation under climate change, Surv. Geophys., 33, 585–608, https://doi.org/10.1007/s10712-011-9159-6, 2011.

Pan, H.-L. and Wu, W.: Implementing a mass flux convective parameterization package for the NMC Medium-Range Forecast model, NMC Office Note 409, 43 pp., available at http://www.emc.ncep.noaa.gov/officenotes/FullTOC.html (accessed August 2018), 1995.

Pan, L. L., Atlas, E. L., Salawitch, R. J., Honomichl, S. B., Bresch, J. F., Randel, W. J., Apel, E. C., Hornbrook, R. S., Weinheimer, A. J., Anderson, D. C., Andrews, S. J., Baidar, S., Beaton, S. P., Campos, T. L., Carpenter, L. J., Chen, D., Dix, B., Donets, V., Hall, S. R., Hanisco, T. F., Homeyer, C. R., Huey, L. G., Jensen, J. B., Kaser, L., Kinnison, D. E., Koenig, T. K., Lamarque, J.-F., Liu, C., Luo, J., Luo, Z. J., Montzka, D. D., Nicely, J. M., Pierce, R. B., Riemer, D. D., Robinson, T., Romashkin, P., Saiz-Lopez, A., Schauffler, S., Shieh, O., Stell, M. H., Ullmann, K., Vaughan, G., Volkamer, R., and Wolfe, G.: The Convective Transport of Active Species in the Tropics (CONTRAST) experiment, Bull. Am. Meteor. Soc., 98, 106–128, https://doi.org/10.1175/BAMS-D-14-00272.1, 2017.

Pedregosa, F., Varoquaux, G., Gramfort, A., Michel, V., Thirion, B., Grisel, O., Blondel, M., Prettenhofer, P., Weiss, R., Dubourg, V., Vanderplas, J., Passos, A., Cournapeau, D., Brucher, M., Perrot, M., and Duchesnay, E.: Scikit-learn: Machine Learning in Python, J. Mach. Learn. Res., 12, 2825–2830, 2011.

Pincus, R., Barker, H. W., and Morcrette, J.-J.: A fast, flexible, approximate technique for computing radiative transfer in inhomogeneous cloud fields, J. Geophys. Res. Atmos., 108, 4376, https://doi.org/10.1029/2002JD003322, 2003.

Pincus, R., Platnick, S., Ackerman, S. A., Hemler, R. S., and Patrick Hofmann, R. J.: Reconciling simulated and observed views of clouds: MODIS, ISCCP, and the limits of instrument simulators, J. Climate, 25, 4699–4720, https://doi.org/10.1175/JCLI-D-11-00267.1, 2012.

Platnick, S.: MODIS Atmosphere L3 Daily Product, https://doi.org/10.5067/modis/mod08_d3.061, 2015.

Posselt, D. J., Jongeward, A. R., Hsu, C. Y., and Potter, G. L.: Object-based evaluation of MERRA cloud physical properties and radiative fluxes during the 1998 El Niño-La Niña transition, J. Climate, 25, 7313–7327, https://doi.org/10.1175/JCLI-D-11-00724.1, 2011.

Reynolds, R. W., Smith, T. M., Liu, C., Chelton, D. B., Casey, K. S., and Schlax, M. G.: Daily high-resolution-blended analyses for sea surface temperature, J. Climate, 20, 5473–5496, https://doi.org/10.1175/2007JCLI1824.1, 2007.

Rienecker, M. M., Suárez, M. J., Todling, R., Bacmeister, J., Takacs, L., Liu, H.-C., Gu, W., Sienkiewicz, M., Koster, R. D., Gelaro, R., Stajner, I., and Nielsen, J. E.: The GEOS-5 Data Assimilation System—Documentation of versions 5.0.1 and 5.1.0, and 5.2.0, Technical Report Series on Global Modeling and Data Assimilation, No. 27, NASA/TM-2008-104606, Greenbelt, Maryland, 92 pp., available at https://ntrs.nasa.gov/search.jsp?R=20120011955 (accessed September 2019), 2008.

Rienecker, M. M., Suárez, M. J., Gelaro, R., Todling, R., Bacmeister, J., Liu, E., Bosilovich, M. G., Schubert, S. D., Takacs, L., Kim, G.-K., Bloom, S., Chen, J., Collins, D., Conaty, A., da Silva, A., Gu, W., Joiner, J., Koster, R. D., Lucchesi, R., Molod, A., Owens, T., Pawson, S., Pegion, P., Redder, C. R., Reichle, R., Robertson, F. R., Ruddick, A. G., Sienkiewicz, M., and Woollen, J.: MERRA: NASA's Modern-Era Retrospective Analysis for Research and Applications, J. Climate, 24, 3624–3648, https://doi.org/10.1175/JCLI-D-11-00015.1, 2011.

Rossow, W., Golea, V., Walker, A., Knapp, K., Young, A., Hankins, B., and Inamdar, A.: International Satellite Cloud Climatology Project (ISCCP) Climate Data Record, H-Series, https://doi.org/10.7289/V5QZ281S, 2017.

Rossow, W. B. and Schiffer, R. A.: ISCCP cloud data products, Bull. Am. Meteor. Soc., 72, 2–20, 1991.

Rossow, W. B. and Schiffer, R. A.: Advances in understanding clouds from ISCCP, Bull. Am. Meteor. Soc., 80, 1999.

Saha, S., Moorthi, S., Pan, H.-L., Wu, X., Wang, J., Nadiga, S., Tripp, P., Kistler, R., Woollen, J., Behringer, D., Liu, H., Stokes, D., Grumbine, R., Gayno, G., Wang, J., Hou, Y.-T., Chuang, H.-Y., Juang, H.-M. H., Sela, J., Iredell, M., Treadon, R., Kleist, D., Van Delst, P., Keyser, D., Derber, J., Ek, M., Meng, J., Wei, H., Yang, R., Lord, S., Van Den Dool, H., Kumar, A., Wang, W., Long, C., Chelliah, M., Xue, Y., Huang, B., Schemm, J.-K., Ebisuzaki, W., Lin, R., Xie, P., Chen, M., Zhou, S., Higgins, W., Zou, C.-Z., Liu, Q., Chen, Y., Han, Y., Cucurull, L., Reynolds, R. W., Rutledge, G., and Goldberg, M.: The NCEP Climate Forecast System Reanalysis, Bull. Am. Meteor. Soc., 91, 1015–1057, https://doi.org/10.1175/2010BAMS3001.1, 2010.

Saha, S., Moorthi, S., Wu, X., Wang, J., Nadiga, S., Tripp, P., Behringer, D., Hou, Y. T., Chuang, H., and Iredell, M.: The NCEP Climate Forecast System Version 2, J. Climate, 27, 2185–2208, https://doi.org/10.1175/JCLI-D-12-00823.1, 2014.

Schoeberl, M. R., Dessler, A. E., and Wang, T.: Simulation of stratospheric water vapor and trends using three reanalyses, Atmos. Chem. Phys., 12, 6475–6487, https://doi.org/10.5194/acp-12-6475-2012, 2012.

Schoeberl, M. R., Jensen, E. J., Pfister, L., Ueyama, R., Wang, T., Selkirk, H., Avery, M., Thornberry, T., and Dessler, A. E.: Water vapor, clouds, and saturation in the tropical tropopause layer, J. Geophys. Res. Atmos., 124, 3984–4003, https://doi.org/10.1029/2018JD029849, 2019.

Sen, P. K.: Estimates of the regression coefficient based on Kendall's Tau, J. Am. Stat. Assoc., 63, 1379–1389, https://doi.org/10.1080/01621459.1968.10480934, 1968.

Sherwood, S. C., Chae, J.-H., Minnis, P., and McGill, M.: Underestimation of deep convective cloud tops by thermal imagery, Geophys. Res. Lett., 31, L11102, https://doi.org/10.1029/2004GL019699, 2004.

Slingo, A.: A GCM parameterization for the shortwave radiative properties of water clouds, J. Atmos. Sci., 46, 1419–1427, 1989.

Smith, E. A. and Shi, L.: Surface forcing of the infrared cooling profile over the Tibetan Plateau. Part I: Influence of relative longwave radiative heating at high altitude, J. Atmos. Sci., 49, 805–822, 1992.

Smith, R. N. B.: A scheme for predicting layer clouds and their water content in a general circulation model, Q. J. Roy. Meteor. Soc., 116, 435–460, https://doi.org/10.1002/qj.49711649210, 1990.

Soden, B. J., Broccoli, A. J., and Hemler, R. S.: On the use of cloud forcing to estimate cloud feedback, J. Climate, 17, 3661–3665, 2004.

Sommeria, G. and Deardorff, J. W.: Subgrid-scale condensation in models of nonprecipitating clouds, J. Atmos. Sci., 34, 344–355, 1977.

Song, J., Wang, Y., and Tang, J.: A hiatus of the greenhouse effect, Sci. Rep., 6, 33315, https://doi.org/10.1038/srep33315, 2016.

Stackhouse, Jr., P. W., Gupta, S. K., Cox, S. J., Mikovitz, J. C., Zhang, T., and Hinkelman, L. M.: The NASA/GEWEX Surface Radiation Budget Release 3.0: 24.5-Year Dataset,, GEWEX News, 21, No.1, February, available at https://www.gewex.org/resources/gewex-news (accessed August 2019), 2011.

Stengel, M., Schlundt, C., Stapelberg, S., Sus, O., Eliasson, S., Willén, U., and Meirink, J. F.: Comparing ERA-Interim clouds with satellite observations using a simplified satellite simulator, Atmos. Chem. Phys. Disc., https://doi.org/10.5194/acp-2018-258, 2018.

Stephens, G. L. and Kummerow, C. D.: The remote sensing of clouds and precipitation from space: A review, J. Atmos. Sci., 64, 3742–3765, https://doi.org/10.1175/2006JAS2375.1, 2007.

Stephens, G. L. and L'Ecuyer, T.: The Earth's energy balance, Atmos. Res., 166, 195–203, https://doi.org/10.1016/j.atmosres.2015.06.024, 2015.

Stevens, B. and Schwartz, S. E.: Observing and modeling Earth's energy flows, Surv. Geophys., 33, 779–816, https://doi.org/10.1007/s10712-012-9184-0, 2012.

Stubenrauch, C. J., Rossow, W. B., Kinne, S., Ackerman, S., Cesana, G., Chepfer, H., Di Girolamo, L., Getzewich, B., Guignard, A., Heidinger, A., Maddux, B. C., Menzel, W. P., Minnis, P., Pearl, C., Platnick, S., Poulsen, C., Riedi, J., Sun-Mack, S., Walther, A., Winker, D., Zeng, S., and Zhao, G.: Assessment of global cloud datasets from satellites: Project and database initiated by the GEWEX Radiation Panel, Bull. Am. Meteor. Soc., 94, 1031–1049, https://doi.org/10.1175/BAMS-D-12-00117.1, 2013.

Su, H., Jiang, J. H., Teixeira, J., Gettelman, A., Huang, X., Stephens, G., Vane, D., and Perun, V. S.: Comparison of regime-sorted tropical cloud profiles observed by CloudSat with GEOS5 analyses and two general circulation models, J. Geophys. Res. Atmos., 116, 644–644, https://doi.org/10.1029/2010JD014971, 2011.

Takacs, L., Suárez, M., and Todling, R.: The stability of incremental analysis update, Mon. Wea. Rev., 146, 3259–3275, https://doi.org/10.1175/MWR-D-18-0117.1, 2018.

Tao, M., Konopka, P., Ploeger, F., Yan, X., Wright, J. S., Diallo, M., Fueglistaler, S., and Riese, M.: Multi-timescale variations of modelled stratospheric water vapor derived from three modern reanalysis products, Atmos. Chem. Phys., 19, 6509–6534, https://doi.org/10.5194/acp-19-6509-2019, 2019.

Tegtmeier, S., Anstey, J., Davis, S., Dragani, R., Harada, Y., Ivanciu, I., Pilch Kedzierski, R., Krüger, K., Legras, B., Long, C., Wang, J. S., Wargan, K., and Wright, J. S.: Temperature and tropopause characteristics from reanalyses data in the tropical tropopause layer, Atmos. Chem. Phys., 20, 753–770, https://doi.org/10.5194/acp-20-753-2020, 2020.

Texeira, A. S. T.: Aqua AIRS Level 3 Standard Daily Product using AIRS and AMSU without HSB V6, https://doi.org/10.5067/aqua/airs/data301, accessed: 2017-03-13, 2013.

Tian, B., Manning, E., Fetzer, E., Olsen, E., Wong, S., Susskind, J., and Iredell, L.: AIRS/AMSU/HSB Version 6 Level 3 Product User Guide, Tech. rep., Jet Propulsion Laboratory, Pasadena, California, 2013.

Tiedtke, M.: A comprehensive mass flux scheme for cumulus parameterization in large-scale models, Mon. Wea. Rev., 117, 1779–1800, 1989.

Tiedtke, M.: Representation of clouds in large-scale models, Mon. Wea. Rev., 121, 3040–3061, 1993.

Trenberth, K. E., Fasullo, J. T., and Kiehl, J.: Earth's global energy budget, Bull. Am. Meteor. Soc., 90, 311–324, https://doi.org/10.1175/2008BAMS2634.1, 2009.

Tsay, S.-C., Stamnes, K., and Jayaweera, K.: Radiative energy budget in the cloudy and hazy Arctic, J. Atmos. Sci., 46, 1002–1018, 1989.

Wall, C. J., Hartmann, D. L., and Norris, J. R.: Is the net cloud radiative effect constrained to be uniform over the tropical warm pools?, Geophys. Res. Lett., 46, 12 495–12 503, https://doi.org/10.1029/2019GL083642, 2019.

Wang, T., Wong, S., and Fetzer, E. J.: Cloud regime evolution in the Indian monsoon intraseasonal oscillation: Connection to large-scale dynamical conditions and the atmospheric water budget, Geophys. Res. Lett., 42, 9465–9472, https://doi.org/10.1002/2015GL066353, 2015.

Wielicki, B. A., Barkstrom, B. R., Harrison, E. F., Lee, III, R. B., Smith, G. L., and Cooper, J. E.: Clouds and the Earth's Radiant Energy System (CERES): An Earth Observing System experiment, Bull. Am. Meteor. Soc., 77, 853–868, 1996.

Wright, J. S. and Fueglistaler, S.: Large differences in reanalyses of diabatic heating in the tropical upper troposphere and lower stratosphere, Atmos. Chem. Phys., 13, 9565–9576, https://doi.org/10.5194/acp-13-9565-2013, 2013.

Wright, J. S., Fujiwara, M., Long, C., Anstey, J., Chabrillat, S., Compo, G. P., Dragani, R., Ebisuzaki, W., Harada, Y., Kobayashi, C., McCarty, W., Molod, A., Onogi, K., Pawson, S., Simmons, A., Tan, D. G. H., Tegtmeier, S., Wargan, K., Whitaker, J. S., and Zou, C.-Z.: Chapter 2: Description of the Reanalysis Systems, in: Stratosphere-troposphere Processes And their Role in Climate (SPARC) Reanalysis Intercomparison Project (S-RIP) Report, edited by Fujiwara, M., Manney, G. L., Gray, L., and Wright, J. S., under revision for the SPARC Report Series, available at https://jonathonwright.github.io/S-RIPChapter2E.pdf (accessed August 2019), 2020.

Xie, S. and Zhang, M.: Impact of the convection triggering function on single-column model simulations, J. Geophys. Res. Atmos., 105, 14 983–14 996, https://doi.org/10.1029/2000JD900170, 2000.

Xu, K.-M. and Randall, D. A.: A semiempirical cloudiness parameterization for use in climate models, J. Atmos. Sci., 53, 3084–3102, 1996.

Yang, G.-Y. and Slingo, J.: The diurnal cycle in the tropics, Mon. Wea. Rev., 129, 784–801, 2001.

Yang, Q., Fu, Q., and Hu, Y.: Radiative impacts of clouds in the tropical tropopause layer, J. Geophys. Res. Atmos., 115, D00H12, https://doi.org/10.1029/2009JD012393, 2010.

Zhang, K., Randel, W. J., and Fu, R.: Relationships between outgoing longwave radiation and diabatic heating in reanalyses, Clim. Dyn., 49, 2911–2929, https://doi.org/10.1007/s00382-016-3501-0, 2017.

Zhang, M. H., Lin, W. Y., Klein, S. A., Bacmeister, J. T., Bony, S., Cederwall, R. T., Genio, A. D. D., Hack, J. J., Loeb, N. G., and Lohmann, U.: Comparing clouds and their seasonal variations in 10 atmospheric general circulation models with satellite measurements, J. Geophys. Res. Atmos., 110, D15S02, https://doi.org/10.1029/2004JD005021, 2005.

Zhang, T., Stackhouse, P. W., Gupta, S. K., Cox, S. J., and Mikovitz, J. C.: The validation of the GEWEX SRB surface longwave flux data products using BSRN measurements, J. Quant. Spectrosc. Radiat. Transfer, 150, 134–147, https://doi.org/10.1016/j.jqsrt.2014.07.013, 2015.

Zhao, Q. and Carr, F. H.: A prognostic cloud scheme for operational NWP models, Mon. Wea. Rev., 125, 1931–1953, 1997.

Zhao, X., Lin, Y., Peng, Y., Wang, B., Morrison, H., and Gettelman, A.: A single ice approach using varying ice particle properties in global climate model microphysics, J. Adv. Model. Earth Syst., 9, 2138–2157, https://doi.org/10.1002/2017MS000952, 2017.